WIND ENERGY MANAGEMENT

Edited by **Paritosh Bhattacharya**

INTECHWEB.ORG

Wind Energy Management
Edited by Paritosh Bhattacharya

Published by InTech
Janeza Trdine 9, 51000 Rijeka, Croatia

Publishing Process Manager Romina Krebel
Technical Editor Teodora Smiljanic
Cover Designer Jan Hyrat
Image Copyright Sander van der Werf, 2010. Used under license from Shutterstock.com

First published July, 2011
Printed in Croatia

A free online edition of this book is available at www.intechopen.com
Additional hard copies can be obtained from orders@intechweb.org

Wind Energy Management, Edited by Paritosh Bhattacharya
p. cm.
ISBN 978-953-307-336-1

Contents

Preface

Wind energy is one of the most prominent renewable energy sources today. The increasing concerns with environmental issues are driving the search for more sustainable electrical sources. Wind energy along with solar energy, biomass and wave energy are possible solutions for environmentally friendly energy production. The initialization of wind power installation, which started in the beginning of 1980s, is very much related to the oil crises of the mid 1970s. During the 1980s, most wind power installations were limited to a few hundred kilowatts. The small size of those installations did not threaten the power system stability. The 1990s marked an important breakthrough in the industry. New concepts emerged because of the demand for more efficient power production and because of the necessity to comply with power quality requirements. During the 1990s, wind turbines grew in size and production, from just a few hundred kilowatts to megawatts. This book focuses on Weibull Distributioin, Environmental hydraulics, power system control, wind turbine generators etc.

The successful completion of this book has been the result of the co-operation and input by numerous people. I wish to both acknowledge and express my gratitude to all of them.

Since the inception of this work to its final stages, I have been privileged to find guidance, support and strength from Prof. (Dr.) P.K.Bose, Director, National Institute of Technology, Agartala, Tripura and Prof. (Dr.) B.B. Ghosh, Ex-Professor, Indian Institute of Technology, Kharagpur who are highly distinguished personalities in their own field. I feel highly indebted and find a great pleasure in expressing my deep sense of gratitude to both of them.

I am thankful to our publishers InTech for the painstaking efforts and cooperation in bringing out this book in a short span of time.

Finally, I am also thankful to all my well wishers and friends who encouraged me directly or indirectly for this work. My life long thanks to my wife Mrs. Indrani, my son Priyotosh, who bear with me in my good and worst period of my life.

Dr. Paritosh Bhattacharya
Department of Mathematics
College of Engineering & Management
Kolaghat, India

Part 1

Weibull Distribution and Its Analysis

1

Weibull Distribution for Estimating the Parameters

Paritosh Bhattacharya
Department of Mathematics, College of Engineering & Management, Kolaghat
India

1. Introduction

Today, most electrical energy is generated by burning huge fossil fuels and special weather conditions such as acid rain and snow, climate change, urban smog, regional haze, several tornados, etc., have happened around the whole world. It is now clear that the installation of a number of wind turbine generators can effectively reduce environmental pollution, fossil fuel consumption, and the costs of overall electricity generation. Although wind is only an intermittent source of energy, it represents a reliable energy resource from a long-term energy policy viewpoint. Among various renewable energy resources, wind power energy is one of the most popular and promising energy resources in the whole world today. At a specific wind farm, the available electricity generated by a wind power generation system depends on mean wind speed (MWS), standard deviation of wind speed, and the location of installation. Since year-to-year variation on annual MWS is hard to predict, wind speed variations during a year can be well characterized in terms of a probability distribution function (pdf). This paper also addresses the relations among MWS, its standard deviation, and two important parameters of Weibull distribution.
The wind resource varies with of the day and the season of the year and even some extent from year to year. Wind energy has inherent variances and hence it has been expressed by distribution functions. In this paper, we present some methods for estimating Weibull parameters, namely, shape parameter (k) and scale parameter (c). The Weibul distribution is an important distribution especially for reliability and maintainability analysis. The suitable values for both shape parameter and scale parameters of Weibull distribution are important for selecting locations of installing wind turbine generators. The scale parameter of Weibull distribution also important to determine whether a wind farm is good or not. The presented method is the analytical methods and computational experiments on the presented methods are reported.

2. Weibull distribution

The Weibull distribution is characterized by two parameters, one is the shape parameter k (dimensionless) and the other is the scale parameter c (m/s)
The cumulative distribution function is given by

$$F(v) = 1 - \exp\left[-\left(\frac{v}{c}\right)^k\right] \tag{1}$$

And the probability function is given by

$$f(v)=\frac{dF(v)}{dv}=\frac{k}{c}\left(\frac{v}{c}\right)^{k-1}\exp\left[-\left(\frac{v}{c}\right)^{k}\right] \tag{2}$$

The average wind speed can be expressed as

$$\bar{v}=\int_0^\infty vf(v)dv=\int_0^\infty \frac{vk}{c}\left[(\frac{v}{c})^{k-1}\right]\exp\left[-(\frac{v}{c})^{k}\right]dv \tag{3}$$

$$\text{Let}\quad x=(\frac{v}{c})^{k}\quad ,\ x^{\frac{1}{k}}=\frac{v}{c}\quad \text{and}\quad dx=\frac{k}{c}(\frac{v}{c})^{k-1}dv$$

Equation (3) can be simplified as

$$\bar{v}=c\int_0^\infty x^{\frac{1}{k}}\exp(-x)dx \tag{4}$$

By substituting a Gamma Function

$$\Gamma(n)=\int_0^\infty e^{-x}x^{n-1}dx\quad \text{into (4) and let } y=1+\frac{1}{k}\ \text{ then we have}$$

$$\bar{v}=c\Gamma\left(1+\frac{1}{k}\right) \tag{5}$$

The standard deviation of wind speed v is given by

$$\sigma=\sqrt{\int_0^\infty (v-\bar{v})^2 f(v)dv} \tag{6}$$

i.e.

$$\begin{aligned}\sigma&=\sqrt{\int_0^\infty (v^2-2v\bar{v}+\bar{v}^2)f(v)dv}\\&=\sqrt{\int_0^\infty v^2f(v)dv-2\bar{v}\int_0^\infty vf(v)dv+\bar{v}^2}\\&=\sqrt{\int_0^\infty v^2f(v)dv-2\bar{v}.\bar{v}+\bar{v}^2}\end{aligned} \tag{7}$$

Use

$$\int_0^\infty v^2 f(v)dv = \int_0^\infty v^2 \frac{k}{c}(\frac{v}{c})^{k-1}dv = \int_0^\infty c^2 x^{\frac{2}{k}} \frac{k}{c}(\frac{v}{c})^{k-1}dv = \int_0^\infty c^2 x^{\frac{2}{k}} \exp(-x)dx \tag{8}$$

And put $y = 1 + \frac{2}{k}$, then the following equation can be obtained

$$\int_0^\infty v^2 f(v)dv = c^2\Gamma(1+\frac{2}{k}) \tag{9}$$

Hence we get

$$\begin{aligned} \sigma &= \left[c^2\Gamma(1+\frac{2}{k}) - c^2\Gamma^2(1+\frac{1}{k})\right]^{\frac{1}{2}} \\ &= c\sqrt{\Gamma(1+\frac{2}{k}) - \Gamma^2(1+\frac{1}{k})} \end{aligned} \tag{10}$$

2.1 Linear Least Square Method (LLSM)

Least square method is used to calculate the parameter(s) in a formula when modeling an experiment of a phenomenon and it can give an estimation of the parameters. When using least square method, the sum of the squares of the deviations S which is defined as below, should be minimized.

$$S = \sum_{i=1}^{n} w_i^2 [y_i - g(x_i)]^2 \tag{11}$$

In the equation, xi is the wind speed, yi is the probability of the wind speed rank, so (xi, yi) mean the data plot, wi is a weight value of the plot and n is a number of the data plot. The estimation technique we shall discuss is known as the Linear Least Square Method (LLSM), which is a computational approach to fitting a mathematical or statistical model to data. It is so commonly applied in engineering and mathematics problem that is often not thought of as an estimation problem. The linear least square method (LLSM) is a special case for the least square method with a formula which consists of some linear functions and it is easy to use. And in the more special case that the formula is line, the linear least square method is much easier. The Weibull distribution function is a non-linear function, which is

$$F(v) = 1 - \exp\left[-\left(\frac{v}{c}\right)^k\right] \tag{12}$$

i.e.

$$\frac{1}{1-F(v)} = \exp\left[\left(\frac{v}{c}\right)^k\right] \tag{13}$$

i.e.

$$\ln\{\frac{1}{1-F(v)}\} = \left[\left(\frac{v}{c}\right)^k\right] \tag{14}$$

But the cumulative Weibull distribution function is transformed to a linear function like below:
Again

$$\ln\ln\{\frac{1}{1-F(v)}\} = k\ln v - k\ln c \tag{15}$$

Equation (15) can be written as $Y = bX + a$
where

$$Y = \ln\ln\{\frac{1}{1-F(v)}\}, \quad X = \ln v,\ a = -k\ln c,\ b = k$$

By Linear regression formula

$$b = \frac{n\sum_{i=1}^{n} X_i Y_i - \sum_{i=1}^{n} X_i \sum_{i=1}^{n} Y_i}{n\sum_{i=1}^{n} X_i^2 - (\sum_{i=1}^{n} X_i)^2} \tag{16}$$

$$a = \frac{\sum_{i=1}^{n} X_i^2 \sum_{i=1}^{n} Y_i - \sum_{i=1}^{n} X_i \sum_{i=1}^{n} X_i Y_i}{n\sum_{i=1}^{n} X_i^2 - (\sum_{i=1}^{n} X_i)^2} \tag{17}$$

2.2 Maximum Likelihood Estimator(MLE)

The method of maximum likelihood (Harter and Moore (1965a), Harter and Moore (1965b), and Cohen (1965)) is a commonly used procedure because it has very desirable properties.
Let $x_1, x_2, \ldots\ldots\ldots\ldots x_n$ be a random sample of size n drawn from a probability density function $f(x,\theta)$ where θ is an unknown parameter. The likelihood function of this random sample is the joint density of the n random variables and is a function of the unknown parameter. Thus

$$L = \prod_{i=1}^{n} f_{X_i}(x_i,\theta) \tag{18}$$

is the Likelihood function. The Maximum Likelihood Estimator (MLE) of θ, say $\bar{\theta}$, is the value of θ, that maximizes L or, equivalently, the logarithm of L . Often, but not always, the MLE of q is a solution of

$$\frac{dLogL}{d\theta} = 0 \tag{19}$$

Now, we apply the MLE to estimate the Weibull parameters, namely the shape parameter and the scale parameters. Consider the Weibull probability density function (pdf) given in (2), then likelihood function will be

$$L(x_1,x_2,..,x_n,k,c)=\prod_{i=1}^{n}(\frac{k}{c})(\frac{x_i}{c})^{k-1}e^{-\left(\frac{x_i}{c}\right)^k} \tag{20}$$

On taking the logarithms of (20), differentiating with respect to k and *c* in turn and equating to zero, we obtain the estimating equations

$$\frac{\partial \ln L}{\partial k}=\frac{n}{k}+\sum_{i=1}^{n}\ln x_i-\frac{1}{c}\sum_{i=1}^{n}x_i^k\ln x_i=0 \tag{21}$$

$$\frac{\partial \ln L}{\partial c}=\frac{-n}{c}+\frac{1}{c^2}\sum_{i=1}^{n}x_i^k=0 \tag{22}$$

On eliminating *c* between these two above equations and simplifying, we get

$$\frac{\sum_{i=1}^{n}x_i^k\ln x_i}{\sum_{i=1}^{n}x_i^k}-\frac{1}{k}-\frac{1}{n}\sum_{i=1}^{n}\ln x_i=0 \tag{23}$$

which may be solved to get the estimate of k. This can be accomplished by Newton-Raphson method. Which can be written in the form

$$x_{n+1}=x_n-\frac{f(x_n)}{f'(x_n)} \tag{24}$$

Where

$$f(k)=\frac{\sum_{i=1}^{n}x_i^k\ln x_i}{\sum_{i=1}^{n}x_i^k}-\frac{1}{k}-\frac{1}{n}\sum_{i=1}^{n}\ln x_i \tag{25}$$

And

$$f'(k)=\sum_{i=1}^{n}x_i^k(\ln x_i)^2-\frac{1}{k^2}\sum_{i=1}^{n}x_i^k(k\ln x_i-1)-(\frac{1}{n}\sum_{i=1}^{n}\ln x_i)(\sum_{i=1}^{n}x_i^k\ln x_i) \tag{26}$$

Once *k* is determined, c can be estimated using equation (22) as

$$c=\frac{\sum_{i=1}^{n}x_i^k}{n} \tag{27}$$

2.3 Some results

When a location has c=6 the pdf under various values of k are shown in Fig. 1. A higher value of k such as 2.5 or 4 indicates that the variation of Mean Wind speed is small. A lower value of k such as 1.5 or 2 indicates a greater deviation away from Mean Wind speed.

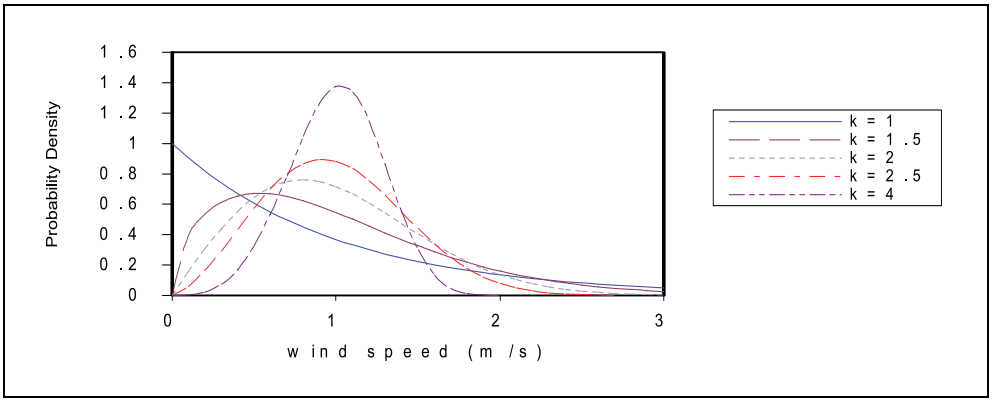

Fig. 1. Weibull Distribution Density versus wind speed under a constant value of c and different values of k

When a location has k=3 the pdf under various valus of c are shown in Fig.2. A higher value of c such as 12 indicates a greater deviation away from Mean Wind speed.

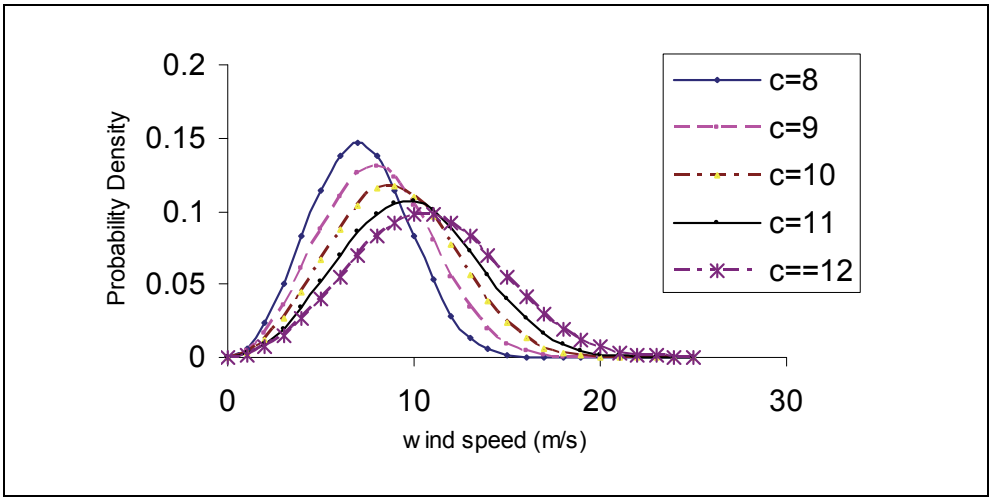

Fig. 2. Weibull Distribution Density versus wind speed under a constant value of k=3 and different values of c

Fig. 3 represents the characteristic curve of $\Gamma\left(1+\frac{1}{k}\right)$. versus shape parameter k. The values of $\Gamma\left(1+\frac{1}{k}\right)$. varies around .889 when k is between 1.9 to 2.6.

Fig.4 represents the characteristic curve of $\frac{c}{v}$ versus shape parameter k .Normally the wind speed data collected at a specified location are used to calculate Mean Wind speed. A good

estimate for parameter c can be obtained from Fig.4 as $c = 1.128\bar{v}$ where k ranges from 1.6 to 4. If the parameter k is less than unity , the ratio $\frac{c}{v}$ decrease rapidly. Hence c is directly proportional to Mean Wind speed for $1.6 \leq k \leq 4$ and Mean Wind speed is mainly affected by c. The most good wind farms have k in this specified range and estimation of c in terms of $\bar{v}$ may have wide applications.

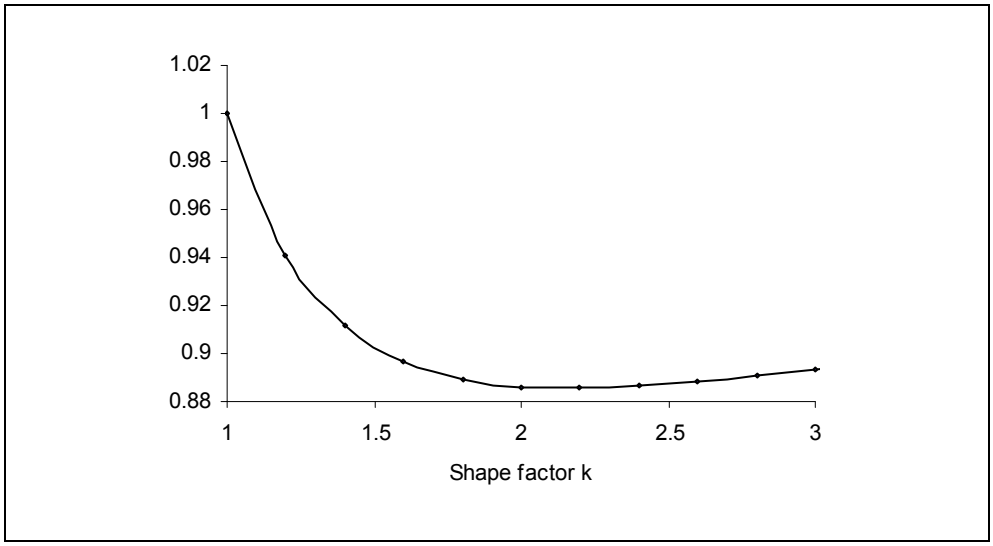

Fig. 3. Characteristic curve of Γ(1+1/k) versus Shape parameter k

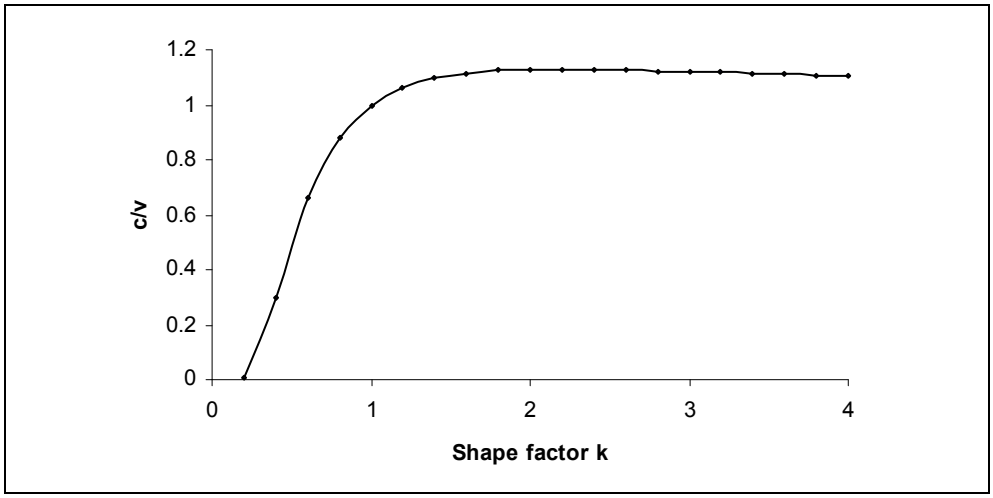

Fig. 4. Characteristic curve of c/ $\tilde{v}$ versus shape parameter k

March, 2009	Wind Speed (m/s)	March, 2009	Wind Speed (m/s)
1	0.56	17	0.28
2	0.28	18	0.83
3	0.56	19	1.39
4	0.56	20	1.11
5	1.11	21	1.11
6	0.83	22	0.83
7	1.11	23	0.56
8	1.94	24	0.83
9	1.11	25	1.67
10	0.83	26	1.94
11	1.11	27	1.39
12	1.39	28	0.83
13	0.28	29	2.22
14	0.56	30	1.67
15	0.28	31	2.22
16	0.28		

Example: Consider the following example where x_i represents the Average Monthly Wind Speed (m/s) at kolkata (from 1st March, 2009 to 31st March, 2009)

Also let $F(x_i) = \frac{i}{n+1}$ and using equations (16) and (17) we get k= 1.013658 and c=29.9931

But if we apply maximum Likelihood Method we get k = 1.912128 and c=1.335916. There is a huge difference in value of c by the above two methods. This is due to the mean rank of $F(x_i)$ and k value is tends to unity.

3. Conclusions

In this paper, we have presented two analytical methods for estimating the Weibull distribution parameters. The above results will help the scientists and the technocrats to select the location for Wind Turbine Generators.

4. Appendix

Those who are not familiar with the units or who have data given in units of other systems (For example wind speed in kmph), here is a short list with the conversion factors for the units that are most relevant for design of Wind Turbine Generators

Length	1m = 3.28 ft
Area	$1m^2$=10.76 ft^2
Volume	$1m^3$ = 35.31 ft^3=264.2 gallons
Speed	1m/s=2.237mph 1knot=.5144 m/s=1.15 mph
Mass	1 kg=2.20 5lb
Force	1N=0.225 lbf=0.102 kgf
Torque	1Nm=.738 ft lbf
Energy	1J= 0.239 Calories= $0.27777*10^{-6}$ kWh= 1 Nm
Power	1 W=1Watt=1 J/s=0.738 ft lbf/s= 1Nm/s 1 hp = 0.7457 kW 1 pk = 0.7355 Kw

5. References

Mann, N. R., Schafer, R. E., and Singpurwalla, N. D., Methods for statistical analysis of reliability and life data, 1974, John Wiley and Sons, New York.

Engelhardt, M., "On simple estimation of the parameters of the Weibull or extreme-value distribution", Technometrics, Vol. 17, No. 3, August 1975.

Mann, N. R. and K. W. Fertig , "Simplified efficient point and interval estimators of the Weibull parameters", Technometrics, Vol. 17, No. 3, August 1975

Cohen, A. C., "Maximum likelihood estimation in the Weibull distribution based on complete and on censored samples", Technometrics, Vol. 7, No. 4, November 1965.

Harter, H. L. and A. H. Moore, "Point and interval estimators based on order statistics, for the scale parameter of a Weibull population with known shape parameter", Technometrics, Vol. 7, No. 3, August 1965a

Harter, H. L. and A. H. Moore, "Maximum likelihood estimation of the parameters of Gamma and Weibull populations from complete and from censored samples", Technometrics, Vol. 7, No. 4, November 1965b

Stone, G. C. and G. Van Heeswijk, "Parameter estimation for the Weibull distribution , IEEE Trans. On Elect Insul. VolEI-12, No-4, August, 1977.

P. Gray and L. Johnson, *Wind Energy System*. Upper Saddle River, NJ: Prentice-Hall, 1985.

W.A.M Jansen and P.T Smulders "Rotor Design for Horizontal Axix Windmills" Development Corporation Information Department, Netherlands, May 1977

Part 2

Environmental Hydrolics

2

Optimizing Habitat Models as a Means for Resolving Environmental Barriers for Wind Farm Developments in the Marine Environment

Henrik Skov
DHI
Denmark

1. Introduction

The recent, rapid growth of offshore wind energy has highlighted significant gaps in our ability to properly assess impacts on wildlife species and habitats. Despite the reported and conceived small and local impacts at small and medium-sized offshore wind farms, the experience with future large-scale wind farms may show otherwise. At the same time the industry now faces daunting logistic and scientific challenges as the construction sites move offshore both in relation to the assessment of the status of habitats and species, and in relation to the estimation of environmental effects.

The key problems are lack of reliable models both of the distributional dynamics and of the habitat displacement and related impacts on populations of the species in question. This situation has hampered decision-making in relation to the management of the offshore wind energy sector by introducing unnecessary conflicts with conservation interests. As shown in this paper habitat models may offer solutions to many environmental barriers by providing data in high spatio-temporal resolution about the distribution of sensitive species.

Detailed data about the distribution of sensitive species is required in order to:

- Predict likely changes in distribution arising from natural dynamic change in the marine environment;
- Evaluate more accurately the potential loss of habitat arising from exclusion (displacement) of priority and sensitive fauna from offshore wind farm areas as induced by disturbance and underwater noise emissions;
- Assess the impact of cumulative habitat loss on priority and sensitive species arising from wind farm construction;
- Avoid conflicts in future offshore wind energy schemes associated with environmentally sensitive areas.

The programmes of biological sampling that are typically carried out for the offshore industry have documented problems associated with biological sampling in a dynamic environment. Even benthic habitats are not stable, and as the weather windows during which sampling of species and habitats is typically undertaken are relatively small interpretation and generalisation of results from baseline surveys is often constrained. Examples of such constraints are the lack of information on the distribution of food supply to higher trophic levels like birds, and the lack of information on the variation of habitats at

the site. Thus, the next generation of habitat models does not only require inclusion of dynamic variables, but also requires the application of a process-based approach which integrates ecosystem models and statistical models.
This paper highlights some examples of integrated, dynamic ecosystem and habitat models, which have been applied in relation to recent offshore wind farm projects in Denmark. Time will tell whether dynamic, process-driven habitat models will form the benchmark for future impact assessments in offshore areas, and whether developers and regulators will have access to solid descriptions of local environmental conditions with lower risks for the appearance of unforeseen impacts and environmental barriers (ON/OFF News, 2010).

2. Limitations of biological sampling in offshore environments and the role of habitat models

Integrated models can enable offshore wind farm projects to better demonstrate ecological sustainability in offshore waters, even in the presence of tight time schedules for baseline investigations. Due to the variability of environmental effect parameters in dynamic offshore environments, the risk exists that major dynamics and changes remain undetected by traditional measurements and monitoring, even following prolonged and intensive sampling campaigns. In most cases, developers will be requested to provide solid descriptions of the environmental baseline conditions based on investigations carried out over a relatively limited period of time. Thus, results of baseline investigations in offshore environments are often constrained due to the following factors:

- Uneven coverage;
- Short weather windows;
- Short baseline period;

This situation may have pronounced financial consequences and may give rise to speculations on the scale of possible effects. The experience from the most recent constructions of offshore wind farms shows that the time schedules under which baseline investigations have to be undertaken will be very tight. In some countries like Germany two years of baseline sureys is mandatory, however in other countries like Denmark baseline studies related to the last large-scale projects (Horns Rev 2, Rødsand 2 and Anholt) were undertaken over just one year. Ecological conditions for many offshore sites on the basis of one year of investigations may not be sufficient to detect major dynamics, and may lead to flawed conclusions on the presence of priority habitats and species at or near the site.

3. From static to dynamic habitat models

Optimization of habitat models in the marine environment requires the development of models which are both sufficiently detailed to describe the realized niche occupied by the species in focus and at the same time sufficiently generalized and parsimonious to be able to predict distributions for a range of environmental scenarios. In other words the next generation of marine habitat models needs to include predictor variables which reflect the whole range of scale-dependent processes which form the basis for the distribution of the species at the site. Since marine processes are dynamic by nature marine habitat models need to be designed in a way which describes the range of dynamics of the key processes driving the distribution of the species.

In the environmental programmes related to two of the latest large-scale offshore wind farm project; Horns Rev 2 (2008-2010) and Anholt (2009-2010) DHI used the MIKE modelling framework (Rasmussen, 1991) to facilitate easy and seamless linking of all models required for the full implementation of a local model in relation to the various aspects of the feasibility, construction and operation of the wind farm. The MIKE modelling framework links the basic hydrodynamic and wave modules to the different modules applied for sedimentation processes, water quality, and benthic pelagic environmental conditions. The water level variation and flows are simulated in response to a variety of forcing functions using a stratified model, MIKE3 (DHI Water & Environment, 2000). The water levels and flows are resolved on an array of nested regular grids.

Benthic habitat models have been developed reflecting the links between the variability of the long-lived elements and bio-coenoces of benthic communities in the regions surrounding the sites in the central Kattegat and the North Sea, and measured/modelled parameters like water depth, sediment, sediment grain size, water temperature, oxygen level, contents of organic matter, light attenuation, plankton density, density of suspended material in the water column etc. The resulting statistical species distribution models are directly coupled to the refined hydrodynamic models which produced temporally resolved predictions of local distribution changes of benthic fauna and flora resulting from natural changes in oceanographic conditions. The statistical models could then be used as a basis for evaluating the change in the distribution of target animals and communities, and the relation to the natural variability of the local ecosystem.

The baseline, impact assessment and monitoring studies carried out in relation to the Horns Rev 2 (Leonhard, 2006; Skov & Thomsen, 2006; Skov et al., 2008) and Anholt (Møhlenberg, 2009; Skov et al., 2009) projects highlighted the benefits of adding model data to the results from traditional surveys. The baseline conditions are used as a yardstick to evaluate the permanent changes in benthic habitats following establishment of the wind farms, and temporal effects related to earth works. The merits of using combined hydrodynamic, sediment and biological models as a basis for estimation of environmental impacts can be summarised as:

- Estimation of the realistic scale of impacts;
- Identification of hydrographic and geomorphologic structures and habitats and estimation of their variability;
- Increase of power of sampled data by provision of physio-chemical data;
- Improvement of understanding of the local dynamics of project site and hence interpretation of changes - especially in relation to regional scale events;
- Evaluation of the similarity of reference and impact sites, incl. re-assessment of the location of the reference areas;
- Evaluation of the extent of the monitoring design in relation to the (modelled) level of impact in monitored areas.

4. Application for offshore wind farm developments

The model design applied for the Horns Rev 2 and Anholt offshore wind farms is based on four model elements:

1. A regional and local hydrodynamic model;
2. An ecological model;
3. A deterministic filter-feeder model;
4. A habitat suitability model.

4.1 Hydrodynamic model

Several numerical 3D flow models have been established within the MIKE modelling framework covering the North Sea and Kattegat. Each of these models has individual strengths. With the purpose of water quality modelling, the so-called BANSAI model (DHI, 2006) was chosen as it has been running operationally since 2001. The model provides input data with regard to the flow field and water quality, and consists of two parts:

- A hydrodynamic module for calculating the evolution in water levels, currents, salinity, and water temperature.
- An ecological module that calculates the spreading of nutrients, the primary production, the biomass, and other ecological parameters.

The main objective of this integrated model system is to calculate the environmental status in the area of the wind farm sites. This includes source apportioning, transport, dispersion, transformation and removal in the coastal and open sea marine waters of nutrients inputs to the North and Baltic Seas. Originally the BANSAI model was created in a collaboration between the Swedish Meteorological and Hydrological Institute (SMHI, Sweden), Finnish Institute of Marine Research (FIMR) and DHI.

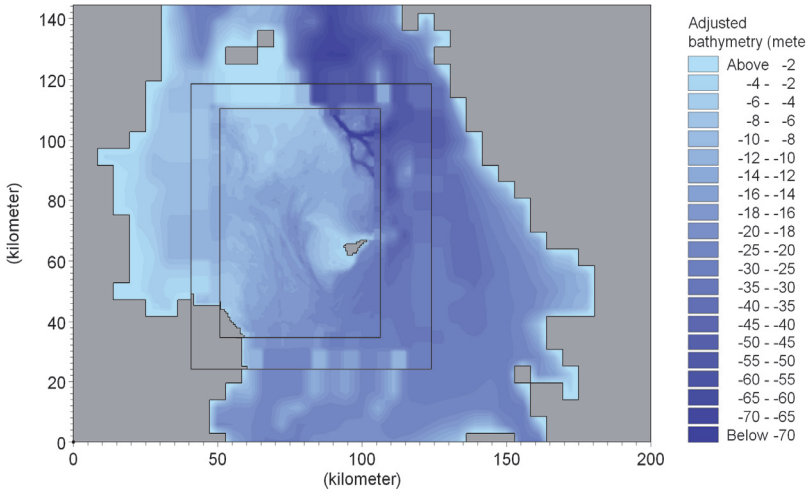

Fig. 1. Example of boundaries and nesting used in the habitat model system for the Anholt offshore wind farm.

The model is using DHI's 3-dimensional model system MIKE3 Classic, which is a fully three-dimensional, non-hydrostatic, primitive equation model (Rasmussen, 1991). It is based on the Reynolds-averaged Navier-Stokes equations and the conservation of mass, salinity and temperature. The prognostic variables are fluid pressure, the three velocity components and the two scalar quantities salt and temperature. In the waters nearest Denmark (the eastern part of the North Sea, Skagerrak, Kattegat, the Belts and the western Baltic) a 3 nautical miles grid is used while a 9 nautical miles grid is used in the North Sea and in the eastern Baltic Sea. The local model applied has this resolution in the outer mesh but by use of the nesting technique this is downscaled by a factor 9 to a resolution of app. 600 m in the area of interest where the wind mills are located. The distance between the wind mills is 600

m – 700 m which means that there will be approximately one wind turbine in each cell in the model area.
The model represents the water column with a 2 m resolution. The model is operational and based on:

- Meteorology;
- Tide, salinity-, temperature and nutrients on the edge of the Atlantic (tide from tidal constituents, salinity and temperature from monthly climatology (ICES), nutrients from climatology supplied with national monitoring data from Denmark and Germany;
- Runoff and nutrient loadings from land (runoff from monthly climatology from HELCOM, OSPAR, national monitoring data) and nutrient loadings from climatology supplied with national monitoring data.

The model was first calibrated based on measurements from the year 2000 and has been continuously improved since then. The representation of salinity in the Belts is extremely important for ecological modelling in the Kattegat, whereas the representation of currents is the key to obtain correct ecological conditions in the eastern part of the North Sea.

4.2 Ecological model

The ecological model consists of an eutrophication model describing the pelagic system with 13 state variables, and seven state variables describing the exchangeable Nitrogen and Phosphorous pools in the sediment (Rasmussen et al., 2009). The pelagic system includes phytoplankton, described in terms of their concentration of carbon (C), nitrogen (N) and phosphorus (P), chlorophyll-a, zooplankton, detritus (C, N & P), inorganic nutrients (dissolved inorganic nitrogen—DIN & PO4–P), total N and P nutrients (including dissolved organic N and P compounds) and dissolved Oxygen (DO). Due to the depth in the wind farm development areas benthic vegetation (i.e. macroalgae) is poorly developed or not existing, and accordingly benthic vegetation is not included in the model. In addition to state variables a large suite of derived variables such as water transparency and secchi depth is modelled and stored during the modelling process. Benthic organisms are not modelled explicitly, but are included as a forcing in the water quality model. Filter-feeding bivalves constitute on average 93% of the entire biomass of benthic invertebrates in the areas, and their filtering activity can exert a significant grazing loss on phytoplankton. Their effect is included in the model by imposing a filtration loss on phytoplankton and detritus in the near bed model layer according to the filtration capacity calculated from length distribution and total biomass of the different species. Because bivalves are not included as a state-variable they do not participate directly in nutrient cycling and accordingly, 50% of filtered algae (C,N,P) are returned as inorganic solutes to the near-bed layer and 50% are entered into the detritus pool subject to sedimentation and remineralisation. Figure 2 shows the state variables and processes for carbon (C) for the pelagic system.
The ecological model was built using the generic equation solver ECOLab that functions as a module in the MIKE 3 simulation software, and ECOLab is linked to the advection-dispersion term of the hydrodynamic flow model, enabling transport mechanisms based on advection-dispersion to be seamlessly integrated into the ECO Lab simulation.
Forcings and boundary conditions of the water quality model follows the line of the forcings and boundaries of the hydrodynamic model, but in addition values for all pelagic state variables at boundaries (Øresund, Southern Kattegat and north of Læsø) and nutrient concentrations in freshwater loads (monthly basis) in addition to atmospheric loads are

included. Boundary values are forced with water quality data extracted from the BANSAI model.

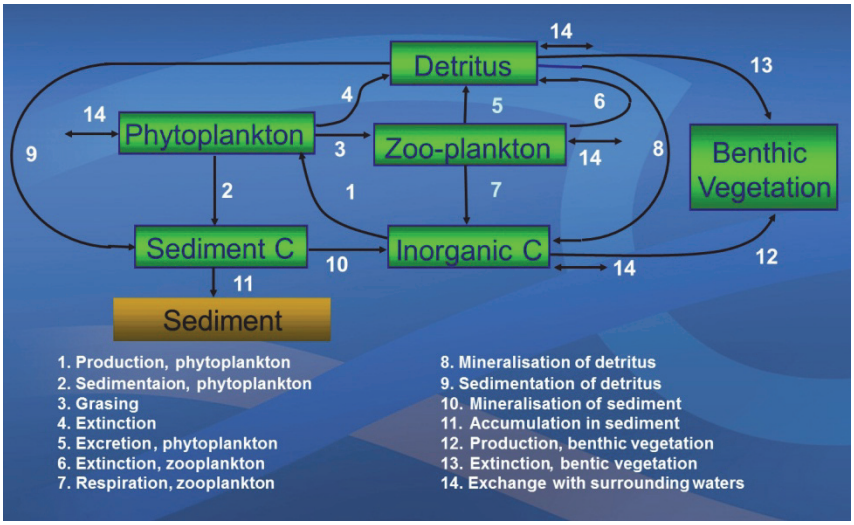

Fig. 2. Schematic diagram showing state variables and processes for carbon in the ecological model established to simulate water quality.

4.3 Filter-feeder model

Carrying capacity models for filter-feeders (FF) were established for epibenthic filter-feeding bivalves exemplified by *Mytilus edulis* and *Modiolus modiolus* and infauna filter-feeding bivalves exemplified by *Arctica islandica* and *Spisula subtruncata* in the Kattegat and infauna filter-feeding bivalves in the North Sea exemplified by *Ensis americanus* and *Spisula subtruncata* using the output from the hydrodynamic and water quality models. The FF models build on the same concept by combining a physiology-based growth and survival model for a standard individual with an advection term that replenish the food ingested by filter-feeders. On a large scale benthic FF for filter-feeders depends on the local primary production and on smaller scale current speed plays an increasing role for FF.

The energy balance of a filter-feeding bivalve can be expressed as: $I = P + R_t + F$, where I = ingestion; P = growth, R_t = total respiration (sum of maintenance respiration, R_m, and respiratory cost of growth, R_g), and F = excretion. Rearranging, growth is expressed as $P = I \times AE - (R_m + R_g)$ or $P = (F \times C \times AE) - (R_m + R_g)$, where $AE = (I - F)/I$ = assimilation efficiency, F = filtration rate, and C = algal concentration. In the individual bivalve growth depends on the quantity (C) and quality of suspended food particles including different species of algae, ciliates and zooplankton organisms along with suspended inorganic material (silt). The maintenance food concentration (which just is sufficient for zero growth) and the maximum growth rate for a standard-sized bivalve differs between species and between populations within species as result of adaptation to local composition and concentration of food (Kiørboe & Møhlenberg, 1981). Energetic growth models are available for many filter-feeders, including *Spisula subtruncata* (Kiørboe et al., 1980) and *Mytilus edulis* (Møhlenerg & Kiørboe, 1981, Kiørboe et al., 1981).

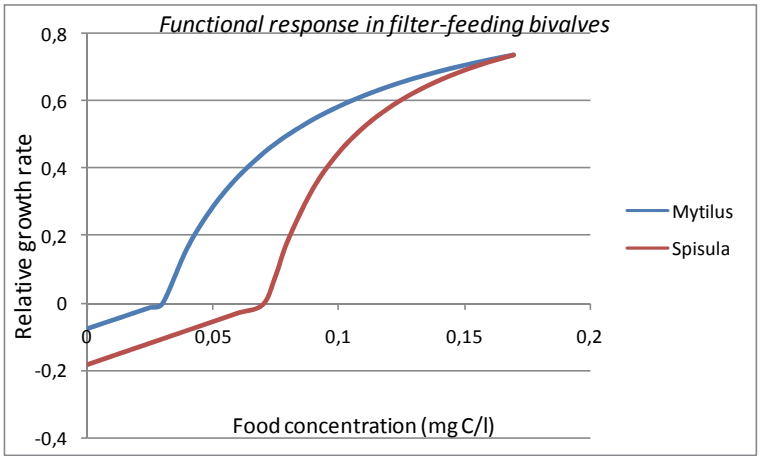

Fig. 3. Comparison of functional response in *Spisula subtruncata* and *Mytilus edulis*.

Important documented evidence for food requirements for *Spisula subtruncata* (Figure 2) includes a rather high maintenance food concentration of 0.072 mgC/l, and that suspended bottom material (i.e. detritus) can constitute up to 30% of assimilated food (Kiørboe et al. (1981). Based on the modelled detritus concentration in the model areas 5% of detritus was assumed to be available for assimilation, hence a growth equation fitted to observed data was developed using non-linear curve-fitting:

For food concentration (PC +0.05*DC) less than 0.072 mg C/l:

Gf = 2.55*(PC+0.05*DC-0.1833)

For food concentration (PC +0.05*DC) above 0.072 mg C/l:

Gf = (PC+0.05*DC-0.072)/(PC+0.05*DC-0.057))

The growth functions described above relate to individual bivalves surrounded by food at constant concentrations. In nature, filter-feeding bivalves aggregate in dense assemblages if current speeds are high, e.g. in tidal areas such as in the Wadden Sea. In low-current environments plankton algae removed by filtration are only slowly replenished and such environments cannot sustain dense populations. Therefore, the growth functions need to be supplemented by an equation that describes the replenishment of food. In *Mytilus* the *in situ* growth rate increases with current speed (Riisgård et al., 1994) and wind-induced turbulence (Sand-Jensen et al., 1994). As bivalves in benthic environments consisting of erodible substrate such as sand cannot maintain their position at current speeds larger than 0.6-1.0 m s^{-1} a bell-shaped current function with an optimum speed at 0.3 m s^{-1} was constructed (Figure 4).
The individual growth function can then be combined with the current function to a 'carrying capacity' index reflecting both individual growth conditions and the density of bivalves that can be sustained:

'CC'-index = Gf * Vf

Controlled experiments of the effects of current speed on growth have only been carried out on oysters, which showed an increase until an optimal current speed of 15 cm s^{-1}, after

which the growth started decreasing. Other bivalve species such as blue mussels increase growth in the field with increasing current speed and wind-induced turbulence until a plateau. This is generally interpreted as a consequence of increasing food availability. Mussels which are settled on substrate like cliffs, stones and foundations may survive and grow in even very energy rich environments (e.g. in current speeds > 60-80 cm s^{-1}), while blue mussels on sandy sediments are unable to establish long-living populations at current speeds exceeding 40-50 cm s^{-1}, probably as a result of erosion.

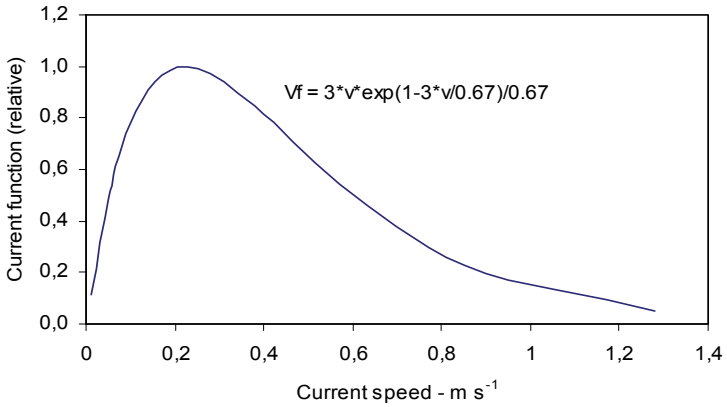

Fig. 4. Current function to describe food replenishment and physical stress in filter-feeding bivalves.

Extended periods with low oxygen concentration can reduce growth and increase mortality in benthic invertebrates including filter-feeders. Such information is included numerically by multiplying the CC-index with a factor (0.8-0.9) for each day oxygen concentration is below 2 mg O_2/l but starting the reduction at day 7 with low oxygen. Also a salinity-dependent function (species-specific) is included in the combined index:

FF-Index=CC index* SF*OF

SF denotes a species dependent salinity index and OF denotes a species independent oxygen index. SF attains values below 1 at salinities less than 20 psu.

The final index for *Mytilus edulis* type in the central Kattegat is shown in Figure 5 for the six years between 2000 and 2005. In general, the index is rather high in the shallow areas at depths less than 12-13 m, whereas at depths larger than 15 m, i.e. where the seabed is located below the pycnocline, the index is rather low due to lower chlorophyll concentrations and lower current speeds. The time series documents a striking stability in the patterns of benthic productivity in the Central Kattegat, and underlines that despite variations the location of the planned Anholt offshore wind farm is always coinciding with the benthic areas of lower productivity.

The model time series of benthic productivity provided a solid basis for the assessment of the importance of the wind farm area to waterbirds. Both baseline and historic survey data unambiguously point at the fact that the waterbirds do not use the wind farm and associated areas with lower carrying capacity for filter-feeding bivalves to any great extent (Figure 6). The areas of high carrying capacity for mussel growth (> 0.15), which match

exactly the most sensitive areas to the waterbirds in the Central Kattegat are located at a minimum distance of 8 km from the wind farm site.

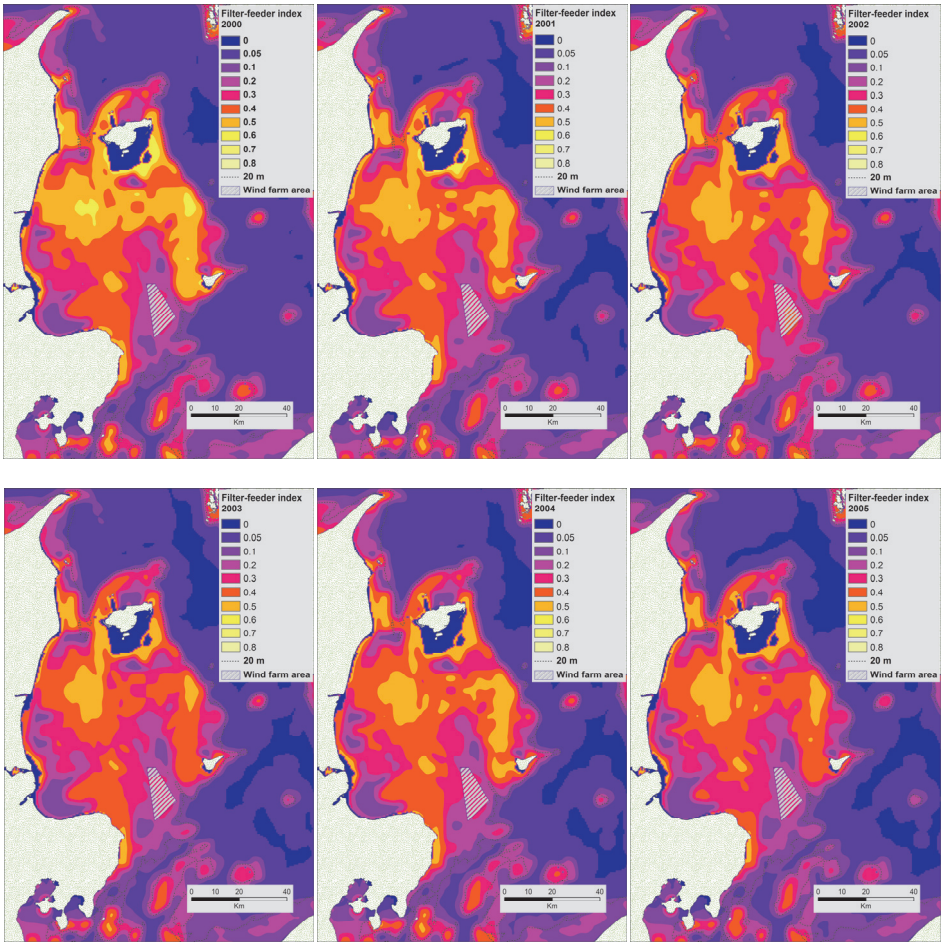

Fig. 5. Modelled mean and annual filter-feeder carrying capacity index for *Mytilus edulis* in the central Kattegat between 2000 and 2005. The planned site for the Anholt offshore wind farm is indicated.

4.4 Habitat suitability model

On Horns Rev, in the North Sea, habitat suitability models were developed on top of the filter-feeder models in order to estimate more precisely the distribution of the two in-fauna bivalves *Spisula subtruncata* and *Ensis americanus*; two key species in the benthic ecosystem of the eastern North Sea whose distribution can only be estimated by the addition of geo-morphological parameters. This was done within the frame of habitat suitability modelling using empirical samples of the two species as response variables and modeled filter-feeder indices, sediment data and data on the depth and relief of the sea floor as predictor

variables. All variables were standardized using 'Box-Cox' normalization (Sokal and Rohlf, 1981), and suitability functions were computed using Ecological Niche Factor Analysis (Hirzel et al., 2002).

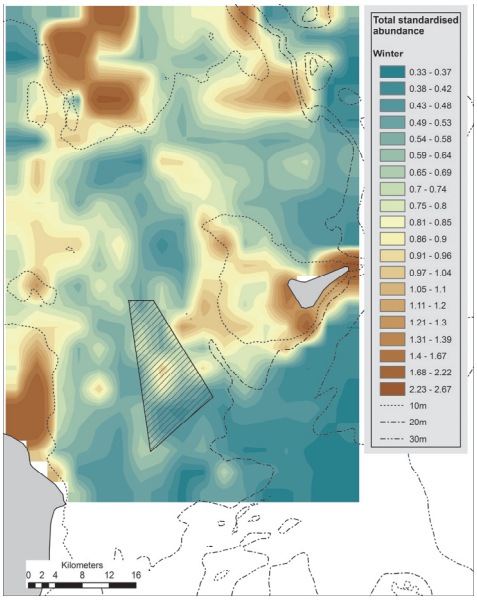

Fig. 6. Index of abundance of waterbirds during winter (species occurring in internationally important concentrations) in the Central Kattegat. The scale is arbitrary. The planned site for the Anholt offshore wind farm is indicated.

Suitability functions compare the distribution of razor clams and trough shells in the multivariate oceanographic space encompassed by the recorded presence data with the multivariate space of the whole set of cells in the modelled area (Hirzel, 2001). On the basis of differences in the bivalve and the global 'space' with respect to their mean and variances, marginality of bivalve records was identified by differences to the global mean and specialisation by a lower species variance than global variance. Thus, for large geographical areas like the part of the North Sea studied here, ENFA approaches Hutchinson's concept of ecological niche, defined as a hyper-volume in the multi-dimensional space of ecological variables within which a species can maintain a viable population (Hutchinson, 1957).
To take account of multi-colinearity and interactions among eco-geographical factors, indices of marginality and specialisation were estimated by factor analysis; the first component being the marginality factor passing through the centroid of all bivalve presence records and the centroid of all background cells in the study area, and the index of marginality measuring the orthogonal distance between the two centroids. Several specialisation factors were successively extracted from the n-1 residual dimensions, ensuring their orthogonality to the marginality factor while maximising the ratio between the residual variance of the background data and the variances of the bivalve occurrences. A high specialisation indicates restricted habitat usage compared to the range of conditions measured in the studied part of Horns Rev. A habitat suitability index was computed on the

basis of the marginality factors and the first three specialisation factors, as a high proportion of the total variance was explained by the first few factors, by comparison to a broken-stick distribution. The habitat suitability algorithm allocated values to all grid cells in the study area, which were proportional to the distance between their position and the position of the species optimum in factorial space.

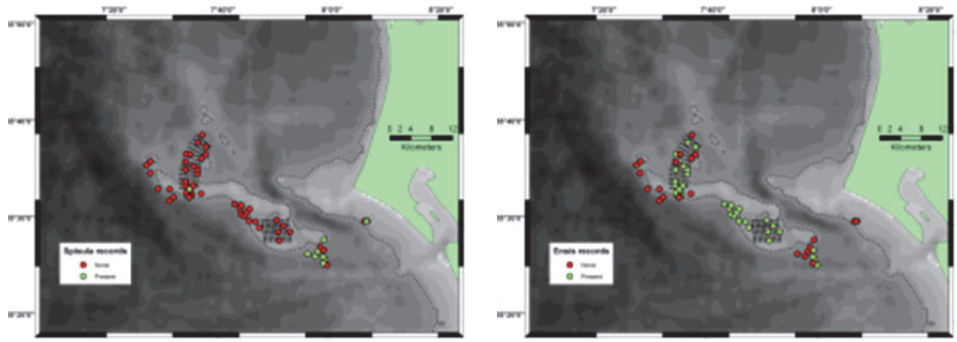

Fig. 7. Available empirical data on the presence/absence of Cut trough shells (left) and American razor clams (right) on Horns Rev.

Application of ENFA provided an overall marginality of m = 3.92 and an overall specialization value of S = 2.734 for Ensis and m = 0.527 and S = 4.654 for Spisula, showing that Horns Rev habitats for the two species during 2000-2007 differed markedly from the mean conditions in the studied part of the North Sea. The three factors retained accounted for more than 93 % of the sum of the eigenvalues (that is 100 % of the marginalization and 95 % of the specialization). Marginality accounted for 50.9 % of the total specialization in Ensis and 81.6 % in Spisula. The two first specialization factors accounted for 41 % of the total specialization in Ensis and 11.7 % in Spisula, indicating that the two species are moderately restricted in the range of conditions they utilize in the study area, with trough shells being more restricted.

Marginality coefficients showed that razor clams were (positively) linked to water depth, areas with relatively flat terrain and the carrying capacity index, while trough shells showed strong links to median grain size (negative coefficient) and the carrying capacity index. These scores can easily be interpreted on the basis of the plotted presence/absence data, which indicate that razor clams mainly use offshore areas and are found commonly around and on Horns Rev, whereas trough shells are mainly found in the eastern-most, near-coastal areas. The marginality and specialization scores lead to habitat suitability scores ranging from 0-100, the upper 33 reflecting suitable habitat (Figures 8, 9). The pixels indicating high habitat suitability for razor clams mainly lie within a coherent zone corresponding to the Horns Rev and moderate slope areas to the northwest and southeast, including the wind farm areas on Horns Rev (Figure 8). The pixels indicating high habitat suitability for trough shells (Figure 9) are confined to the area of fine sediments and high carrying capacity values in the south-eastern and eastern-most part. In most years, the wind farms areas have low suitability for trough shells, and intermediate suitability is only estimated for the Horns Rev 1 wind farm on the eastern part of Horns Rev.

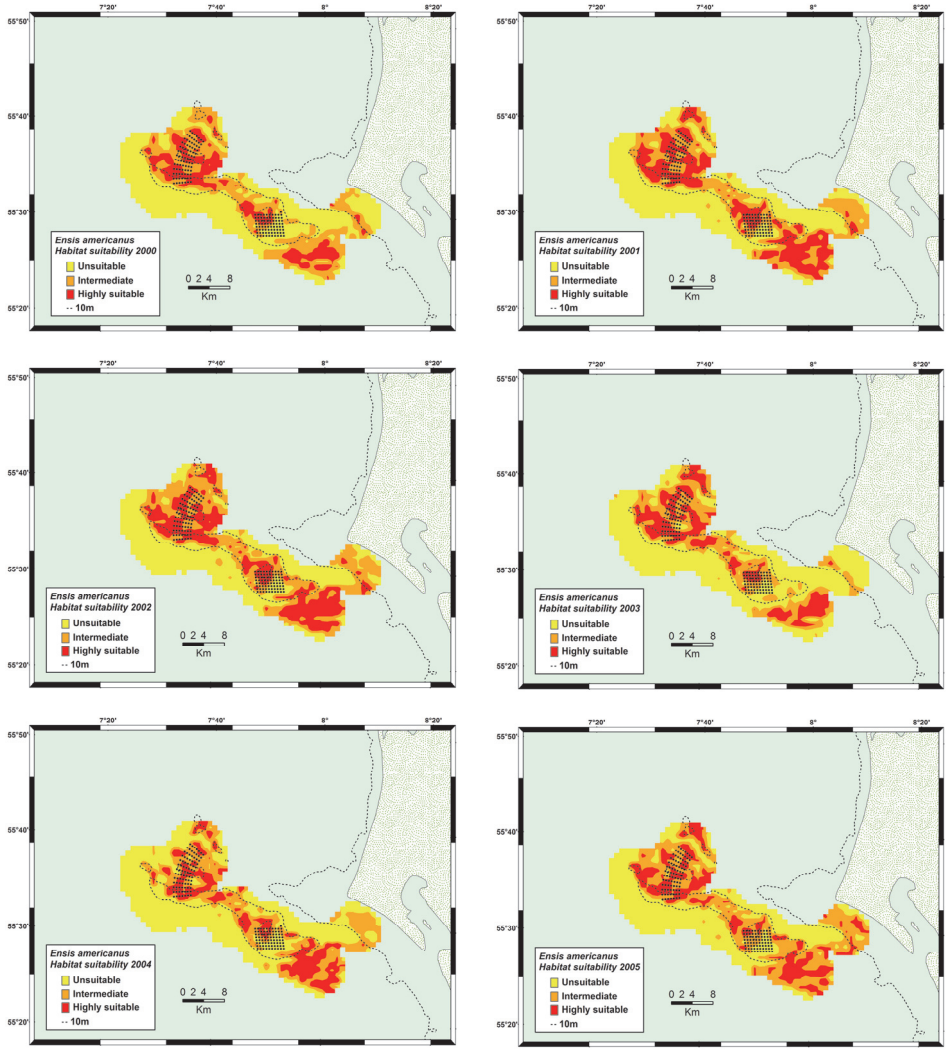

Fig. 8. Modelled annual habitat suitability for American razor clam *Ensis americanus* on Horns Rev for the period 2000-2005. The two offshore wind farms Horns Rev 1 and Horns Rev 2 are marked as black dots.

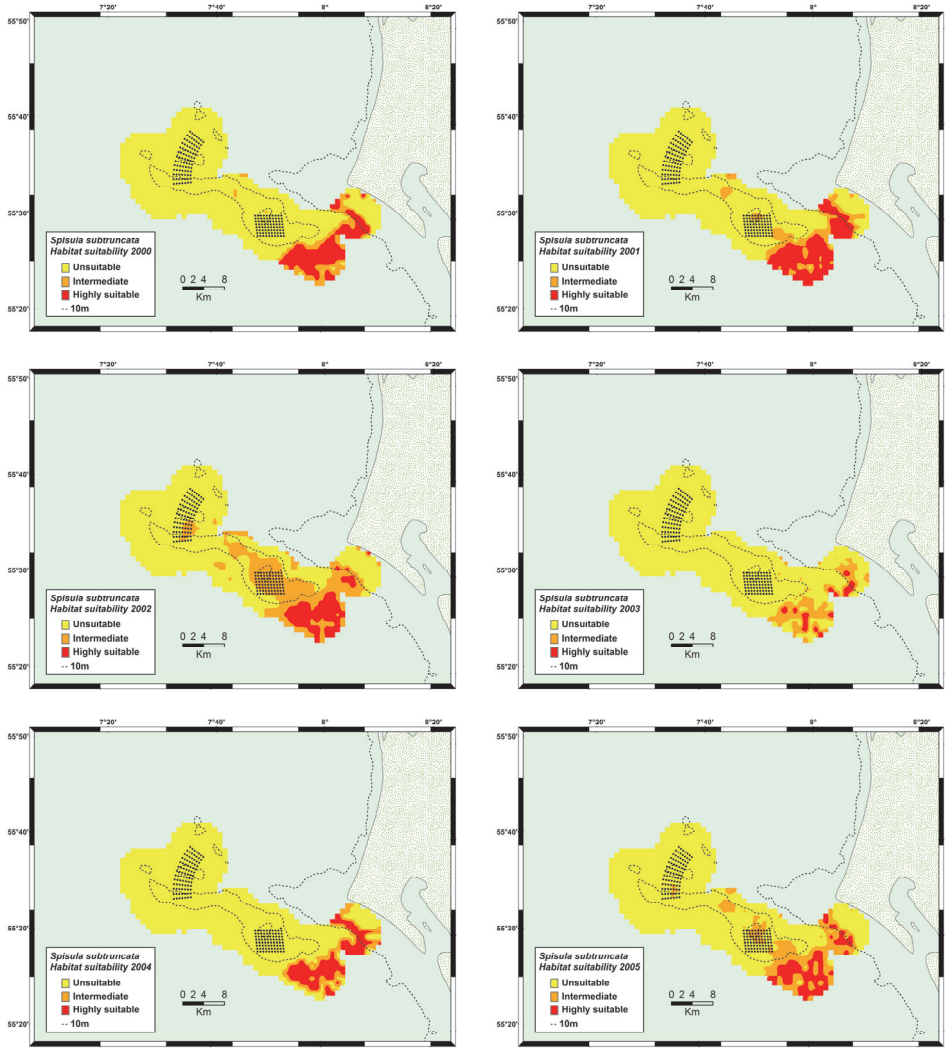

Fig. 9. Modelled annual habitat suitability for Cut trough shell *Spisula subtruncata* on Horns Rev for the period 2000-2005. The two offshore wind farms Horns Rev 1 and Horns Rev 2 are marked as black dots.

The time series of suitable habitat to razor clams and trough shells on Horns Rev enabled the prediction of the distribution of benthic-feeding waterbirds, and assessment of the importance of the wind farm area to sensitive species like Common Scoter *Melanitta nigra* (Figure 10). The predicted distribution of the Common Scoter shows the Horns Rev 1 wind farm area as of low importance, and the Horns Rev 2 wind farm area of medium importance.

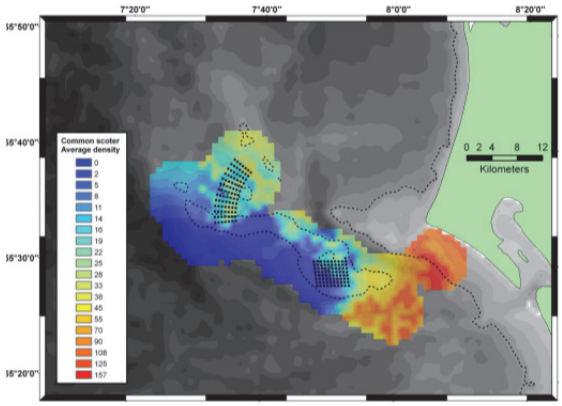

Fig. 10. The average density (number of birds/km^2) of Common Scoter *Melanitta nigra* at Horns Rev modelled for six aerial surveys between December 2007 and April 2008. The two offshore wind farms Horns Rev 1 and Horns Rev 2 are marked as black dots.

5. Conclusion

The environmental investigations related to the Anholt and Horns Rev 2 offshore wind farm projects are illustrative examples of the fact that the integration of traditional sampling and advanced habitat modelling make it possible to achieve a robust assessment of baseline conditions and ecological impact within the relatively short period of time available. Time will tell whether these projects represent a benchmark for future impact assessments in offshore areas, and whether developers and regulators will have access to solid descriptions of local environmental conditions with lower risks for the appearance of unforeseen impacts and environmental barriers.

6. Acknowledgement

The modeling activities related to the Anholt offshore wind farm project were carried out as part of the Rambøll/DHI contract with EnergiNet.Dk, and the activities related to the Horns Rev 2 project were carried out as part of the Orbicon/DHI contract with DONG Energy.

7. References

DHI Water & Environment. (2000). *MIKE 3: Environmental Hydraulics*. DHI Software User Guide, Documentation and Reference Manual.

DHI. (2006). *Baltic Sea – North Sea Transition Area*. Environmental status year 2004. Bansai Project. Technical note for the Nordic Council of ministers.

Hirzel, A.H., 2001. *When GIS come to life. Linking landscape- and population ecology for large population management modelling: the case of Ibex (Capra ibex) in Switzer-land.* PhD thesis. Institute of Ecology, Laboratory for Conservation Biology. University of Lausanne, 114 pp.

Hirzel, A.H., Hausser, J., Chessel, D., Perrin, N. (2002). Ecological-niche factor analysis: How to compute habitat- suitability maps without absence data? *Ecology* 83: 2027-2036.

Hutchinson, G.E. (1957). Concluding remarks. In: *Cold Spring Harbour symposium on quantitative biology*, Vol. 22, pp. 415-427.

Kiørboe, T. & F. Møhlenberg. (1981). Particle selection in suspension feeding bivalves. *Mar. Ecol. Prog. Ser*. 5: 291-196.

Kiørboe, T., Møhlenberg, F. & O. Nøhr. (1980). Feeding, particle selection and carbon adsorption in Mytilus edulis in different mixtures of algae and resuspended bottom material. *Ophelia* 19: 193-205.

Kiørboe, T., Møhlenberg, F. & O. Nøhr. (1981). Effect of suspended bottom material on growth and energetics in Mytilus edulis. *Mar. Biol.* 61: 283-288.

Leonhard, S.B.L. (2006). EIA Report. *Benthic communities*. Horns Rev 2 Offshore Wind Farm. Report request. Commissioned by DONG Energy. Orbicon A/S.

Møhlenberg, F. (2009). *400 MW Off-shore wind park in Kattegat*. *Habitats*. Report to EnergiNet.Dk. DHI.

Møhlenberg, F. & T. Kiørboe. (1981). Growth and energetics in Spisula subtruncata (da Costa) and the effect of suspended bottom material. *Ophelia* 20: 79-90

ON/OFF News. (2010). DHI behind advanced ecological and habitat modelling technologies. ON/OFF News November 2010: 14-16.

Rasmussen, E.B. (1991). A finite difference scheme for three dimensional modelling of fluid dynamics. *Proceedings of IAHR*, Madrid, Spain: 339-348.

Rasmussen, E.K., Svenstrup Petersen, O., Thompson, J.R., Flower, R.J. & M.H. Ahmed. (2009). Hydrodynamic-ecological model analyses of the water quality of Lake Manzala (Nile Delta, Northern Egypt). *Hydrobiologia* 622: 195-220.

Riisgård, H.U., Clausen, I., Møhlenberg, F., Petersen, J.K., Olesen, N.,J., Christensen, P.B., Møller, M.M. & P. Andersen. (1994). Filtratorer, planktondynamik og biologisk struktur i Kertinge Nor. Miljøstyrelsen, 75 sider. – Havforskning fra Miljøstyrelsen, nr. 45.

Sand-Jensen, K., Borum J, Geertz-Hansen, O., Jensen, J.N., Josefson, A.B., Møhlenberg, F. & B. Riemann. (1994). Resuspension og stofomsætning i Roskilde Fjord. Miljøstyrelsen 69 sider. – Havforskning fra Miljøstyrelsen nr. 51.

Skov, H., Thomsen, F. (2006). *EIA report marine mammals*. Horns Rev 2 Offshore Wind Farm. Report to DONG Energy. Bio/Consult AS, DHI Water & Environment, Biola, Arhus, Denmark

Skov, H., Piper, W., Leonhard, S.B.L. (2008). *Horns Rev II wind farm*. Monitoring of waterbirds. Baseline Studies 2007-08. Report request. Commissioned by DONG Energy. Orbicon A/S & DHI.

Skov, H., Krogsgaard, J., Piper, W., Durinck, J. (2009). *Anholt Offshore Wind Farm. Birds*. Report to EnergiNet.Dk. DHI.

Sokal, R.R. & Rohlf, J.F. (1981). *Biometry: the principles and practice of statistics in bio-logical research.* 2nd ed., W. H. Freeman and Company, San Francisco.

Part 3

Power System Control

3

Technical Framework Conditions to Integrate High Intermittent Renewable Energy Feed-in in Germany

Harald Weber[1], Christian Ziems[1] and Sebastian Meinke[2]
[1]*Institute of Electrical Power Engineering*
[2]*Department of Technical Thermodynamics*
University of Rostock
Germany

1. Introduction

The first part of this chapter gives a short overview about the general problems of integration. Therefore a control theory based description of the basic fundamentals of the power system control concepts is given.
The second part of the chapter concentrates on the technical framework conditions of conventional power plants to follow the intermittent power feed-in because as long as no large-scale storage systems are available these conventional power plants will be necessary to integrate the renewable energy at least for the next 20 years. Therefore different methods and tools to analyze and simulate the power plant scheduling and to determine the additional life time consumption of highly stressed components of fossil fueled power plants will be presented and illustrated by different scenarios.

2. German ambitions for renewable energy until 2050

In Germany the existing electrical generation system is going to be essentially influenced due to the continuously increasing influence of intermittent renewable energy sources. Because of the massive expansion of the total number of wind turbines, especially in the northern part of Germany within the last years, wind power now plays the most important role concerning the renewable energy sources in Germany.
At the end of 2010 the installed capacity of wind turbines amounted to more than 27.2 GW. Besides the photovoltaic capacities are increasing so fast, that at the end of 2010 there was more than 17.4 GW of installed capacity for photovoltaic systems. In the photovoltaic sector this was an increase of about 80 % compared to 2009.
Despite of a stepwise reduction of the legal refunds for the electrical energy produced by photovoltaic systems and wind turbines in Germany within the next 10 years, current predictions yield to about 50 GW of installed capacity for photovoltaic systems and an installed capacity of wind turbines of more than 51 GW in 2020. This means that there will be probably more than 100 GW of wind and solar power generation installed in Germany by the end of the decade. Therefore the share of electrical energy produced by these two

renewable sources could increase from 8.6 % in 2010 to more than 35 % in 2020 of the German electrical net energy consumption.
In regard to a peak load of 85 GW and an off-peak load of only 45 GW there will be new challenges to integrate such a high intermittent power feed-in into the existing electrical generation system. Until now there are only the fossil and nuclear power plants available to balance the renewable energy production and to follow the wind and solar power production in a complementary way. But due to the increasing fraction of intermittent renewable energy sources within the generation system the number of available synchronized conventional power plant generators will be reduced continuously especially in periods with high renewable power feed-in. Since the system stability depends on the availability of flexible power stations, sufficient spinning reserves and certain system inertia, the robustness of the electrical power system will reduced towards suddenly appearing disturbances of the power balance.
Due to the limited fossil and nuclear resources that we use today and the high carbon dioxide emissions and nuclear waste production to produce more than 80 % of the German electrical energy, Germany has to exploit new energy sources that are available in an unlimited way. Therefore in the 21st century the renewable energies will become the most important field of research in several domains of technology. Wind and solar energy are available nearly everywhere in Germany. But it will depend on several economical boundary conditions which kind of technology will be the best to gain an efficient access to this unlimited energy supply.
Of course in regard to the relevance of solar energy it would be the most efficient way to generate the electricity where the solar energy supply is naturally the highest. But unfortunately these regions are often far away from the areas with the high population and consumption density. For example it would be possible to cover the total worldwide energy consumption by just covering a very small fraction of the desert areas like the Sahara in North Africa, but a very powerful transportation system for electrical energy is needed that has to consist of various high voltage transmission lines that can deliver the energy to the consumers. In Europe for example the consumers are several thousand kilometers away from the desert areas and of course Europe is separated from the continent of Africa by the Mediterranean Sea. So it would be necessary to use cable systems to connect this intercontinental sea distance which are very cost-intensive compared to overhead lines.
These new transmission line systems will cause very high capital expenditures that can't be raised in the near-term future. This funding, on the one hand for the transmission line systems and of course on the other hand for the solar generators like Concentrated Solar Power (CSP) stations or photovoltaic (PV) systems, has to be invested in the long-term future. Although in Europe there is a first ambitious entrepreneurship called Desertec, that proposed to it selves that it could be possible to build up such a renewable solar and wind generation system in North Africa within the next decades, earliest in 2050 almost 15 % of the electrical energy consumption of entire Europe could be covered. But in regard to the security of supply it has to be mentioned that there is always a certain risk in dependence to other countries especially when the political systems are not stable in these countries.
So to fulfill the German goals and to be less dependent from foreign political issues it is necessary to use the renewable energy sources that are available on the German land and sea area to increase the fraction of renewable energy in the electrical energy system from 18 % today up to 40 % until 2020 and up to 80 % until 2050.
The potential especially for wind energy is very high in Germany. Naturally the solar energy potentials aren't as high as in southern Europe or North Africa but nevertheless it is still worthwhile to exploit this renewable energy source with photovoltaic systems. In

Germany hydro power is already exploited to a great extent and biomass and geothermal energy aren't capable to contribute big proportions of the energy consumption. Therefore only the intermittent energy sources like wind and photovoltaic power can be used to deliver a high proportion of the total energy demand.
But unfortunately these two energy sources have a very disadvantageous characteristic. They occur in an intermittent way and they aren't reliable. Furthermore the energy supply of wind and solar generators do not correlate to the overall energy consumption. From the consumers point of view this makes it impossible to operate an electrical generation system without any backup power plants that are supplied by big storage systems. Besides these backup power stations are necessary to ensure the safety of supply at any time even when the system is disturbed by suddenly appearing technical outages of any electrical equipment of the generation system. Moreover fast reacting generators are essentially needed especially when the wind and solar energy occurrence is decreasing due to changing meteorological conditions.

3. The electrical generation system as a controlled system: frequency – active power – control

To understand the fundamental problems of the integration of intermittent renewable energy sources into the electrical generation system it is very important to understand the control structure of the system. Therefore in the following subsections a more detailed description of the electrical generation system, which is precisely a controlled system, will be given.
Worldwide the electrical energy supply is operated with a three-phase network. Three-phase rotary current is used instead of single phase Alternating Current (AC) because its behavior towards the transmission of energy is similar to a rotating mechanical shaft which is continuously delivering power. But this virtual "electrical shaft" is not emitting noise nor is it necessary to lubricate it. From the powered generator shaft to the slowing down motor shaft the three-phase rotating current network therefore behaves like a warped torsion shaft under workload that rotates with 50 rotations per second. Hence the electrical switch- and transformer-stations act like mechanical gearboxes that are connected to several distribution shafts which are connected with the consumers. The consumer can use these distribution shafts to perform mechanical work or to produce light or heat by the cause of friction. The shafts are driven by different mechanical power drives which care for the n_T=50 rotations per second and provide the torque M_T which is required for the delivered power P_T according to:

$$P_T = M_T \cdot \Omega_T = M_T \cdot 2 \cdot \Pi \cdot n_T \tag{1}$$

This torque is produced by turbines that are classed into thermal, gas fired and hydraulic. To ensure a long life time of the power drives the rotational speed n_T has to be kept as constant as possible. Therefore only the torque M_T can be adjusted which means more or less steam, gas or water onto the turbine. The turbines consist of rotors which have an inertia Θ. But a rotating mass is only able to change its rotational speed if the sum of working torques is changed according to:

$$\Theta \cdot \dot{\Omega}_T = (M_T - M_V) \tag{2}$$

Here M_V is the delivered load torque: If M_T increases the system accelerates, if M_V increases the system slows down. The rate of acceleration or deceleration of the whole system is significantly determined by the inertia Θ. Hence if the inertia would be reduced the rotational speed change rate would increase, too.
To summarize this first part it can be outlined that if the mechanical system wouldn't emit noise and if it wouldn't be necessary to lubricate the components, the energy supply systems could be realized with pure mechanical components. To understand the frequency – active power – control loop it is therefore sufficient to understand the controlled mechanical energy supply system.
In control engineering usually per unit (p.u.) values are used for different physical values. These per unit values are referenced to their nominal value. If furthermore is assumed that the rotational speed n_T and therefore Ω_T isn't changed noteworthy, equation (2) can be constituted as:

$$\Theta \cdot \Omega_N \cdot \dot{\Omega}_T = (P_T - P_V) \tag{3}$$

If the nominal values P_G and Ω_N are introduced, equation (3) can be written as:

$$T_G \cdot \dot{f} = (p_T - p_V) \tag{4}$$

The values indexed with G stand for values referenced to the whole network. Here f is the per unit system frequency or rotational speed. T_G is called the acceleration time constant and it is calculated by:

$$T_G = \frac{\Theta \cdot \Omega_N^2}{P_G} \tag{4a}$$

The acceleration time constant, which is calculated by the inertia of the generators and motors, commonly states how much time it takes from standstill to accelerate an inertia that is driven by its nominal torque or power until the nominal rotational speed is reached. Within the electrical energy system the inertia is of vital importance, since only the inertia is able to stabilize the network frequency at an acceptable value in the first moment after a disturbance of the power balance. Normally wind turbines are connected to the system via frequency inverters and photovoltaic systems are always connected via DC/AC converters, so they are mechanically and electrically decoupled from the system and can not increase the acceleration time constant. Therefore it is has to be lined out that the acceleration time constant is reduced if more and more wind turbines and photovoltaic panels are connected to the system when at the same time the number of conventional power plant generators with masses are displaced by these intermittent generators while the total nominal power value of the whole system remains constant.

3.1 The primary control

With the use of the Laplace transform equation (4) can be stated according to:

$$\Delta f = \frac{1}{s \cdot T_G}(\Delta p_{G_E} - \Delta p_{G_V}) \tag{5}$$

The values indexed with G stand for values referenced to the whole network, index E for the generation and V for the consumption. This equation of motion is the basis of the control orientated modelling structure of the primary control of a total network shown in Fig. 1. Here the frequency f is stated as the deviation from the desired network frequency that is 50 Hz in Europe. Furthermore the following assumption was made: All power plants and consumers are connected to a single node network model; this means the transmission lines or transmission shafts between them are neglected. Therefore only one network frequency exists. The losses are allocated to the consumers. p_{GE} describe the total power generation and p_{GV} the total power consumption in per unit values. With this kind of model the whole European generation system of the ENTSO-E from Portugal to Poland and Denmark to Turkey with a total nominal power of P_G = 300 GW can be described.
Due to the dependency of the power consumption of motors on the network frequency the real absorbed power p_{GV} is corrected by the frequency dependent change of power Δp_{GVf} according to:

$$\Delta p_{GV_f} = \frac{1}{\sigma_{G_V}} \cdot \Delta f \tag{6}$$

This behaviour is called the consumer self-controlling effect which is expressed by σ_{GV}. The mean value for this value is 200 % in Germany. Therefore the consumers itself acts like a control loop because they reduce their power consumption if the frequency decreases and they increase their power consumption if the frequency increases. Hence in Fig. 1 the magenta-hued total consumer has three single paths:

1. The actual operating point of the consumed power
2. The always occurring disturbance of the system because of consumer re- and disconnections from the system
3. The frequency dependent power consumption of the motoric consumers

The operating point "consumed power" is the forecasted power demand of the total network at a certain hour of the day. All deviations from this value result in the disturbance signal "consumer re- and disconnection". The operating point "consumed power" has to be covered by the existing power plants. In Fig. 1 this is symbolized by the "scheduled power". The operating point "secondary control power" will be described later. For now it can be assumed to be zero.
If now is assumed that only the consumer self-controlling effect would take effect, the deviation of the network frequency from the nominal value of 50 Hz would increase to a non-permissible extent. In Fig. 2 this deviation is illustrated by the green line for a step disturbance of the consumed power of 1 % of the nominal power. For the European network with a nominal power of P_G = 300 GW this is equal to a disturbance of 3 GW. The primary control is designed to handle such a disturbance at the maximum and to compensate the power deficit completely. This maximum disturbance is equal to the outage of two French nuclear reactors of the nuclear power plant Tricastin. As withdrawn in Fig. 2 the frequency deviation amounts to Δf = -0.02 pu = -2 % or -1 Hz. In the case of such a high frequency deviation first consumers would be automatically disconnected from the system to ensure the safety of supply and to protect electrical components.

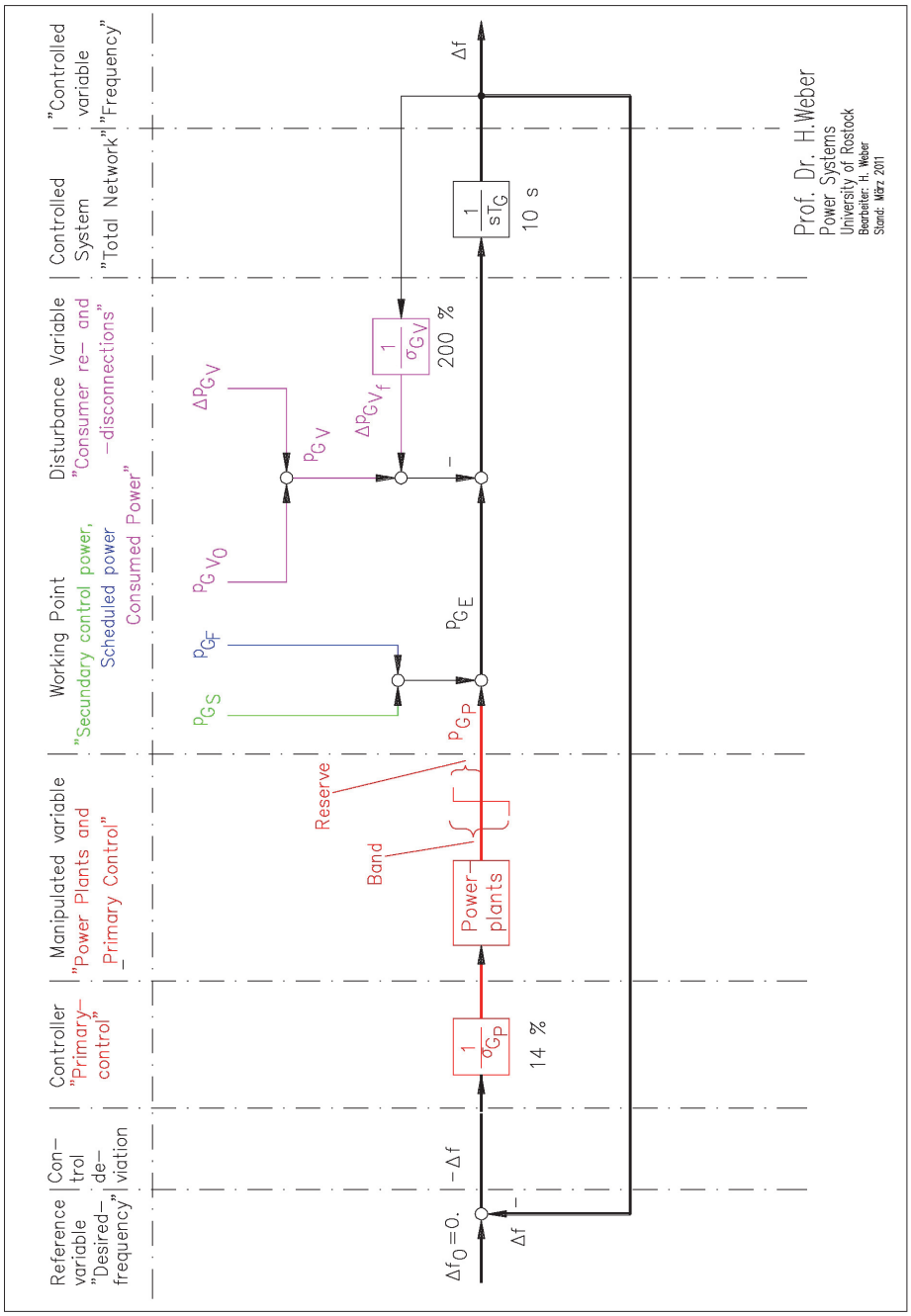

Fig. 1. Control oriented scheme of the primary control

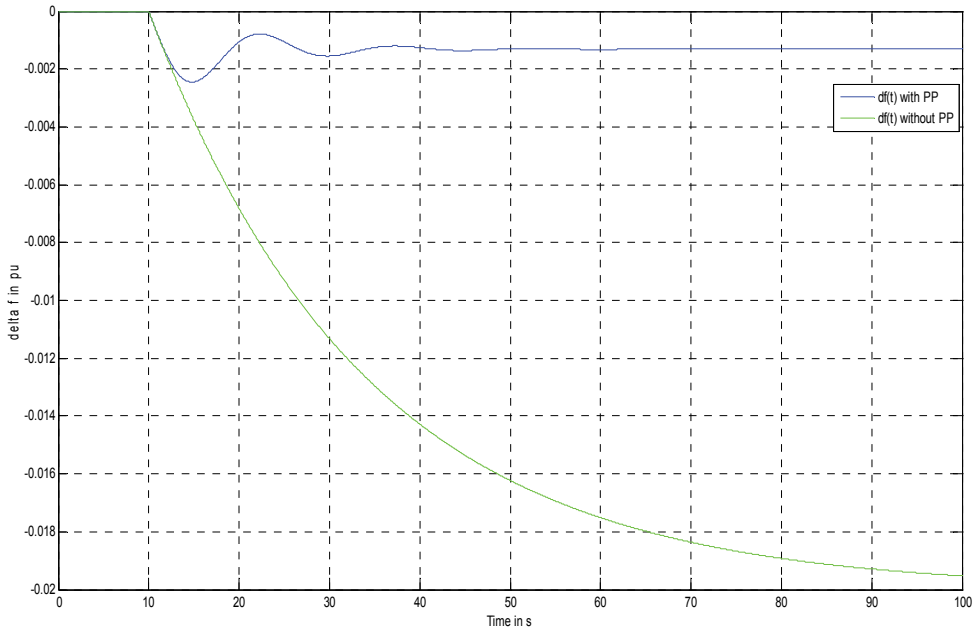

Fig. 2. Frequency deviation in pu while Δp_{GV} = +1 %

The step-shaped disturbance of the consumed power of 1 % has to be covered at any time. In Fig. 3 the different types of power are shown that cover this additional consumed power: The blue line shows the reduction of the real consumed power due to the consumer self-controlling effect according to equation (6), the green line shows the accelerating power that is delivered by the inertia of each rotating mass that slows down corresponding to equation (7). As outlined by this graph in the first moment the required power is delivered by the accelerating power that is provided by the decelerating rotating masses and later by the consumer self-controlling effect which is reacting due to the decreasing frequency.

$$p_{G_{acc}} = -T_G \cdot \Delta\dot{f} \tag{7}$$

In the future the electrical generation system will be characterized by inertia-free energy converters like frequency inverter controlled wind turbines and photovoltaic panels, so the accelerating power has to be generated synthetically with power electronics to safe the grid control and to ensure the system stability any longer.
In the control orientated structure of Fig. 1 the controller "primary controller" and the manipulated variable "primary control power" are shown. This primary reserve power has to be reserved in all power plants that are connected to the system. Due to this primary reserve power the frequency deviation is kept in an acceptable tolerance range which is illustrated by the blue line in Fig. 2. Here the frequency deviation remains within -200 mHz in regard to a steady state evaluation if a σ_P of 14 % is assumed.

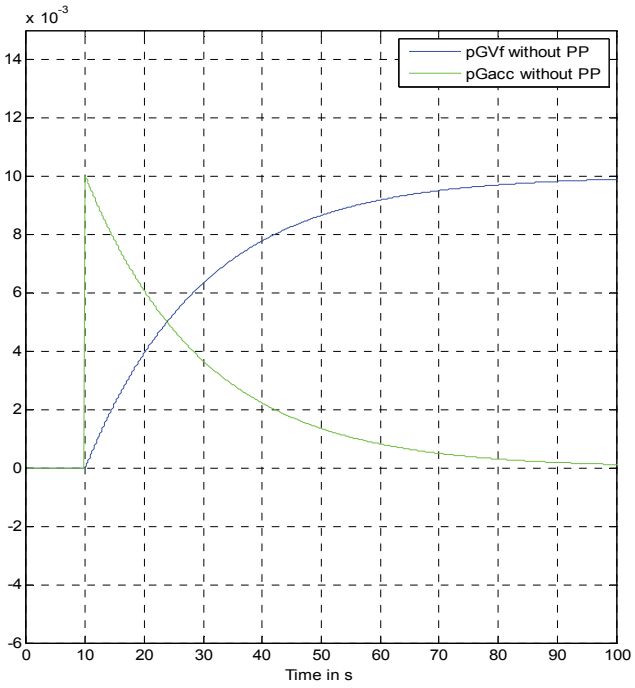

Fig. 3. Disturbance of the power balance covered by accelerating power and the consumer self-controlling effect

In this context in Fig. 4 the accelerating power is shown again. Here now the primary control (red line) almost entirely takes over the disturbance slightly supported by the consumer self-controlling effect. This transition process proceeds oscillating as well as the corresponding frequency change. The related power plant model was simplified to two PT1-elements with the time constants T_{K1} = 0,8 s and T_{K2} = 6 s.
In the future as mentioned before the acceleration time constant T_G will be reduced due to the increasing amount of renewable generation from wind and photovolaics because of the loss of inertia. In Fig. 5 is shown the effect of a reduced inertia. Therefore the network acceleration time constant is reduced from 12 s to 6 s and then to 2 s. As illustrated in the three lines of diagrams at the beginning the frequency deviation increases, the network behaviour gets "softer", although the disturbance remains constant in all three cases. This behaviour will continue until the primary controller stability is lost completely in the third scenario due to the lack of sufficient inertia.

3.2 The secondary control

The operating point "secondary control" in Fig. 1 remained zero in case of the aforementioned primary control action which acts in the domain of seconds. This caused a remaining steady state deviation of the frequency as shown in Fig. 2. This deviation is now corrected by the secondary control within the domain of minutes whereby this process has to be finished after 15 minutes.

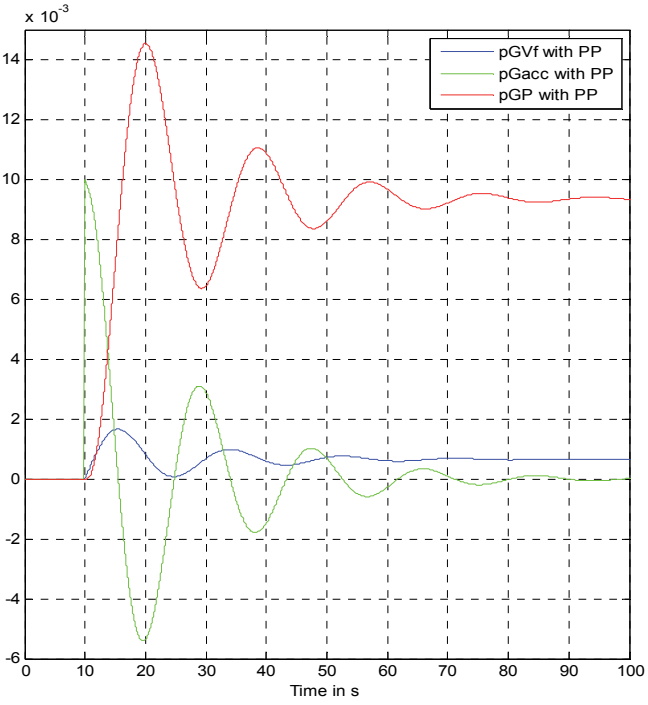

Fig. 4. Disturbance of the power balance covered by accelerating power, the consumer self-controlling effect and the primary control

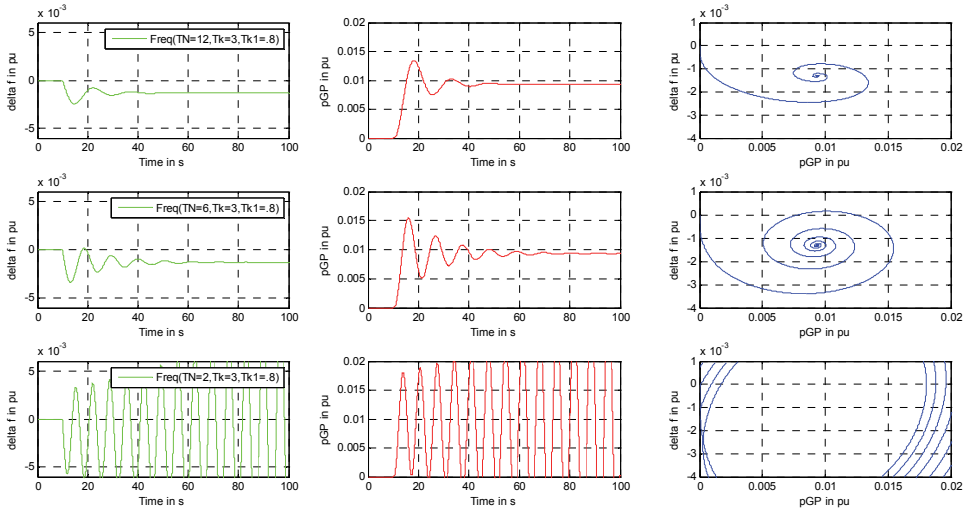

Fig. 5. Effect of a reduced acceleration time constant due to reduced inertia onto the primary controller stability

Furthermore the secondary control has to determine in which control area of the system the disturbance occurred because only the disturbed control area should compensate the disturbance. In this context it is important to consider the scheduled exchange power between different control areas, too. The secondary control detects the disturbance by the use of the Area Control Error (ACE). After the transient oscillation of the primary control the ACE is zero in a non-disturbed control area and in the disturbed control area the ACE is equal to the sum of the power balance (import positive, export negative). Basically the following equation has to be fulfilled for every control area after the transient oscillation of the primary control:

Zero = deviation of primary control power – deviation of exchange power - disturbance power

In the case of a consumer reconnection the disturbance power is positive; in case of a disconnection it is negative. If now the equation above is transposed it reads as follows:

disturbance power = -ACE = deviation of primary control power – deviation of exchange power

or

$$-ACE = -K_T \cdot \Delta f - \Delta P_{T_A} \; oder \; ACE = K_T \cdot \Delta f + \Delta P_{T_A} \tag{8}$$

The Area Control Error ACE of the secondary control reads as follows:

$$ACE = K_T \cdot \Delta f + \Delta P_{T_A}$$

Here values with index T belong to the part-networks and index A for the exchange power. By the estimation of the deviation of the primary control power and by measuring the deviation of the exchange power the each time appearing disturbance power can be determined. The coefficient K_T given in MW/Hz necessary for this estimation is determined by the measurement of the real network coefficient of the primary control of a part-network Λ_T ,whereas this coefficient is about Λ_G = 20 GW/Hz for the whole ENTSO-E network in non per unit values today. Generally for the total network it reads as follows:

$$\lambda_G = \Lambda_G \cdot \frac{f_N}{P_G} \; and \; \sigma_G = \frac{1}{\lambda_G} \tag{9}$$

The inverse value of the network coefficient λ_G is called the network statics σ_G. The per unit value of network coefficient λ_G is calculated by the per unit values of the network coefficients of the part-networks according to:

$$\lambda_G = \sum_i \lambda_{T_i} \cdot \frac{P_{T_i}}{P_G} \; oder \; \frac{1}{\sigma_G} = \sum_i \frac{1}{\sigma_{T_i}} \cdot \frac{P_{T_i}}{P_G} \tag{10}$$

For the steady-state frequency deviation of the primary control of the total network in Fig. 1 in the case of steady-state considerations the deviation is calculated by:

$$\Delta f = -\sigma_G \cdot \Delta p_{G_V} \tag{11}$$

σ_G describes the statics of the total network including the self-controlling effect of all consumers. Under consideration of this relation the control oriented block diagram shown

in Fig. 6 of a secondary controlled part-network within a total network can be given. In this figure the ACE is the controlled variable, the steady-state primary and secondary controlled part- and total network is the controlled system and the secondary control power of the power plants are the manipulated variables. The controller itself is the integral acting secondary control, which splits into the different control reserve ranges of each contributing power plant of the secondary control according to the coefficients c_i. The operating point "scheduled power" of the power plants is created by the exchange power schedule of the part-network and the hourly load forecasts as well as by the forecasts for the renewable energy generation. The forecasts of the renewable energy generation are commonly differentiated into the day-ahead and intra-day forecasts to minimize the final forecast error as far as possible. The schedules of all power plants are generated according to the demand and supply characteristic which is traded via the European Energy Exchange (EEX) in Germany. This process is described by the tertiary control. The forecasts and forecast errors of the load and the renewable energy generation compose the so called "residual load". The sum of all forecast errors results in the disturbance variable of the controlled system. Therefore it is the job of the secondary control to automatically compensate the disturbance variable. If in the future this disturbance variable will increase due to the increased fraction of renewable energy sources within the system the actively controlling conventional power plants have to be designed for high control reserves and therefore higher ramping rates. This will cause higher stress and thermodynamical wear and it will increase the maintenance costs. Hence the undisturbed part-networks do not contribute to this control because indeed their exchange power P_{TA} and the network frequency will change but with a well conditioned $k_T \approx 1/\sigma_T$ both paths "primary controlled part-network $1/\sigma_T$" and the network coefficient network controller k_T compensate each other and therefore the ACE_T remains zero.

In Fig. 7 the principle of operation of the secondary control with steady-state primary control is shown for a total network that consists of two identical part-networks 1 and 2. In part-network 1 occurs in the left case a step-shaped and in the right case a sine-shaped disturbance of 0.01 pu. In the case of the step-shaped disturbance the frequency deviation amounts to:

$$\Delta f = -\Delta p_{T1_V} \cdot \frac{P_{T1}}{P_G} \cdot \sigma_G = -0.01 \cdot 0.5 \cdot 0.14 = -7 \cdot 10^{-4} pu \; oder \; -35 mHz \tag{12}$$

The ACE_{T1} (blue line) is changed according to the disturbance in the first moment and returns back to zero after the secondary control p_{TS} has reacted and compensated the disturbance. Whereas the signal ACE_{T2} (red line) remains zero during this process. In the first moment part-network 2 supports the compensation of the disturbance by the use of the frequency deviation and the primary control by delivering an exchange power of 5×10^{-3} pu to the part-network 1 (red line). Therefore part-network 1 receives this power of -5×10^{-3} pu shown by the blue line.

The sine-shaped excitation is used to illustrate the influence of the forecast error of the renewable energy production and the consumers onto the secondary control: A permanent frequency deviation occurs and the part-network 1 is continuously delivering secondary control reserves by its power plants (blue line) which will lead to increased wear in these plants. Besides the undisturbed part-network 2 continuously delivers an oscillating amount of power by the use of the primary control (red line). So the power plants of these

undisturbed control areas are stressed and wear at a higher extent, too. This effect is even higher as much more the acceleration time constant is reduced.

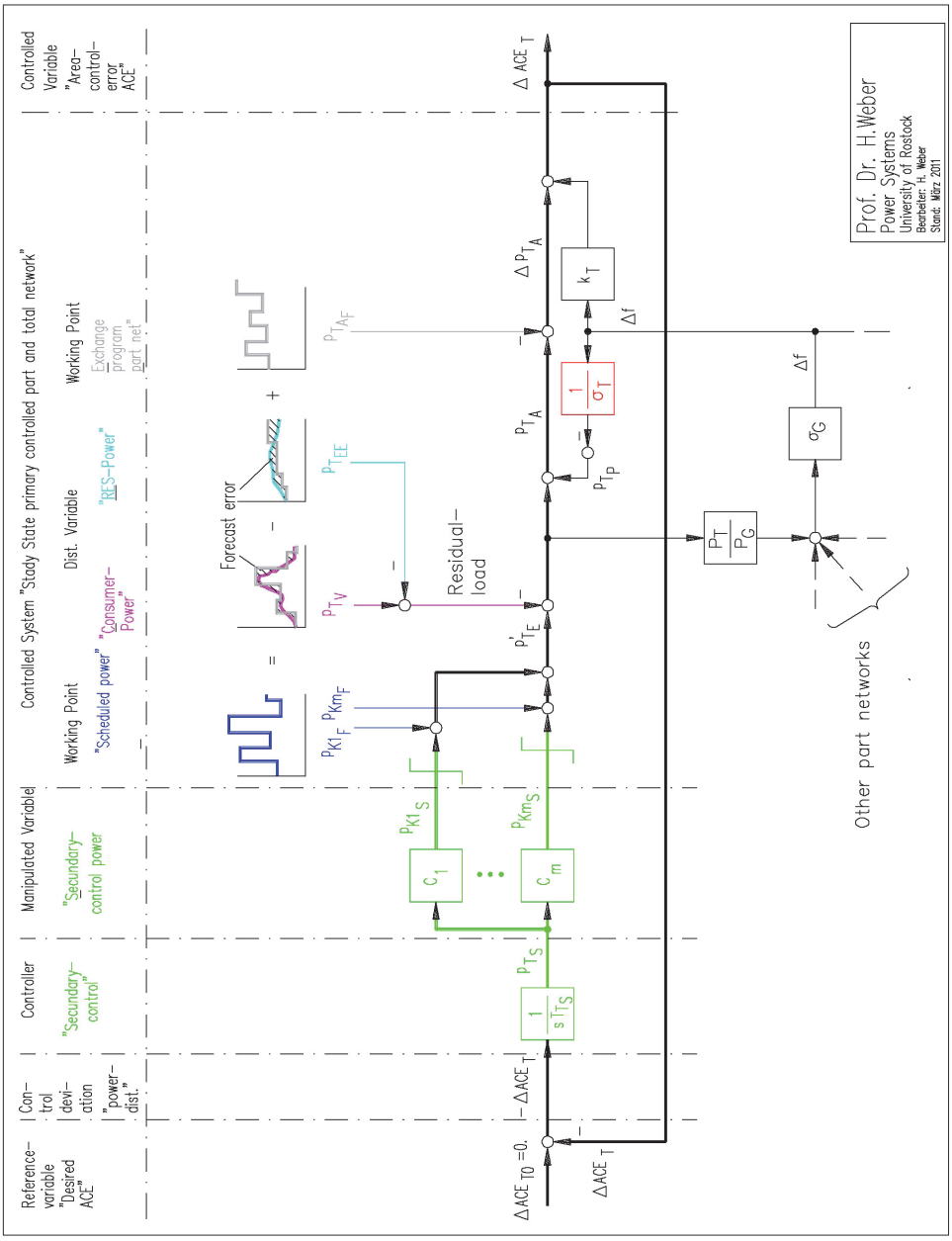

Fig. 6. Control oriented scheme of the secondary control

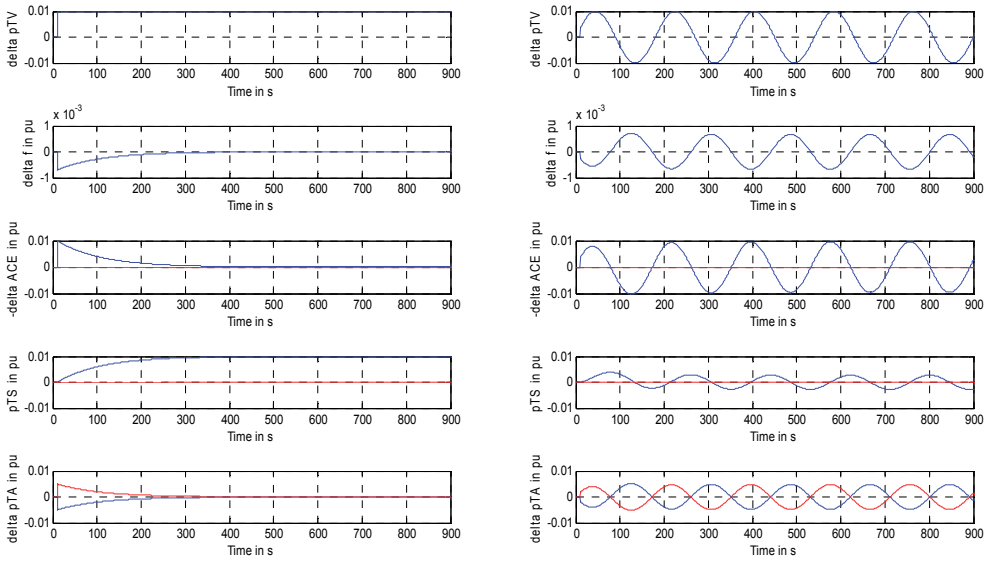

Fig. 7. Principle of operation of the secondary control if a step-shaped (left) and a sine-shaped (right) disturbance occurs

3.3 The tertiary control

The primary task of the tertiary control is the allocation of power into the power plant schedules of a part-network according to the forecasts for the load, for the renewable energy generation and the exchange schedules with other part-networks. In this context it is not a kind of automatic control like the secondary control because these schedules are generated on the basis of stock exchange contracts at the EEX. The control oriented structure of the tertiary control is shown in Fig. 8.

The main task of the players that trade the electrical energy at the EEX is to minimize the costs of generation and to maximize the profit. Therefore it is attempted to minimize the losses and at the same time ensure the safety of supply. This means amongst other issues that the secondary control signal returns back to zero at the end of each quarter-hour. Furthermore the forecasts for the load and the renewable energy generation have to be refreshed continuously and the exchange schedule with other part-networks must be ensured. Therefore the inadvertent exchange power of every week has to be included into the next-week delivery in such a way that all MWh are compensated. Here the controlled system is the "primary and secondary controlled part-network" which is disturbed by the load curves and the real renewable energy generation. The manipulated variables are the schedules of each conventional power plant which can be adjusted with a quarter-hour resolution. In addition to these adjustments of the scheduled power output even warm and cold start-up cycles of conventional power plants can occur to follow the intermittent renewable power feed-in in a complementary way.

This kind of dynamical operation will increase in the future if more and more uncontrolled renewable power feed-in is added to the system. Therefore the effect of this higher dynamic and more pretentious flexibility requirements are discussed in the next sections.

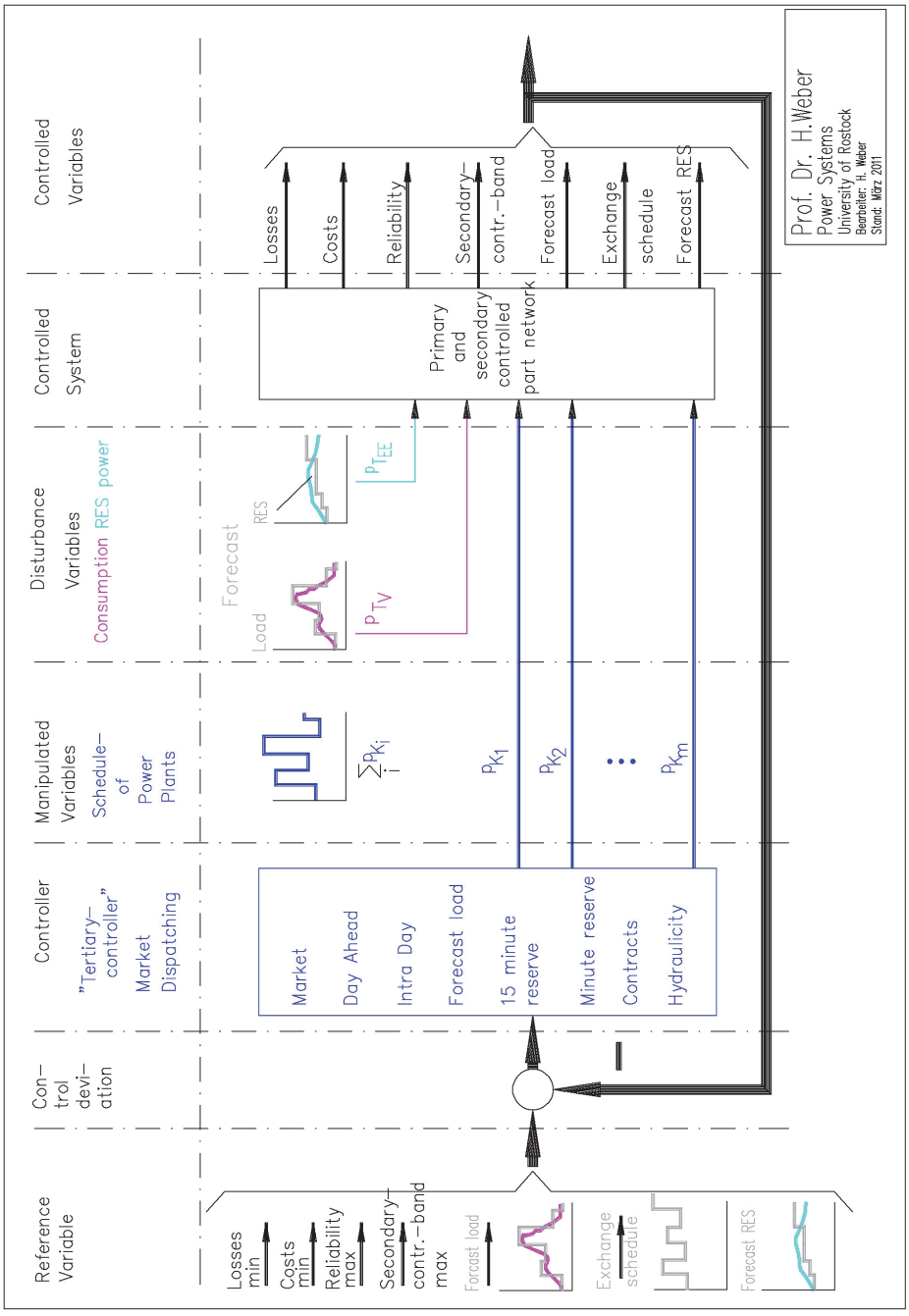

Fig. 8. Control oriented scheme of the tertiary control

4. Power plant scheduling and technical limitations of conventional power plants

To analyze the intermitting power sources and to simulate the influence onto the conventional Thermal Power Plants (TPP) several simulation models are necessary. The network control was described in detail in the previous sections. In this section particularly the power plant scheduling model will be described with some more details. To have a more precisely formulation of the associated equations please take look at the references mentioned in the text.

The so called unit commitment models can be used to simulate the power plant scheduling, e.g. the tertiary control, to take care of general technical parameters of thermal power plants like minimum up- and downtimes, minimum power output and ramping rates, reserve capacities and time dependant start-up costs. Today often these models have a Mixed-Integer Linear Programmed (MILP) optimization structure that uses commercial solver engines like IBM CPLEX to calculate the schedules of the fossil and nuclear power plants using variable time resolutions usually set to a one or a quarter-hour. In these models the spinning reserves for primary and secondary control and the non-spinning reserves for the tertiary control have to be considered. Fig. 10 gives an overview of the different types of power reserves.

To give an example for such a scheduling process for an existing thermal generation system the power plant parameters for the following scenarios were set to realistic values that hold for most of the German power plants. These values were determined with the help of the five biggest power plant operators in Germany and Dong Energy from Denmark as well as the combined cycle power plant (CCPP) operator "Kraftwerke Mainz-Wiesbaden (KWM)" in Mainz (Germany) within the research project "Power plant operation during wind power generation" – the "VGB Powertech" research project No. 333. The "VGB Powertech" is the holding organization for more than 460 companies from the power plant industry in 33 countries especially in Europe.

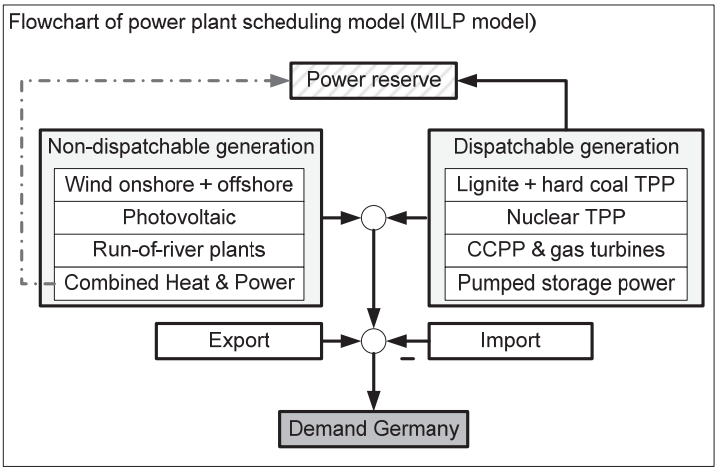

Fig. 9. Overview of the different types of generation sources for the scheduling simulations shown in this section

For the following scenarios the simulations include estimation models for the wind and photovoltaic time series as well as time series to take care of the Combined Heat and Power (CHP) stations whose electrical output power normally depends on the outside temperature and therefore the heat demand and which will have heavy influence onto the remaining must-run power and inertia as well as the resulting residual load that has to be covered by dispatchable power stations.
Therefore Fig. 9 gives a general overview of the different types of power plants and energy sources within the simulations. In this diagram two main boundary conditions must be observed at any time. The first is the active power balance stated in equation (13) between dispatchable generation and the residual load, the second one is the observation of the availability for the different types of reserve power as stated in equation (14).

Constants

$R^{rt}(t)$	Total reserve of type rt in period t
$RL(t)$	Residual load demand in period t

Sets

U	Set of indexes of the generating units
T	Set of indexes of the time periods
RT	Set of indexes of the different reserve types

Variables

$c_u^{fu}(t)$	Production cost of unit u in period t
$c_u^{su}(t)$	Start-up cost of unit u in period t
$c_u^{sd}(t)$	Shut-down cost of unit u in period t
$p_u(t)$	Power output of unit u in period t

$$\sum_{u \in U} p_u(t) = RL(t), \quad \forall t \in T \tag{13}$$

$$\sum_{u \in U} p_u^{rt}(t) = R^{rt}(t), \quad \forall t \in T, \forall rt \in RT \tag{14}$$

Due to the huge number of flexible units in such models, here more than 150 units, and a time horizon of one or more days with a an hourly resolution (here 36 hours), the number of overall binary variables can be reduced by using an efficient formulation of the different boundary conditions as stated in Carrión *et al.* (2006) under consideration of equations from Arroyo *et al.*, (2000). A detailed description of all equations used for the simulations shown here can be found in these two references to describe all aforementioned technical constraints of the conventional power plants. The equations were slightly adjusted to the assumption described in this section but the basic structure was not changed at all.
For similar approaches where MILP structures are used to solve the unit commitment problem even under consideration of security constraints and simplified transmission line capacities see Streiffert *et al.* (2005), Delarue *et al.* (2007) and Frangioni *et al.* (2009).

4.1 Consideration of the different types of reserve power

As mentioned before the reserve power is considered as well within the scheduling process. Therefore there are different classes and types of reserves for different purposes with different response times.

The reserves can be divided into two classes – the spinning and the non-spinning reserves as shown in Fig. 10. Spinning reserves are available in the aforementioned inertia of the rotors of the directly synchronized generators. The reserve provided by the accelerating power of the directly synchronized inertia responds immediately to any active power disturbances.
The second class of reserves – the non-spinning reserve – is provided by generators that can be online or offline but ready to start up within 15 minutes. Usually this tertiary or so called minute reserve is provided by gas turbines or Combined Cycle Power Plants (CCPP).
These different types of reserves are necessary to guaranty the stable operation of the generation system and to respond to outages of generation units or changes in the power demand.

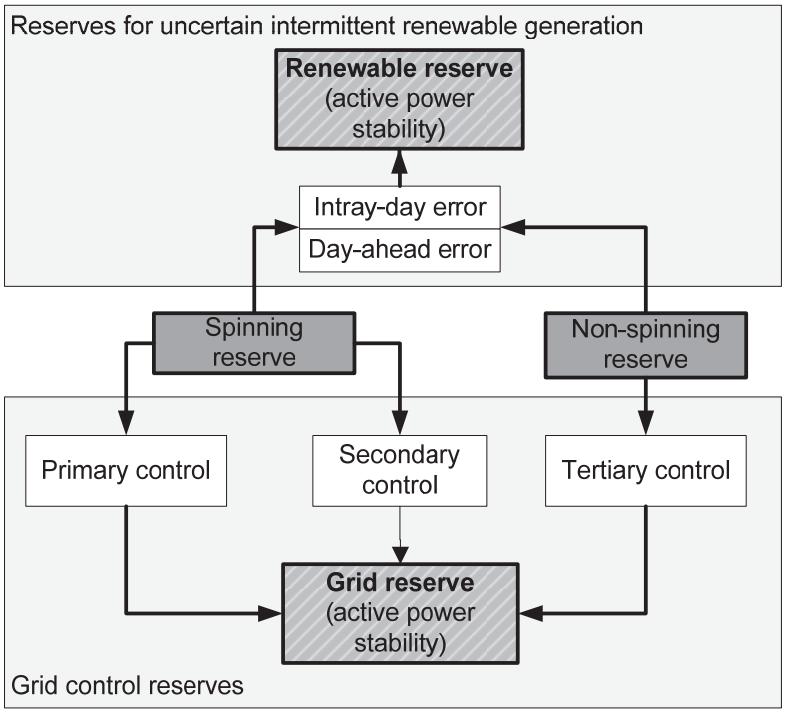

Fig. 10. Classes and types of different power reserves

Unfortunately due to the intermittent character of solar and wind power these energy sources are uncertain and so they are forecasted depending on meteorological measurements and forecasting models. These models always have forecast errors but they were enhanced intensively within the last years. These forecast errors can be divided into two types, the day-ahead or long-term errors and the intra-day or short-term errors. Normally the intra-day errors are noticeable smaller than the day-ahead errors because the forecast horizon is much smaller. The average forecast errors are usually characterized by the root-mean-squared-error (RMSE), which was between 3.7 and 5.8 % in 2010 for day-ahead and about 2.7 % for average intra-day forecasts in Germany according to information of the German Transmission System Operators (TSOs).

4.2 Objective function for the tertiary control optimization process

As shown in Fig. 9 the power plants are divided into dispatchable and non-dispatchable generation. Normally only the power plants that belong to the dispatchable generation are able to fulfil the network control requirements. This means their operation point as well as the amount of primary and secondary control reserves are optimized by an optimization process so that the total operational costs are minimized as stated in equation (15). These operational variable costs split into fuel costs on the one hand and start-up and shut-down costs on the other hand.

$$Minimize \sum_{t \in T} \sum_{u \in U} c_u^{fu}(t) + c_u^{su}(t) + c_u^{sd}(t) \tag{15}$$

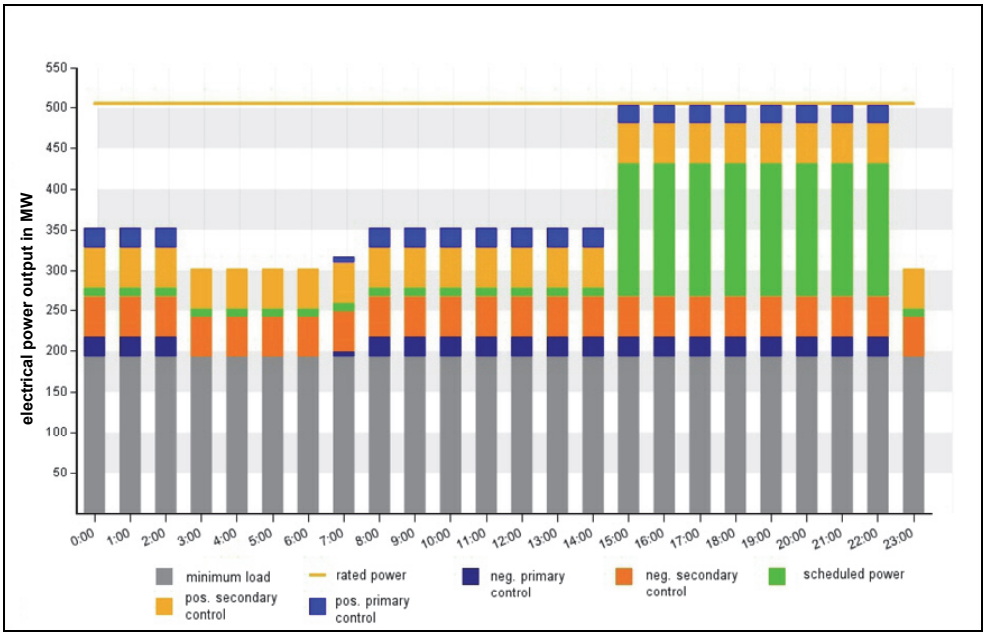

Fig. 11. Simulated schedule with reserved control areas for primary and secondary control for a single power plant

This kind of optimization problem is commonly known as the unit commitment problem. For simplification the fuel costs often are modelled by a step-wise linear production cost curve for partial loads of conventional power plants. For the scenarios shown here the partial production cost curve is divided into maximal three segments. The detailed equations used and adjusted for modelling such step-wise functions as well as equations for start-up and shut-down costs and ramping rates are stated in Carrión *et al.* (2006), but in addition to the reserve stated there, the scenarios here consider a detailed allocation of the different types of spinning and non-spinning power reserves, too. This means that the amount of reserve power for primary and secondary control as well as a dynamical reserve for forecast errors is determined for each station that is online. By considering these

spinning reserves in each station, the resulting must-run power that can't be undercut is determined by the optimization process.
Fig. 11 shows the result of such an optimization for a certain single power plant. Here the area with the reserved power for the primary and secondary control is illustrated for each hour. In this diagram the scheduled power output of the plant for each hour is the power value which belongs to the top of the green area. Therefore only the range of the green area can be used to correct the schedule in the negative direction without a change of the online state of the plant. In the positive direction the maximum possible correction is limited by the rated power output of the plant.

4.3 Exemplary scenarios for 2020 of the power plant scheduling process

To simulate a future power plant scheduling scenario it is necessary to generate some reasonable input time series for the different types of non-dispatchable generation. Therefore Fig. 12 shows an exemplary behavior of this non-dispatchable generation. Such time series are used in the following scenarios for different seasons of the year.

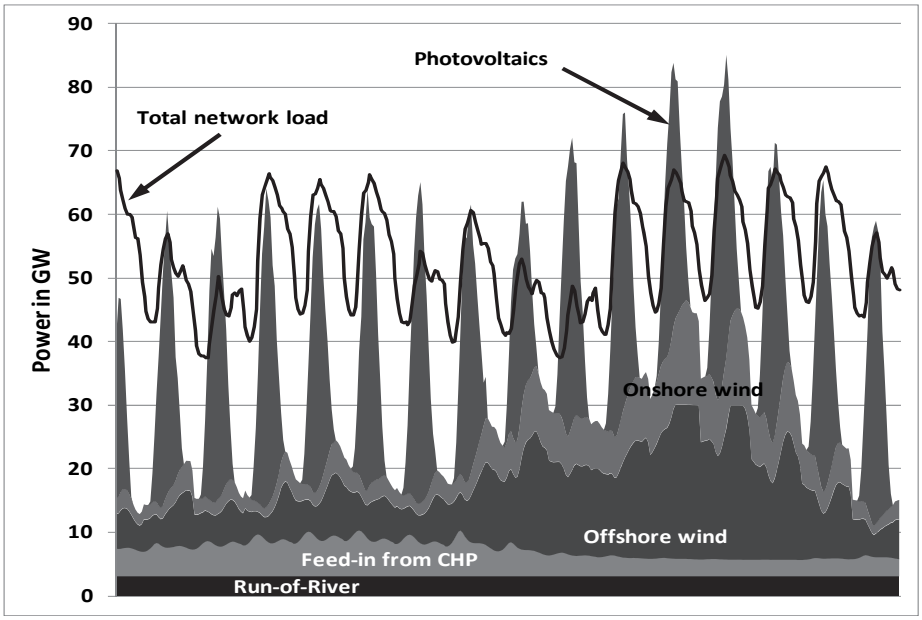

Fig. 12. Non-dispatchable power feed-in for a two weeks summer period in 2025

Fig. 13 and Fig. 14 show the accumulated results of the power plant scheduling for two different scenarios. The first scenario is a typical winter scenario showing the situation in Germany today. In Fig. 13 the typical types of operation modes for base, medium and peak load are clearly visible. Herein the nuclear and lignite power plants are almost operated as base load. The hard coal power plants provide the medium load and the gas and pumped storage capacities (PSPS) support the peak load. In this scenario no offshore wind capacities were defined. Due to the high district heating demand in a winter period the CHP-fraction in this scenario is relatively high.

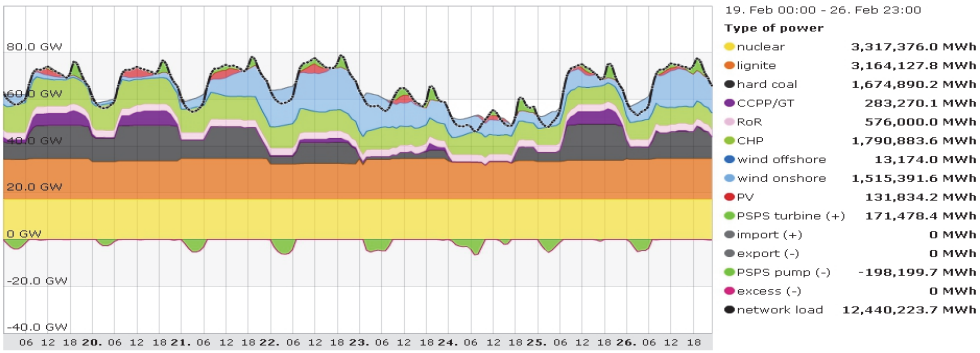

Fig. 13. 7 days period – winter scenario 2010 without import/export capability

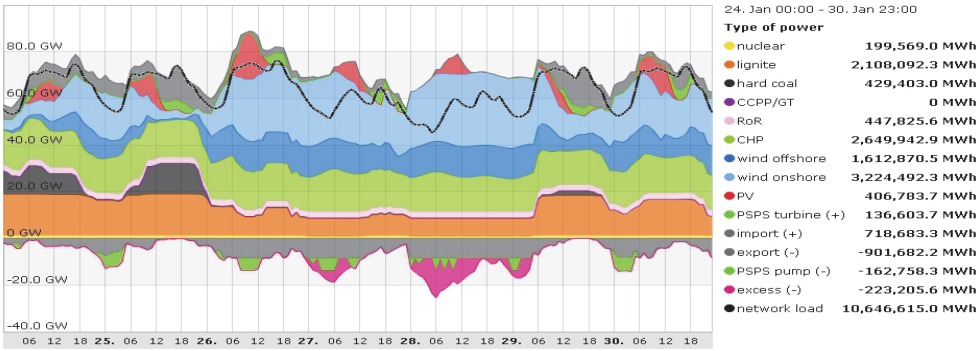

Fig. 14. 7 days period – winter scenario 2020 with import/export capability

In the second scenario, shown in Fig. 14, a 7 day period illustrates a typical high wind at load low load scenario for a winter weekend as expected for 2020. In this scenario the lignite power plants are operated on a very low partial load during the weekend. They ramp up to their nominal output at the end of Sunday (the 5th day) because the wind power feed-in decreases massively at the end of this weekend. At this time several power plants have to start-up as well.

The fraction of nuclear power was reduced due to the high probability of a nuclear phase-out in Germany. The CHP-fraction in this scenario is relatively high because of the high demand for district heating in the winter period.

Due to the limited storage capabilities of the pumped storage power plants and the limited power transmission line capacities to the German neighbour countries it could be possible that a certain amount of renewable energy could not be integrated into the system with today's storage capacities. This amount of energy respectively the excess power is identified

by the model as power surplus shown in Fig. 14. In reality today there are about 10 GW of transmission line capacities, but how much of these capacities will be available in such a high renewable feed-in scenario depends on the renewable power feed-in in the other countries. This problem has still to be investigated in furthermore studies.
By the use of such power plant schedules in addition to certain disturbance signals to simulate the non-predictable deviations of the forecasts for the consumer and the renewable energy generation it is possible to determine the life time consumption of different highly stressed components of single power plants. Therefore a detailed model of each power plant is necessary to simulate the exact thermodynamical behaviour. The methods for such investigations are discussed in the next sections.

5. Life time consumption and life time improvements of conventional fossil power plants

In a future power grid with high renewable power feed-in, especially from wind power, it becomes more important as well as economically beneficial for conventional power plants to be able to adjust the production in order to balance the renewable energies. But due to the long life time, the majority of current power plants have been designed decades ago mainly for steady state operation. Consequently, the focus was put more on reliability and preservative operation than on high dynamics.
The recent and ongoing changes in the energy market in Germany will lead to an increased number of start-ups and load changes, which cause additional life time consumption. Improvements of the existing technologies are required to enable higher dynamics at limited additional stress during transient operation.
This is especially true for coal fired power plants because of the fuel pulverization in coal mills. These mills have a slow and often unknown dynamic and limit the ramping rates of coal fired units. Additionally, the boiler itself shows a slow transient response due to its big metal and water masses as well as uncertainties like degradation of the heat transfer due to ash build up on the heating surfaces. To overcome this, the ramping rates are made sufficiently slow.
Improvements to this conservative approach could be achieved by the use of advanced control systems, e.g. state observers and model based control systems or additional sensors, like for example coal dust measurement (Dahl-Soerensen, M.J./Solberg, B., 2009).
For the evaluation of such optimizations of the process and the control system, computer aided simulation of the power plant process could be a powerful tool.

5.1 Methods for simulation

In order to judge the expected impacts of a more dynamic power plant operation a detailed, transient model consisting of one-dimensional or lumped interlinked sub models, based on thermodynamic fundamental equations, has been created. A 550 MW hard coal power plant, that started its operation in 1994, has been used as a reference. This power plant represents the state of the art and is due to its long rest life time heavily effected by future changes of the energy market.
The focus of the investigation has been put on the water-/steam circuit, the combustion chamber of the steam generator and the fresh air passage with the coal mills, as well as their

dynamics and the influence of different operation modes on distinct devices e.g. thick-walled headers and turbine shafts.
A simplified schematic of the model is shown in Fig. 15. Indicated are the feed water pumps, high pressure preheaters (HPP), the steam generator, the different turbine stages, as well as the forced draft and mill fan, the air preheater and the coal mills. The low pressure preheaters (LPP) are not part of the power plant model, since they are not highly stressed, due to their low temperature level.

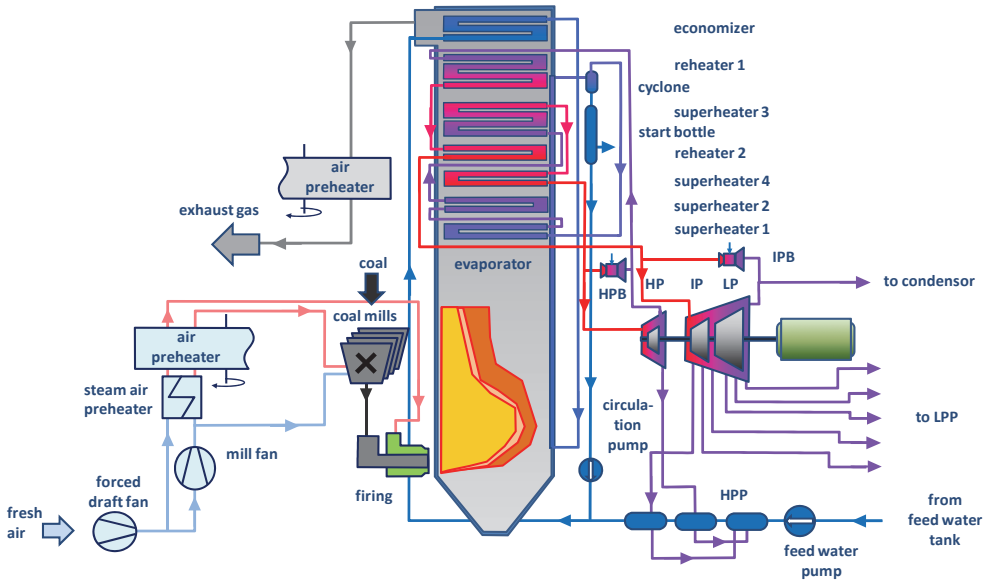

Fig. 15. Structure of the power plant model

For making simulation-based statements about the influence of different power plant operation modes the thermodynamical model is coupled to a reduced copy of the power plant control system.
The modeling is conducted in Modelica (Casella *et al.*, 2003, Casella *et al*, 2005, Fritzson, 2004) using the simulator Dymola®. The modeling with Modelica is characterized by its modular concept.

5.2 Methods for evaluation of life time consumption

With this model it is possible to predict temperatures and temperature gradients at points which are inaccessible to measurements like wall temperatures of highly stressed components.
For the first 90 minutes of a soft start the occurring wall temperatures of the superheater 2 outlet header are displayed in Fig. 16. Obviously the metal temperature at the outside of the wall follows the inner temperature with a certain delay and its amplitudes are considerably

smaller. This effect can be explained with time specifics of the heat conduction. The noticeable phase shift of the temperatures leads to relative high temperature differences between the inner and outer phase in case of sharp edged changes in evaporator heating or cooling.
The evaluation of metal temperatures offers the possibility to benchmark different controller parameter sets with a view to preserving operation at concurrently high load dynamics.
Quantification of the effects of thermal stress on the different components of a plant is a challenging task as the processes of fatigue are complex and highly statistical. For this reason the results of a fatigue prediction in this context can only be of qualitative nature and should be understood as a trend indicator that is capable of identifying the most stressed components and predict possible side effects of innovative control strategies on this complex system. For a detailed investigation of certain components a FEM-analysis considering the installation situation (and with it possible pretensions in the component) and the exact geometry should be taken into account.

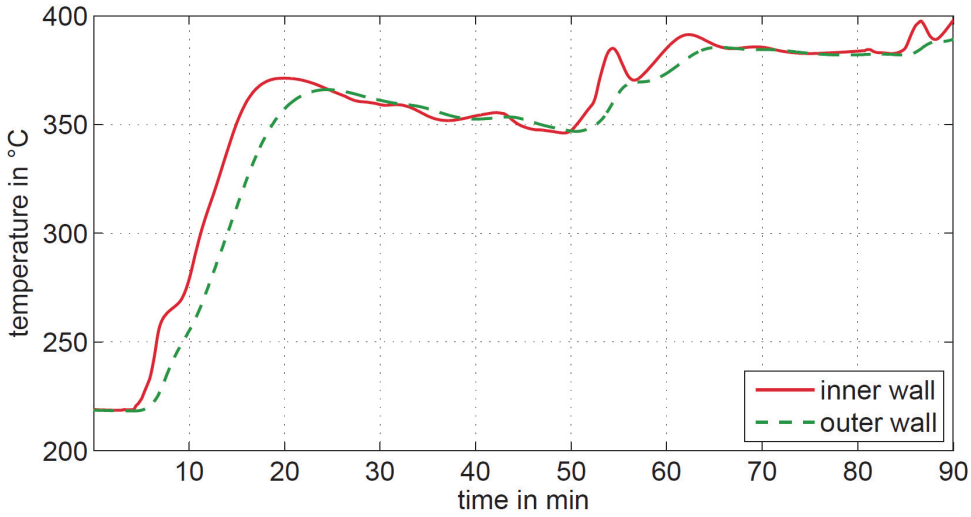

Fig. 16. Metal temperatures in the SH 2 outlet header

However, for a first estimation of the effects of future more dynamic plant operation two different approaches are used and should be discussed in the following:
The guidelines of the *Deutsche Dampfkesselausschuss (2000)* TRD 301 and 508 give directives for the estimation of fatigue of thick-walled boiler components under smoldering pressure and temperature due to start-up processes.
For this purpose an effective stress range is evaluated with a Wöhler-diagram for crack initiation. The following equation gives the law for calculating the stress range $\Delta\sigma$.

$$\Delta\sigma_i = \left(\alpha_m \frac{d_m}{2s_b}\right)\Delta p + \left(\alpha_\vartheta \frac{\beta_{L\vartheta} E_\vartheta}{1-v}\right)\Delta\theta \tag{16}$$

Herein $\alpha_m, \alpha_\vartheta, d_m, \beta_{L\vartheta}, E_\vartheta, \nu, \Delta p$ and $\Delta\theta$ denote for mechanical and thermal correction factors for stress super-elevation at branches, mean diameter, mean wall thickness, linear expansion coefficient, Young's modulus, Poisson's ratio and the range of pressure and temperature difference during load change, respectively. Fig. 17 shows qualitatively the evaluation of the working stress during load change. The maximum number of load changes comparable to the actual one is generated from the Wöhler-curve. The percentile fatigue of the actual load change is then:

$$e = \frac{1}{N}100 \tag{17}$$

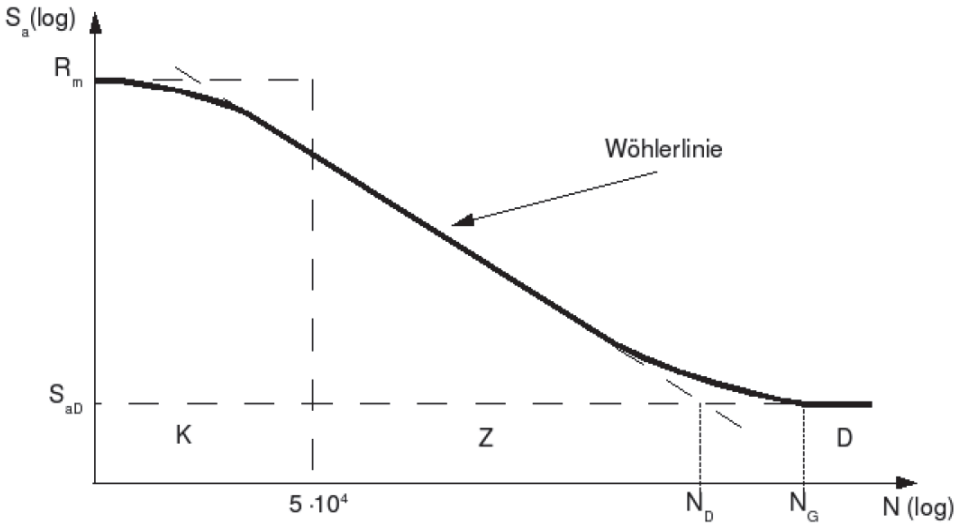

Fig. 17. Principle of evaluation of component stress for cyclic loading (Levin et. al, 1990).

This estimation leads to conservative results in order to handle the numerous uncertainties in calculation of working stresses at complex components and material properties.
This method allows to benchmark different and possible future operation modes in terms of their level of deterioration to different components. In Fig. 18 is the fatigue of a warm start and several load changes plotted for the in- and outlet headers of the super- and reheaters. It should be stated, that currently normal operation is between 50 % and 100 % load with a ramping rate of 2 % per minute, so the shown load change of higher then 60 % as well as the load gradients of 4 % per minute could be considered as an unconventional operation. These load changes corresponds to a possible future operation with a lowered minimum load of for instance 35 % and a doubled load gradient.

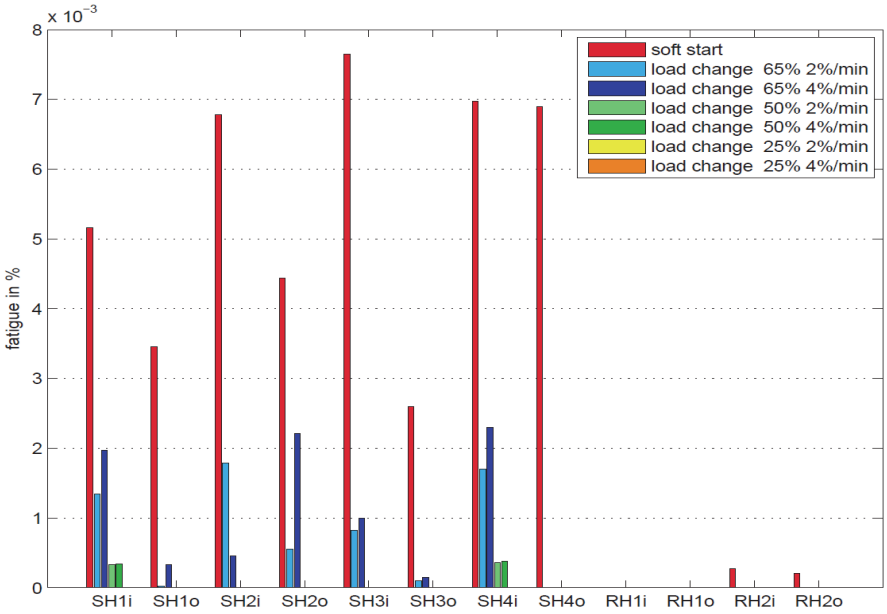

Fig. 18. Fatigue of heating surface in- and outlet headers for different base stress situations

It could be obtained, that the outlet header of super heater three and four are affected the most, whereas the headers of the reheaters are not or low stressed. Furthermore it could be derived, that conventional load changes less the 50 % barely cause any fatigue, because the stress levels are below the endurance strength.

Considering the flaw growth of pre-damaged component gives a far more sensitive view on the operation mode. The *Forschungskuratorium Maschinenbau* (FKM, 2001) gives guidelines for the calculation of crack progress. Fig. 19 gives a general overview on crack propagation rate as function of the range of stress intensity factor ΔK .

There is a certain load that does not lead to crack propagation $(\Delta K \leq \Delta K_{th})$. In region I to III there is a stable propagation to be expected $(\Delta K_{th} \leq \Delta K \leq \Delta K_c)$ which can be conservatively estimated by the law of Paris and Erdogan:

$$\frac{da}{dN} = C\Delta K^m \tag{18}$$

Where a, N, C, m denotes for crack length, number of cycles, a case-specific factor and a load specific exponent, respectively.

The stress intensity factor has to be calculated depending on the flaw's geometry and size and its position within the component. With this tool it is possible to detect the most strained components by comparing the crack growth over a certain reference time period.

In an analogue manner as in Fig. 18 the flaw propagation is shown for thick-walled headers in Fig. 20.

In contrast to the fatigue also low stress levels of small load changes cause impairment and consequently with this estimation a method is given to evaluate the deterioration potential of load changes during normal operation.

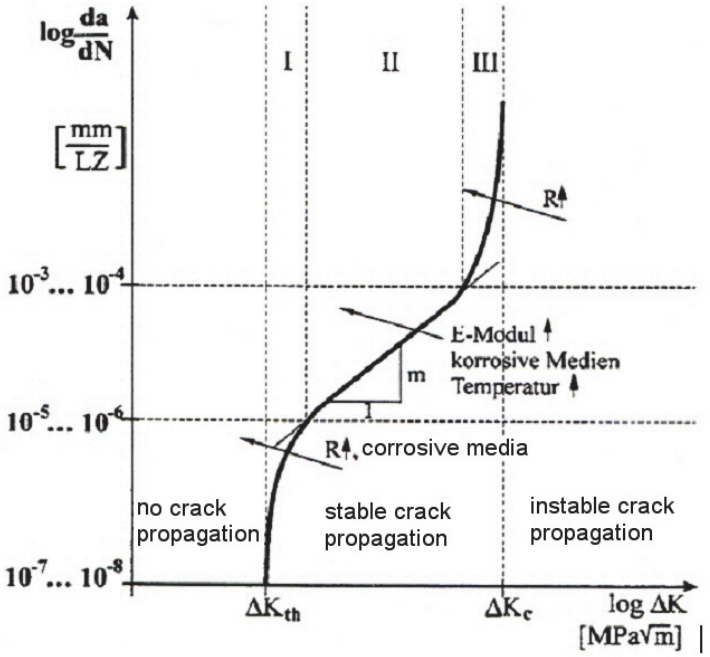

Fig. 19. Overview on crack propagation under cyclic load (FKM, 2001)

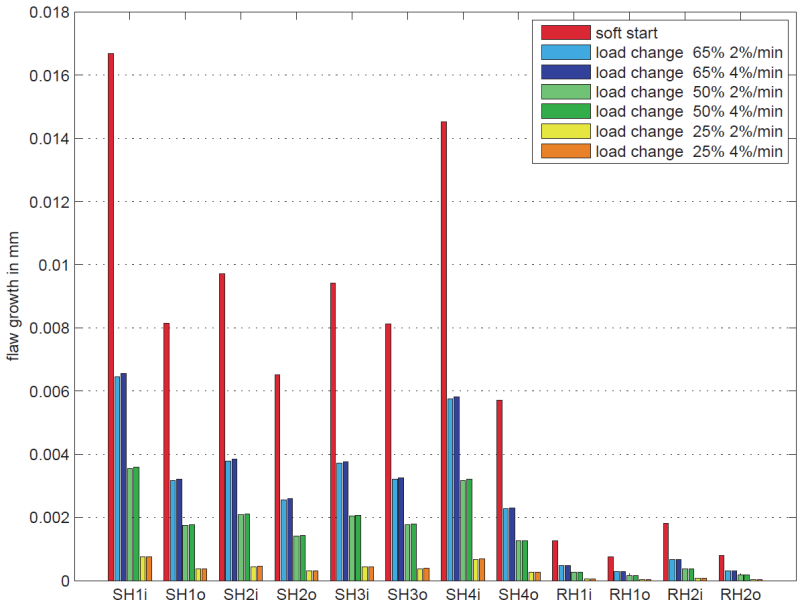

Fig. 20. Flaw growth in potentially pre-damaged thick-walled in- and outlet headers for different base stress situations

In this way, future demands on power plants which might become necessary in order to realize wind integration successfully at controllable costs can be benchmarked. Since the detailed manner of the plant model does not allow long term simulation over years or even weeks due to high computing time, the fatigue has to be extrapolated by decomposing long term load schedules to base operation scenarios and adding the individual fatigues and crack growths under the assumption of linear damage accumulation. In cooperation with the power plant scheduling model it is possible to evaluate such long term load profiles for e.g. a heavy wind month.
This aspect of power plant operation management will probably become more important due to highly increasing wind power production and its fluctuating characteristic.
Furthermore the modular structure of the model allows the easy replacement of single components, e.g. life steam temperature control, which enables for example the benchmark of advanced control systems or the implementation of different or additional hardware for different operation scenarios.

6. Conclusion

In Germany the existing electrical power production and distribution systems are going to be essentially influenced due to the continuously increasing relevance of renewable energy sources.
To analyze these intermittent power sources and to simulate the influence onto thermal power plants, several simulation models can be used. These models can be used to simulate the power plant scheduling that is necessary to consider technical restrictions of thermal power plants like operation states, minimum up- and downtimes, minimum power output, ramping rates, storage capacities etc. Today such models are often formulated as a Mixed-Integer Linear Programmed (MILP) optimization problem, commonly known as the unit commitment problem.
With the calculated schedules for each station within the model, the number of load changes and start-up cycles for the different types of power plants can be determined. These schedules can be rated in terms of mechanical wear due to thermal stress by a thermodynamical model that simulates the life time consumption of the different components used within a hard coal fired power plant with a complex model of the water steam cycle as well as the mill and boiler components. This model of the thermodynamical process is controlled by a detailed simulation of the power plant control system.
The renewable energy generation will be the future solution for the global energy consumption problem. Therefore it is very important to consider all technical restrictions of the network control and the thermal power plants that are necessary to ensure the safety of supply.
To investigate the effects of the increasing fraction of renewable energy produced by intermittent generators like wind turbines and photovoltaic systems within the existing generation system several models with different time domains are necessary as described in this chapter. These models can help to evaluate new concepts for power plants in regard to economical issues and they can help to determine the limitations of a stable system operation in regard to reduced system inertia.

7. References

Arroyo J. M. & Conejo A. J. (2000). *Optimal response of a thermal unit to an electricity spot market,* IEEE Trans. Power Sys., vol. 15, no. 3, pp. 1098–1104.

Carrión, M. & Arroyo, J. M. (2006), *A Computationally Efficient Mixed-Integer Linear Formulation for the Thermal Unit Commitment Problem, IEEE* Trans. Power Syst, vol. 21, no. 3, pp. 1371-1378.

Delarue E.; Bekaert D.; Belmans R. & D'haeseleer W. (2007). *Development of a Comprehensive Electricity Generation Simulation Model Using a Mixed Integer Programming Approach,* World Academy of Science, Engineering and Technology 28 2007.

Frangioni A.; Gentile C. & Lacalandra F. (2009*). Tighter Approximated MILP Formulations for Unit Commitment Problems,* IEEE Trans. on Power Sys., vol. 24, no. 1, pp. 105–113.

Streiffert D.; Philbrick R. & Ott A. (2005). *A Mixed Integer Programming Solution for Market Clearing and Reliability Analysis,* IEEE.

Dahl-Soerensen, M.J. & Solberg, B. (2009). *Pulverized Fuel Control using Biased Flow Measurements*, IFAC Symposium on Power Plants and Power Systems Control, Tampere.

Casella, F. & Leva, A. (2005). *Object-Oriented Modelling and Simulation of Power Plants with Modelica*, proceedings of 44th IEEE Conference on Decision and Control, and the European Control Conference, Sevilla.

Casella,C. & Leva,A. (2003). *Open Library for Power Plant Simulation: Design and Experimental Validation*, proceedings of 3rd. International Modelica Conference, Linköping

Deutscher Dampfkesselausschuss (2000). *Technische Regeln für Dampfkessel (TRD) 301 Berechnung auf Wechselbeanpruchung durch schwellenden Innendruck bzw. durch kombinierte Innendruck- und Temperaturänderungen*. Carl Heymanns Verlag KG

Deutscher Dampfkesselausschuss (2000). *Technische Regeln für Dampfkessel (TRD) 508 Zusätzliche Prüfungen an Bauteilen berechnet mit zeitabhängigen Festigkeitswerten,* Carl Heymanns Verlag KG

Forschungskuratorium Maschinenbau (2001). *Bruchmechanischer Festigkeitsnachweis für Maschinenbauteile*, VDMA-Verlag

Part 4

Wind Farm Analysis

4

The Design and Implement of Wind Fans Remote Monitoring and Fault Predicting System

Yao Wanye and Yin Shi
North China Electric Power University
China

1. Introduction

In modern wind power farms, it is imperative to establish a remote monitor system to monitor the unmanned working process and the fans which working in the bad environment. Under this remote monitoring system, we realized the supervisory information of the wind farms, which similar to the SIS of fuel power plant, including: power forecasting of fans, fault predicting of wind generators and more. This article mainly introduced the OPC system for data collection, the virtual private network (VPN), the real-time data base monitoring and fault predicting. If the wind farms have been established electricity special communication network, we can apply for the special communication network to transfer data of fans and boost station, which will be more safety and steady. On the basis of these, the remote monitoring system has the function of fault predicting in control center. This system has been used in Hebei Construction and Investment New Energy and Datang new Energy.

2. Preface

Along with the global resources and environment worsening, the development and utilization of new energy has gotten more attention. While, comparing with traditional energy sources, wind energy is a clean renewable energy. It is not dependent on fossil energy, no fuel price risk, and no carbon emissions and other environmental costs. In addition, the availability of wind energy is widely distributed around the globe. Because of these unique advantages, wind power has become an important part of sustainable development in many countries. According to statistical report which Global Wind Energy Council (Abbreviation GWEC) edited, global wind power generator installed capacity has reached 158 million kW, the cumulative growth rate has reached 31.9%. To the end of 2009, worldwide there have been more than 100 countries that involved in wind power development, among them, there are 17 countries accumulative total installed capacity over million kilowatts. Large-scale wind power operation will increase uncontrolled power output, which will generates a lot of pressure for electric power dispatching.

In the wind farms, fans are widely distribution with large amount and they are away from the monitoring center, working environment is poor. In order to ensure the safe and stable operation of the wind farms, we need to satisfy the wind power operation requirements, own better function performance and stability of remote monitoring system to improve the

management efficiency. In view of this, the power group increasing highly requirements on wind farm group management, but at present, the single SCADA system which the fan manufacturers offered has failed to meet our requirements. With the investment of new energy, more and more wind farms will be building.

Currently, the wind farm supervisory control and data acquisition (SCADA) system are provided completely by fan manufacturers, the main problems are shown as follows:

1. Compatibility issues:
   There are more than 40 companies engaged in research and development wind generator, and more companies are developing proprietary fans components or complete machine. Large-scale wind farm are generally provided by multiple vendors, the manufacturers of SCADA systems are not compatible, different types of fans lack of effective monitoring and management studies, it is difficult to unified maintenance and management.
2. Information development level:
   At present, the problems of wind power still concentrate in the reliability of wind power generation, power prediction, and Security to the grid, etc. In the SCADA software, the application of information and centralized data collection is still the degree of showing. It is only available to supply operator real-time data and historical data without deeper level of information development, such as condition monitoring, fault diagnosis, operational guidance and so on.
   On the basis, this article designs the wind farm remote monitoring and data analysis system to achieve a variety of fans in different wind farms, and realize wind farm cluster control and data analysis and fault warning.

2.1 The present situation and the solution of the wind farms remote monitoring system

First, because the existing wind farms adopt the monitoring system of the different fans of the manufacturer, the data between the different systems cannot fulfil resource sharing, and can't meet the needs of remote monitoring. Secondly, the wind farm applied to cluster control, which will facilitate different fans operating conditions and the output comparing. Third, the resolving of failure fans began to carry out after the fan malfunction happened, which is not conducive to run economy of wind farms. So we must build a fault early warning ways and improve the operation reliability of the wind farms.

Therefore, we are currently using remote monitoring system for wind farms, which refer to the experience of thermal power project. We have integrated the data that is from different fan manufacturers, and gathered real-time data of run fans and remote communication of booster station. It can realize the remote monitoring, data analysis and processing, provides management with the power plant in the various operating statements, on the basis of this, we also realize equipment fault diagnosis and life management of funs, wind power prediction, and other functions.

2.2 The overall program design of system function

The design of the system can be achieved parallel with the existing fan SCADA system, maintaining data integrity and continuity with kinds of fans running centralized display.

1. The maintenance of the wind resource information

Wind resource generally includes a number of wind farms, usually displayed in the map marked.

2. The maintenance of wind farm information
   Maintain basic information of wind farms, fan information and electric price in tariff in a time period.
3. The maintenance of fans information
   a. Maintain each fan's information, and marked on the map.
   b. Providing for each class, each wind farm of the standard extension for comparison when doing technical analysis.
   c. Each type of fan fault code table.
4. The maintenance of substation information

It include basic information and the wiring diagram of the wind farm, main transformer, circuit breakers, high voltage side arrester, reactive power compensation device, booster station and other equipment.

Remote monitoring system for wind farm should include the following function modules: real-time data collection and monitoring, remote centralized control, performance statistics and analysis, fault early warning, life management, output statistics and forecasts, operation optimization. The functional design should include three levels. First, the underlying data collection and monitoring, namely: using OPC technology to achieve real-time collection for fans and booster station, which save in real time / history stored in the database. By the way, it is shown in web as configuration mode. The second is the upper fault warning analysis, life management function, which including: equipment failure records, fan performance comparison, statistics and fan life management. The third level is a fan of the forecasting and planning, which is on the basis of meteorological data and historical data. This module can get fan's model to predict short-term and even medium-term output forecast for the power grid to provide scheduling support.

The module used to implement specified data collection from existing SCADA systems and substation system. Base on the Web application technology and Browse/Server（B/S）, when data uploaded to data center, users can access via IE overview of wind resources and wind farms, an operation status, substation operation, real-time wind data and other information, real-time operating status of individual fans, all kinds of alarm and fault information. this feature provide wind farm running status of monitoring real-time power and other information for leaders, and they can easily check the production of key information, including core businesses of production management, wind power generation, booster station operation and so on.

The figure of the physical structure of remote monitoring system of wind power is shown in figure 1.

Equip each of the wind farms with a front-end computer to collect the information of the running fans in wind farms and the booster station. The main task of front interface computer is collecting the data of the monitoring systems which are then organized into UDP packets, sent to the data repeater through the firewall, and finally stored in the real-time/historical data server. Develop the function of data cache in front-end computer to ensure that the data is cached when the link is interrupted while it is able to uplink data after the link is unblocked. Install redundant database services on the side of group center to store real-time data and historical data. The 500,000 points real-time\historical database of Tianren Huadian is chosen as the database. For the traditional fan monitoring system, one can enter the fan surveillance server (with a public IP) simply through the VPN client and a

simple password to monitor and control the operations of fans now, which does not meet the requirements of information security and must be improved. Cancel public network IP and all the information exchange with the outside world is to be conducted through a specified isolation unit. Apply optical fibre communication system to the communication link we use and a special 2M special line (E1 lines) used to transmit the information of wind farms is opened for all the wind farms, which in essence ensures the security of information exchange.

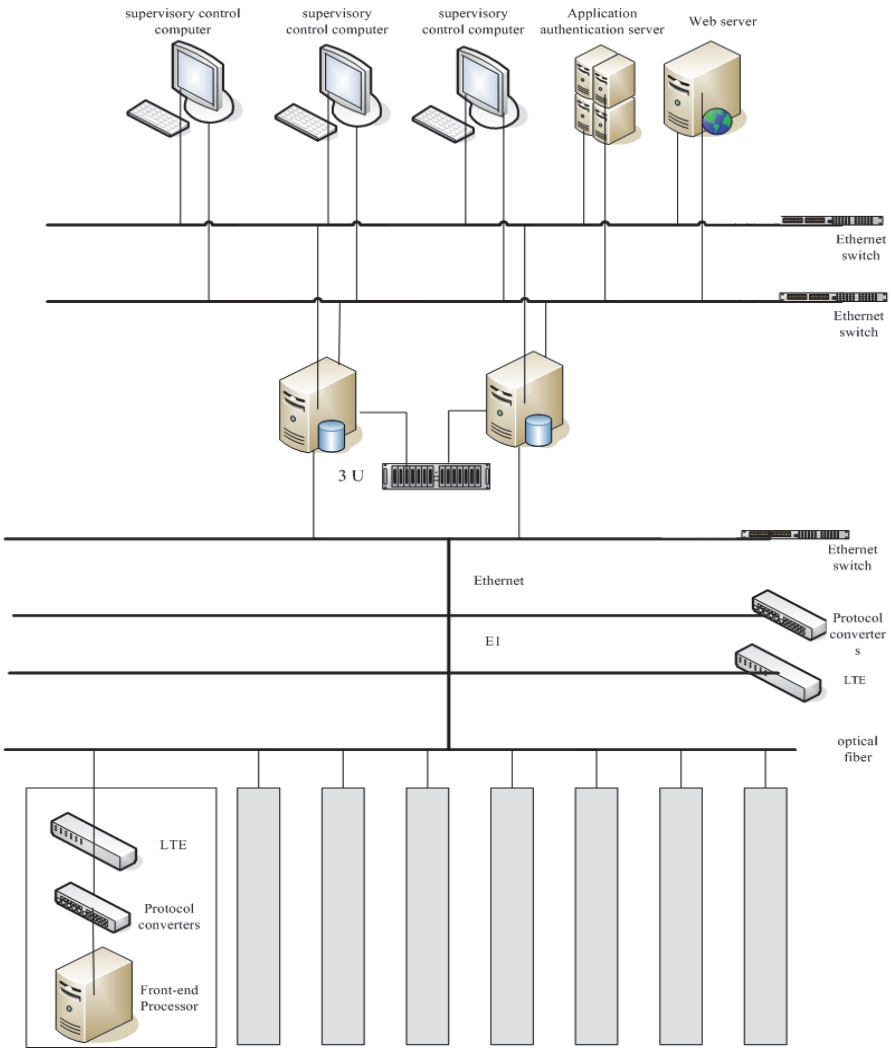

Fig. 1. The physical structure of remote monitoring system of wind power

The data which are lost due to network interruption or other reasons can be amended through manual labour. For areas with no broadband transmission, or no interconnected

network, we can export the data on the plant side, and then sent it to the group through other means to have the data import manually.
The data flow chart of remote monitoring system of wind power is shown as follows:

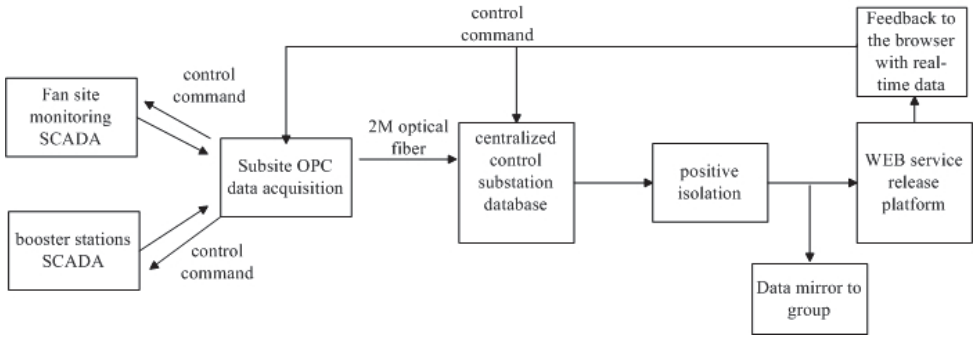

Fig. 2. The data flow chart of remote monitoring system of wind power

3. Design and development of SCADA system software

The software structure of the system is divided into 3 levels. The bottom level is the site monitoring software which can complete the site supervision of respective wind farms independently and is provided by the respective fan manufacturers. The middle level is the redundant real-time / historical database, which covers the storage of the data of fans and booster stations. The top level is software application Level, which completes the programming of plug-in applications and the analysis, processing and prediction of data.
The data level mainly focuses on collecting the operating parameters of wind fields and storing the data in real-time/historical database, with OPC as the collecting method. The application level deals with the applications of real-time database intensively, consisting of business components like business processing service, system authentication service, data connection service, application management system, etc. Those business components can be deployed flexibly in accordance with the actual situation. We can either centralize them on one single computer or choose to deploy them discretely. The chief function of the presentation level, in which the system and users interact, lies in accomplishing man-machine interface works like monitoring, operating, system management, etc.
The system adopts the application system structure in which B/S and C/S combine with each other, which can be configured flexibly according to the actual situation of the scene and user's requirements. It adopts application service based on .NET, fulfils system applications using SVG and XML technology and possesses advantages like easy maintenance, high efficiency, easy to transplant, etc.

3.1 The design and implementation of OPC interface

In a traditional system, application programs like supervisory control and data acquisition system (SCADA), human-machine interface (HMI), configuration software, etc. communicate with field devices through drivers. However, the driver has its own limitations. Different drivers need to be developed if we want to adapt a device to different client applications, resulting in duplication of labour. Once the hardware upgrades, the

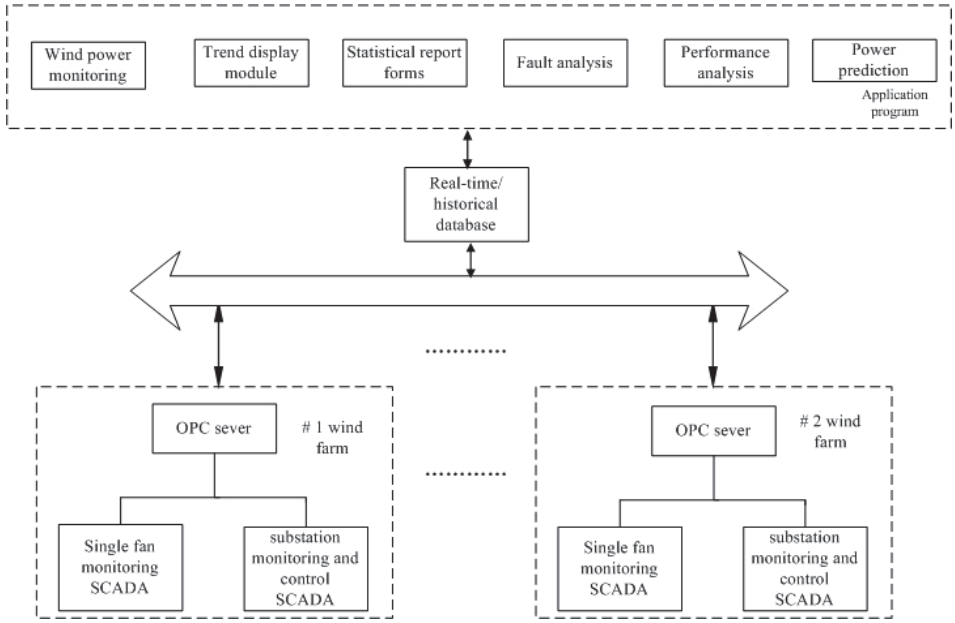

Fig. 3. SCADA software development diagram

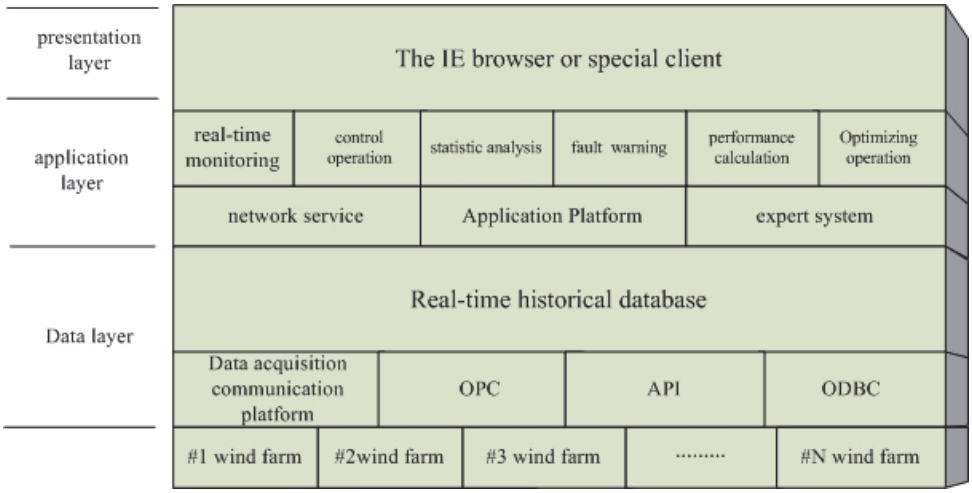

Fig. 4. The design of software structure

previously developed drivers should be modified accordingly. Normally drivers take the form of dynamic link library (DLL), and dynamic data exchange (DDE) is their primary means for data exchange. However, this approach does not allow the visit of multiple applications on one device simultaneously.

OPC (OLE for Process Control) technology comes into being in such a development background. OPC technology is an interoperability standard of industrial control software made by OPC foundation, and also a technology introduced jointly by the control fields and the Microsoft Company aiming at apply Windows to the control system. Based on the component object model / distributed component object model (COM / DCOM) technology of Microsoft, it defines a set of standard interfaces for industrial control software. Through these object interfaces, it realizes the standardization of the data exchange between applications, which greatly enhances the openness and interoperability between automated equipments.

OPC technology demands that hardware manufacturers must provide both equipments and OPC servers with standard communication protocols, while providers of SCADA system software provide client programs in line with the standards of OPC, thus SCADA can connect to OPC servers seamlessly. OPC interface can be applied to the lowest level of applications. That is, through this interface the real-time field data can be gathered and transmitted to DCS or SCADA system. Also by using this interface, we can transfer the data from the DCS system or SCADA system to the application software of upper layer. This contributes to the integration of management and control, and is beneficial to the computerized management of enterprises.

Under OPC, Client visit data in field data server through identical data access method. Though OPC servers may be offered by different software manufactures, an OPC Client can be connected to one or more different types of OPC servers. The structure of OPC applications is as follows:

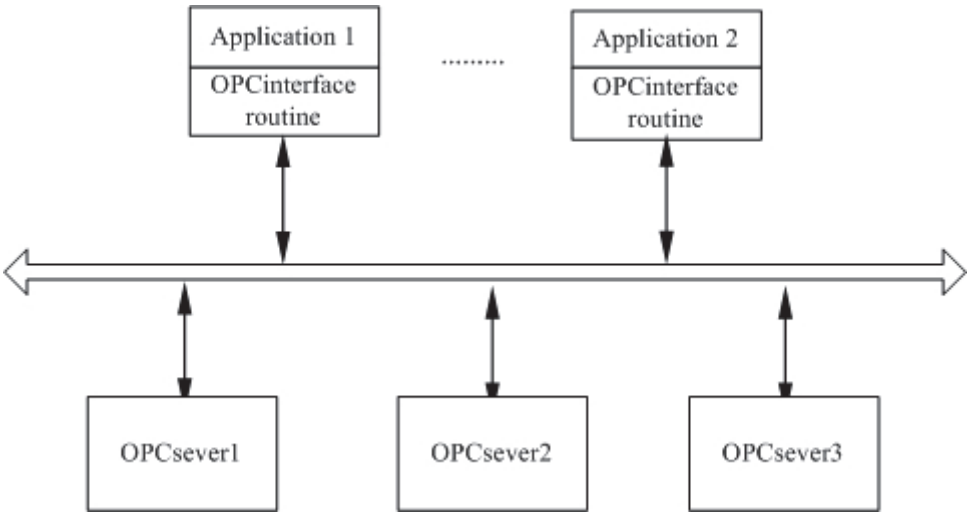

Fig. 5. OPC application program structure

3.2 The design of data acquisition system of front-end computer in wind farms

Since OPC defines a set of interface access methods based on the Microsoft OLE / COM or DCOM, applications which support or meet the OPC agreements can exchange data via OPC protocol if they can visit each other based on TCP / IP. Multiple network adapters

installed on the front interface computer of the wind farm need to be connected to the engineer station of the monitoring systems provided by fan manufacturers. As for its IP address, it should be in the same network segment with the engineers. The system structure is as follows:

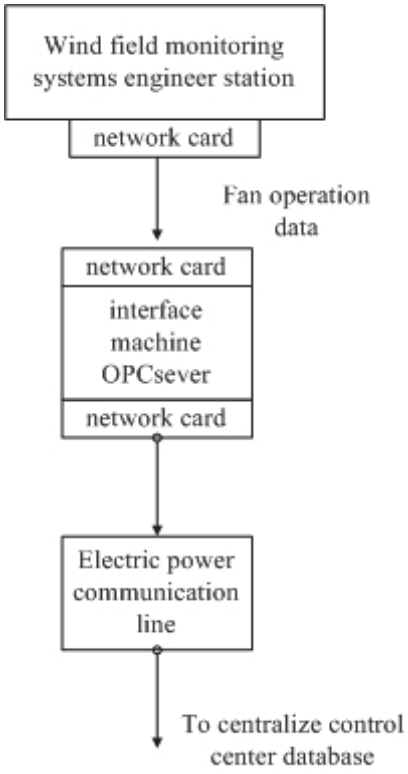

Fig. 6. OPC application program structure

3.3 The design of wind farm centralized control center

Install two database servers in Centralized Control Station for the storage of redundant wind field data, and they share memory way to increase system stability. Connect the network to the office network of New Energy Group as the subnet of the production system for the convenience of releasing information on the whole group web. Access permissions and strategies of the production subnet can be set in the planning of Group network.

Control station database pass to the Group side database system in way of the mirror function. The database server on Group side is deployed in the new energy group. Due to its high expansibility, system adopts SAN, which consists of two fibre switches, for storing. With the expansion of system capacity, the number of disk array and database servers can be increased randomly to achieve the expansion of storage capacity.

We install positive isolation device between the redundant database of centralized control center and Web server for the purpose of isolating fan control systems, substation control

system and real-time historical database system. It only allows the control system interface device to send data to the database system, which achieves unidirectional transmission of information and therefore ensures the security of production control system. The structure of centralized control station is shown as follows:

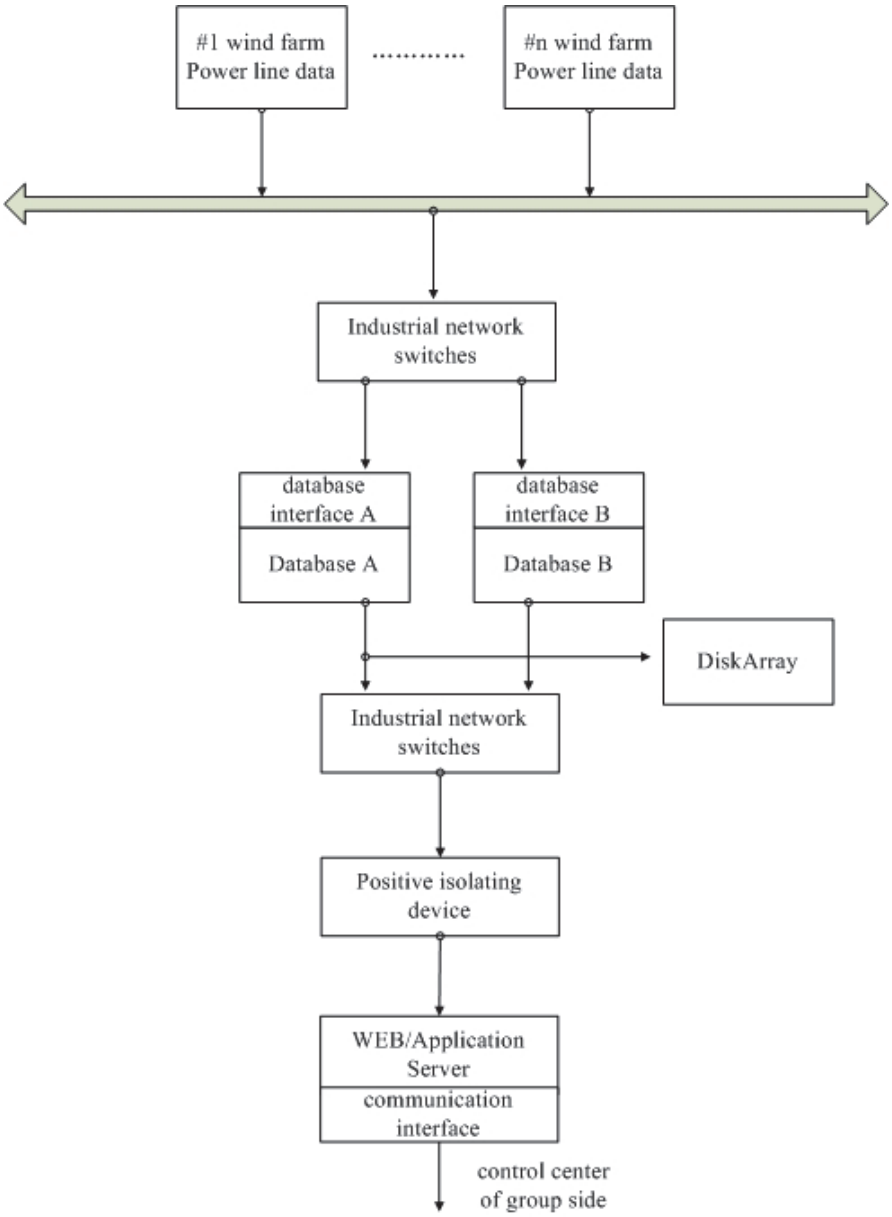

Fig. 7. OPC application program structure

The fan running data of multiple wind farms are uploaded to the redundant database of wind farm centralized control station side though the 2M communication line of their respective wind farms. The data in database is compressed and stored in extensible disk array. Positive isolation device is to ensure the unidirectional transmission of data from the wind side to the group side. Safe isolation network gateway (GAP) is needed. Users can get relevant information only after the digital identity certification. Security isolation gateway, consisting of software and hardware, is a network security device in which specialized hardware with multiple control functions cuts off the link layer connection between networks in the circuit and is able to carry out safe and moderate application data exchange between networks. The hardware device consists of three parts: external processing unit, internal processing unit, isolation hardware. When the user needs to ensure his network of high security while exchanging information with other networks which it distrusts, GAP is essential. Under that situation, using physical isolation card won't satisfy the demand of information exchange; using a firewall won't prevent the leakage of internal information, external viruses and the infiltration of hacker programs, therefore security can not be guaranteed. Security isolation network gateway, however, is the best choice for this circumstance since it can meet those two requirements at the same time and avoid the inadequacies of physical isolation card and firewall. The function of Web / Application Server is releasing data on the intranet of the company, thus any computer connected to the company intranet can share the data

4. Real-time/historical database

Data of Wind farms is the foundation of data analysis, data mining, control optimization and management optimization. There have to be thousands or even hundreds of thousands of data collecting units in one centralized control center which governs several wind farms. Due to the need for site monitoring and real-time analysis, the collected data is subjected to real-time changes. Such large-scale mass data is so difficult to be preserved for a long term in its prototype that the traditional relational database system is unable to accomplish this task at all. Therefore, real-time database comes into being.

Real-time database is the combination of real-time data and database, the key point in the development of which is the compression and storage of mass data. In addition, problems like real-time data model establishment, transaction scheduling methods, resources allocation strategies, real-time data communication, etc. also need to be solved in real-time historical database.

As for database system software, we should choose the large real-time historical database-VeStore widely used in power industry, the authorization point of which is 500,000 points. Database supports standard B/S (browser/server) structure, which can ensure all the real-time production process information of the electric field and calculation through effective compression methods. The recovery time of compressed data should not be more than 15 milliseconds and it should possess good expansibility and openness.

Real-time database should not only serve as the source of data needed in all the computing analysis programs, surveillance pictures, statistical forms and remote control and support standard linking approaches like application programming interface (API) and ODBC2.0, etc, but also provide the management information system (MIS) with required real-time data, calculation and analysis result. Its server and client hardware should be standard products from the third party, and the software module should fully support and be

compatible with the Microsoft system structure and have good transparency and secondary development ability. VeStore real-time database should have backstage calculation engine, a tool that can convert raw data into powerful information. All kinds of complicated second operation can be done through using configuration.
The real-time database should have perfect data mirror function, through which it can mirror the data center of the subsidiary to that of the group company.

5. Real-time/historical database

By processing real-time/historical data, Report capabilities should generate automatically daily reports, monthly reports, availability, power generation losses, etc. which shall be used to assess the running effects of fans from suppliers. Tabular forms should be offered to all kinds of users acting as a basis for management and decisions.
Reports completed by the system are mainly real-time reports, including:
I. Real-time load reports: generate real-time load reports which display information on units, the installed capacity of Wind Farms, load and load rate through classification approaches such as branches, unit capacity, etc.
The average availability in any given cycle of each wind turbine of a wind farm should be calculated as follows:
Availability = TA / TCT * 100%
TA is the available time of a fan, namely the cumulated hours that fans operate or the time that fans possess operating conditions in any given cycle calculated by fan controller
TCT refers to all the calendar time calculated by hours within the computing cycles, for example, the TCT of the availability counted on an annual basis equals 8760 hours.
II. Reports on the start-stop condition of units:
Real-time unit start-stop report—employ flexible inquiry mode and display the present start-stop state of units according to query conditions like unit capacity, wind farm, etc.
Historical start-stop inquiry report—give a record of the start-stop conditions of units in wind farms, its history query time period can be selected arbitrarily.
III. trend analysis reports:
All the parameters can be displayed in multi-forms like trend chart, bar chart, related parameters groups, etc., displaying parameters value in real time and the maximum value, minimum value and average value in defined time period.
IV. unit real-time comparative reports:
The inquiry approaches designed in the system is flexible; it is inquired according to unit capacity and wind farms. You can choose any units or parameters that need to be compared from the units connected to the system to form real-time report of the comparison between parameters.
Reports involved in this system:
1. Start-stop records of fans;
2. The monthly availability of fans in wind farms;
3. The availability chart of several units in different wind farms;
4. The loss analysis table of fan failure;
5. The loss analysis diagram of fan failure;
6. The fault frequency and time contrast of each wind farm;
7. The failure frequency of various types of fan and the comparison chart of power loss;
8. The time proportion of all the running states within given time in wind farms;

9. Comparison of fan power curve;
10. Generating capacity of wind farms;
11. The comparison chart of on-grid energy and repurchase power;
12. Monthly charts of Power generating capacity and on-grid energy;
13. The generating capacity and on-grid energy comparison chart shown in Year / month;
14. The monthly contrasting chart of expected generating capacity and the actual generating capacity;
15. The wind speed- wind rose;
16. Wind energy - wind direction and the actual power generation contrast rose;
17. The trend diagram of monitored data and time (historical changes in blade angle, power, wind speed and blade angle);
18. Wind speed and wind wheel rotate speed curve, the wind farm operating comprehensive daily report;
19. Failure frequency reports of all types of fans;
20. Failure frequency reports of all types of fans and power loss;
21. Unit failure frequency reports and the time report;
22. Generating capacity of all the farms, utilization rate reports;
23. The cost report of the field operation and maintenance;
24. The main interface of wind farm operation and the integrated information of wind farms;
25. The display of instantaneous information of single wind turbine;
26. The caption of fan in different states;
27. The real-time curve of the instantaneous wind speed in wind farms;
28. The historical data Display of wind farms, etc.

The comparison of average wind speed this month and last month in wind farms monitored by centralized control station are shown in Figure 8:

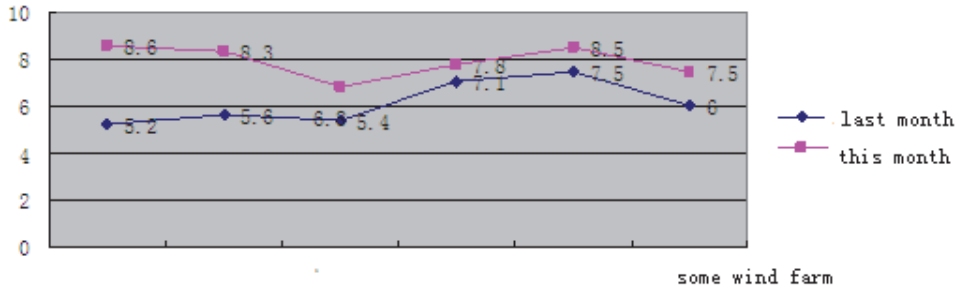

Fig. 8. The comparison chart of average wind speed this month and last month in some wind farms

6. The realization of advanced functions of wind power operation

6.1 The wind units state detection and early fault warning

Wind farm remote monitoring system will monitor and process the real time data condition of fans operating on-line and make a classification of fans under states such as running, fault, overhaul, reset, etc. It takes the structure of chain components, variable speed running

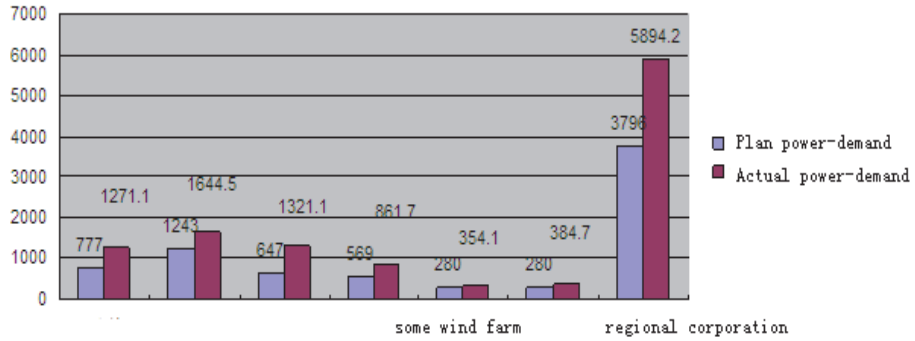

Fig. 9. The comparison chart of plan power-demand and actual power-demand in some month

The real-time data and historical data query from 0 to 16 o'clock is shown in Figure 10:

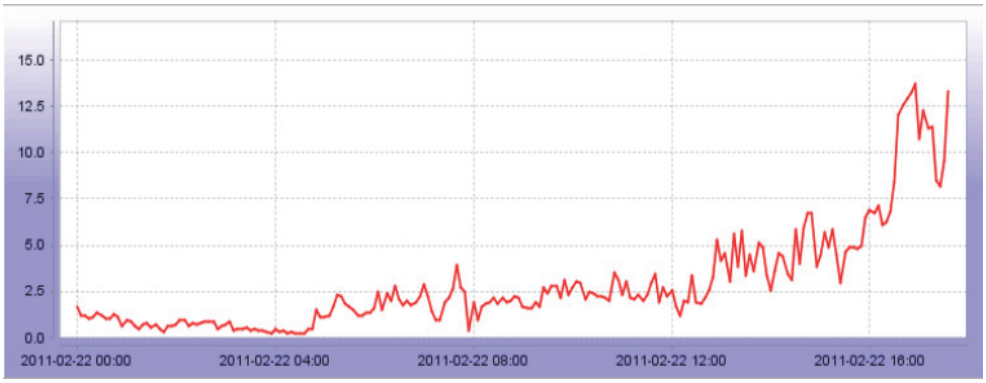

Fig. 10. Real-time data and historical data query from 0 to 16 o'clock

condition and hostile using environment such as high or low temperature into consideration. Through the use of reliable data collection system and international advanced fault diagnosis technology, it makes accurate judgment on the location where fault occurred and conducts remote and real-time monitoring of the running states of fan transmission chain (spindle, gear box and generator, etc.), the engine, vanes and tower drum, etc. It pre-warns diagnoses and analyzes the equipment faults. Abnormal states occurred in operation such as the malfunction of transmission device and generators caused by device state imbalance, rolling bearing damage, correcting error, etc. are detected out before fan fault happens. Thereby early fault diagnosis is achieved to determine the properties, types, location, degree, cause of faults. Then it points out the development trends and consequences, puts forward countermeasures to control its continued development and eliminate faults, and makes a classification of the fault types automatically. The faults include inverter reset overtime, generator speeding, temperature being exorbitant in high voltage transformer, temperature being too low in the cabin, etc. If failed to detect the fault, it will give rational proposals and instruct maintenance engineers to accomplish the

overhaul of the fan. It also provides scientific basis for the preventive maintenance by users, thereby reducing fan maintenance cost significantly.

It monitors multi-groups of data simultaneously, including: rear bearing and fore beating rotation speed and vibration of Generator, rotate speed of high-speed shaft, cabin yaw state, gearbox low speed shaft, intermediate shaft,, high-speed axis, input shaft, the gear ring vibration and oil temperature, vibration condition of Spindle fore bearing and spindle rear bearing, leaf temperature freezing, etc. Through the establishment of condition monitoring library of wind turbines of the same type, fans with big state variation are acquired automatically for fault forecast and analysis, thus completing fault pre-warning. Fan monitoring scheme is shown as follows:

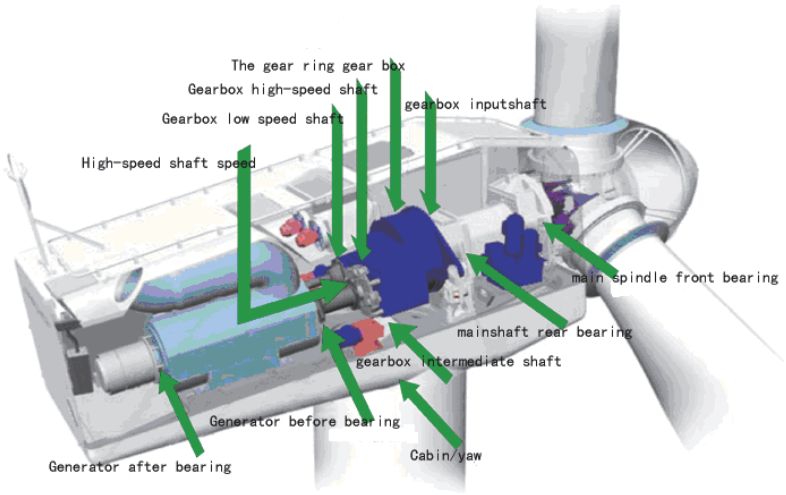

Fig. 11. The scheme of fans' monitoring

1. The reliability statistics evaluation scope of fan unit is bounded by export master switches of wind turbines, including wind wheel, transmission variable speed drive system, generator systems, hydraulic system and yaw system, control system, communication system and corresponding auxiliary systems.
2. The reliability statistics evaluation of wind farms includes all the generating equipments. Besides wind turbines, it also includes box transformer, confluence lines, main transformer, etc, and corresponding accessory and auxiliary equipment, common system and facilities.

6.2 Fan operation optimization

After wind farms are connected to grid, output of the regular generating units in the system shall change due to the injection of wind power. Since wind power is a constantly changing, we must keep adjusting and compensating the regular generating units in the system in accordance with the changing of wind power so as to keep the system in a certain balance

state. In the operation process of the wind power system, all the electric parameters of the system will change accordingly. Due to the increase of wind farm capacity, it will lead to bigger changes of the transient states of node voltages, system frequency, etc. When the proportion that the capacity of wind farms occupies in that of system reaches a certain level, some of the electric parameter indexes of the system will surpass the allowed range and the system might lose stability. Therefore, the low voltage ride through ability of wind farms is introduced.

When the proportion of the installed capacity of wind power in electric system is relatively large and the power system malfunction caused the fall of voltage, the off-grid of wind power shall influence the operation stability of system seriously, therefore wind turbines should possess low voltage ride through (LVRT) ability to guarantee the uninterrupted grid-connected operation of wind generators after system failure.

Wind generators should possess low voltage ride through ability:

a. Wind farms must possess low voltage ride through ability to maintain operating 620ms when voltage has dropped to 20% of the rated voltage;
b. Wind farms must keep grid-connected operation when the voltage of wind farms is able to recover to 90% of the rated voltage within 3s after it felt;
c. Wind power must keep uninterrupted grid-connected operation when the voltage on the high voltage side of the substation in wind farms is not lower than 90% of the rated voltage.

The acceptable wind-power capacity of power system is influenced by factors like grid transmission capacity, peak load adjusting capability, degree of stability, voltage fluctuation, etc, among which the peak load adjusting capability that the grid can provide for wind power is the most fundamental restraining factor, which is closely related to system load property, property of power and output power size. If grid-connected wind power exceeds the peak load adjusting limit that the grid can, it would be difficult to balance wind power output, leading to the out of limit of frequency and even break down of the grid in a serious situation. Since the ability of Grid system to accept wind power is restricted, added by the uncertainty of wind power, power quality and power system operation shall be seriously influenced after the wind penetrate power exceeds a certain value. Scholars have done a lot of research work in this field and points out that the current acceptable wind power of the grid in China cannot exceed 15%. Therefore, enhancing the security construction of grid is significant to the connecting of wind power to grid. If wind speed and wind power can be accurately calculated, it will be helpful for the dispatching departments in power system to make timely adjustments on dispatching plan and the adverse impacts of wind farm on power system shall be effectively reduced or avoided.

Fan operation maintenance optimization decision support system mainly includes: establish mathematical model and simulation system of wind power equipments; study the operating rules of wind generator and optimize operation system, combining the condition monitoring analysis and diagnosis system, adopting the form of unattended or less people on duty, establish wind power operation maintenance system which combines with wind power information system to improve the operation efficiency of the wind system.

The biggest difference which distinguishes wind power from other energies lies in the random variation and uncontrollability of its source power. Wind speed is not only influenced by large-scale atmospheric motion, but also affected by micro-scale atmospheric turbulence movement caused by many kinds of surface factors; therefore the wind speed presents strong random properties on instantaneous changes of time and space. Many key

techniques in wind turbine control and wind farms grid-connected operation are developed to adapt to the randomness of wind variation.

Wind power generation leads to the increase of uncertainties in power system due to the randomness of wind power, which raises new challenges for the safe operation of power system. If we were able to make relatively accurate predictions on the wind speed in wind farms, it would help the dispatching departments in power system make advanced adjustment on dispatching plan when necessary, which can effectively reduce the influence of wind power on grid security.

With the increase of the proportion of wind generation in the power source structure of power grid, the randomness, intermittent and volatility of wind generation bring a series of problems to grid operation security. The dispatching departments can only roll blackouts to cope with those problems at the moment. Effective predictions on fan generating can help the dispatching departments in power system make various power dispatching plans so as to reduce wind power brownouts, thus reducing the economic loss that power brownouts bring to wind power owner and increasing the return of investment in wind power.

Wind power predication module possesses high precision data meteorological forecast function, wind power signal purification, high-performance space-time model classifier, networked real-time communication, general wind power information data interface and other high-tech modules. It can accurately forecast the load of wind farms in future 168 hours - time curves, which will help wind farm production personnel arrange reasonable operation patterns for wind farms and reduce discarded wind. The average forecast precision rate of the system is over 80%, which can meet the electric load dispatching requirements in wind farms. The system is up to the individual wind power at the prediction error less than 25%.

The functional principle diagram is shown below:

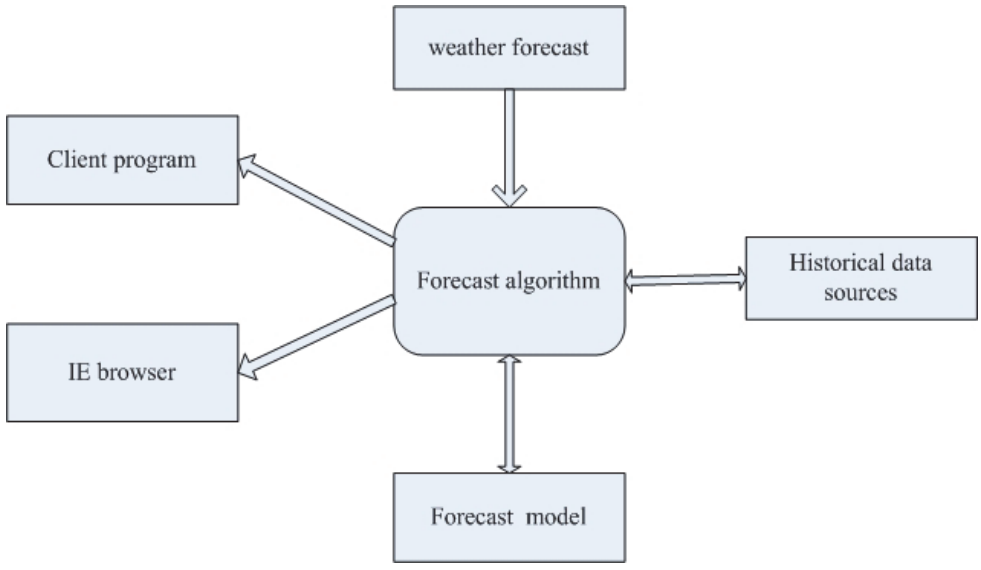

Fig. 12. The diagram of wind power prediction function principle

Prediction error of wind speed in wind farms is mainly decided by forecasting method, prediction cycle and the wind properties on the prediction site. Generally speaking, the shorter the forecast cycle is, the more moderate the variation of wind speed on the prediction site is, the smaller predicting error will be; on the contrary, the predicting error will be bigger.

The present prediction methods of wind speed mainly include Kalman Filtering method, random time sequence method, artificial neural network method, fuzzy logic method, spatial correlation method, etc. Random time sequence method needs a large amount of historical data in modelling, but it can set up a prediction model only by knowing a single speed in wind farms or a power time sequence. Spatial correlation method, taking many groups of data of wind speed in wind farms and several neighbouring sites into account, makes wind speed prediction using spatial correlation between wind speeds of several sites. Its collection of original data is enormous, but due to the increase of issues that should be taken into account in the prediction process, the prediction effect of spatial correlation method is relatively good. Artificial neural network possesses features like parallel processing, distributed storage and fault-tolerance, etc, and capabilities such as self-study, self-organization and self-adaptive, which are effective in solving complex problems. It can be used in wind speed prediction but problems like slow training speed exist.

Support vector machines (SVM) further explain the institutions risk minimization principle in learning theory, the prediction effect of which is good. Support vector machine seeks optimal compromise between the complexity of model and learning ability according to the limited sample information in order to obtain better generalization ability. Support vector machine is similar to multilayer feed forward networks in form, and it can also be used in pattern recognition and nonlinear regression. Support vector machine is most practical in speed prediction considering the highly nonlinear of wind speed data.

Calculation of the system uses support vector machine approach and adopts Gaussian radial basis function as its kernel function. It establishes regression estimation function expression using the regression estimation algorithm based on support vector machine and shows us the network structure of support vector machine. Due to the highly nonlinear of wind speed, point estimate of the relevant data constitute the training sample, and solve objective function. Point the relevant data to constitute the training sample, and solve objective function

Gray GM (l, 1) model is widely used in production researches like the load prediction of power system and possesses high forecast precision. Since the GM (1, 1) model is an exponential growth model and wind speed is a complex nonlinear systems affected by many factors, especially sensitive to seasonal change, taking one growing trend into consideration is not enough. Accordingly, the prediction accuracy of wind speed with periodic fluctuations is unsatisfactory. In order to improve the prediction precision and expand model applicable scope, we could promote GM (l, l) model to GM (1, 1, λ) model and then build up corresponding differential evolution method to solve the model. Compare the prediction values acquired through two kinds of forecasting methods, select the result with small errors and conduct the prediction and calculation of wind power. This system adopts both Support vector machine and Gray prediction in its prediction, and then it fuses the acquired information using information fusion technology to get preferable prediction effects.

Power of wind generator is mainly decided by the wind speed of the place where blades locate. If the wind speed is below a certain value, the wind generator cannot generate

electricity and power output is zero; while when the wind exceeds a certain limit, wind-driven generator will brake automatically for the sake of self-protection, power output of the wind-driven generator in this situation is zero as well. Power properties of wind generators are shown below:

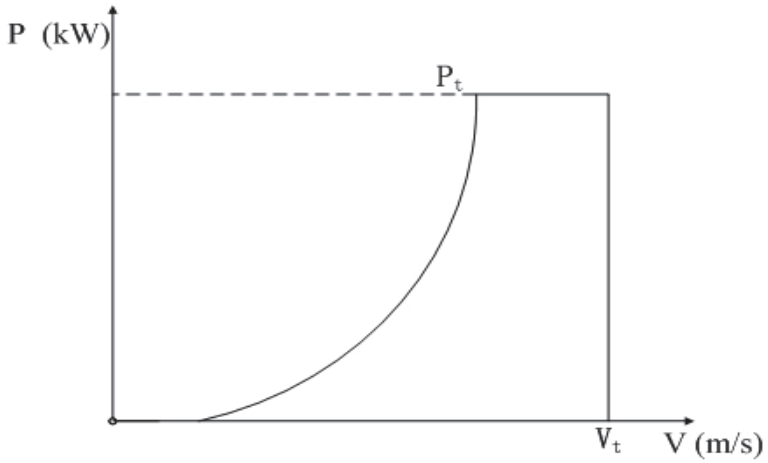

Fig. 13. The wind generators' power characteristics

The wind power is cube to the speed of wind. Wind power forecasting and wind speed forecasting follow the same principle, but the prediction error of wind power is greater than that of wind speed, the main reason of which lies in the corresponding relationship of wind speed and wind power generation.
The comparison chart of forecast power and realistic power is shown in Figure 14.

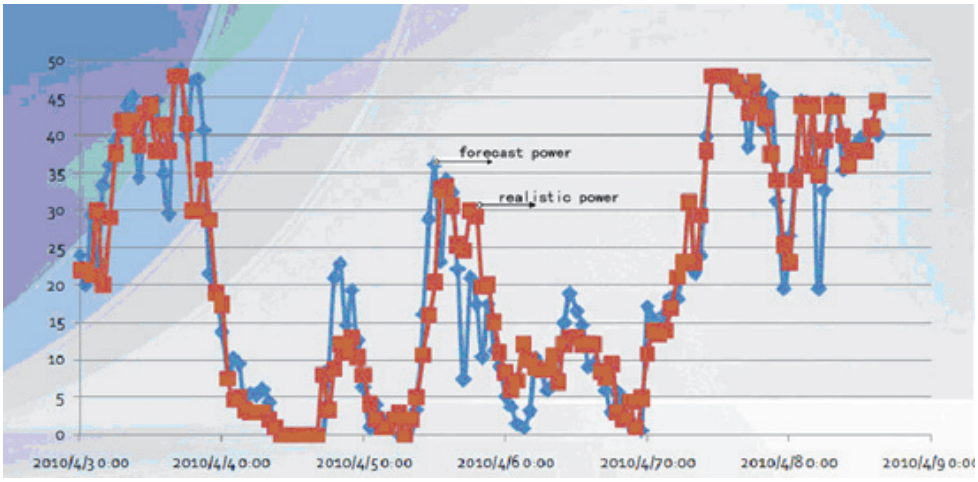

Fig. 14. The comparison chart of forecast power and realistic powe

Wind speed predictions in wind farms is a most important means in reducing undesirable impacts of wind power on power grid. One of the most typical applications of it is in the real-time control of wind farm and grid scheduling. Make further decisions based on the information acquired after corresponding calculation and processing according to the wind forecast value given by wind speed forecast system, thereby AGC—power grid dispatching power setting and automatic power control is realized finally.

The traditional economic dispatch in power system is divided into static optimal scheduling and dynamic optimization scheduling. Static optimal scheduling only seeks optimal target at certain time section of the power system without considering the intrinsic link between different time sections; while the dynamic scheduling takes the coupling of different time sections into account, thus its calculation process is more complex than that of static optimal scheduling, but its result is much closer to actual requirements. As wind speed changes randomly, dynamic model is more suitable for the economic dispatch of power systems with wind farms.

Automatic generation control is achieved through a closed-loop control system. It gets real-time measurement data from SCADA, calculates out the control commands for each power plant or unit, and then sends them to the controller of each power plant though SCADA. The power plant controller adjusts the unit power and makes it track the control commands of AGC

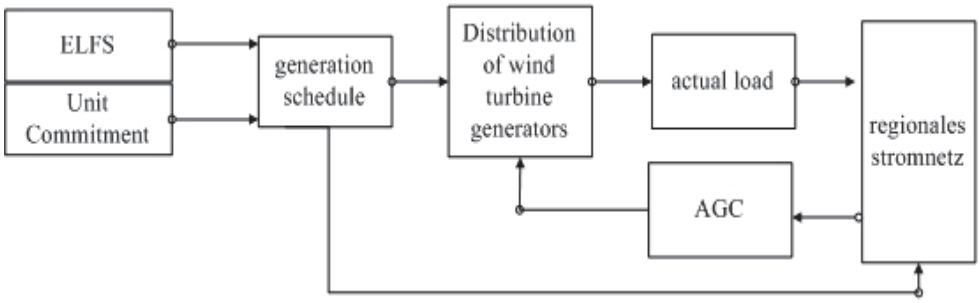

Fig. 15. Automatic generation control(AGC)

At first, wind farm centralized control center formulates a generation plan based on the wind power forecast system of wind farms and reports it to the regional grid dispatching company, and then the dispatching company distributes power generating units according to the generating schedule. When the actual load is inconsistent with the planned power, grid dispatching will reflect the deviation to units and make timely adjustments, thus achieving the purpose of automatic control.

7. Data collection and analysis of the booster station

The preliminarily design of the booster station data acquisition of this system is to collect remote metering, remote surveillance, and remote regulating from wind field booster station SCADA. The program has been carried out in Hebei Construction Investment New Energy and the results are good. There's a centralized control system aiming at booster station in the present centralized control station named RCS-9001 SCADA, which includes analogue

(P, Q, I, U, f, etc.), status quantity (switch, knife switch, accident total signal and protective device movement and status signal), electric power with time, BCD code, accident sequential record (SOE), plan value curve and protective device installation value, measured value, action message, warning information, regression signal and so on.

The repeater communication is an essential work in the centralized control station system. As the relationships between scheduling systems are becoming closer and closer, the repeater content are increasing. RCS-9001 is as a platform for dealing with the repeater, which can define the forwarding of any data in the database and define the forwarding cycle of different data. It is capable of communicating with other monitoring station systems and interconnecting with other SCADA systems.

With the development of substation integrated automation, acquiring booster station data from the RCS-9001 SCADA system is more reasonable and convenient. The communication protocol we chose is the NARI DISA communication protocol, which is developed based on the DL451-91CDTprotocol.

The chart below is a wiring diagram of a wind farm, which shows the remote metering, the remote surveillance, etc.

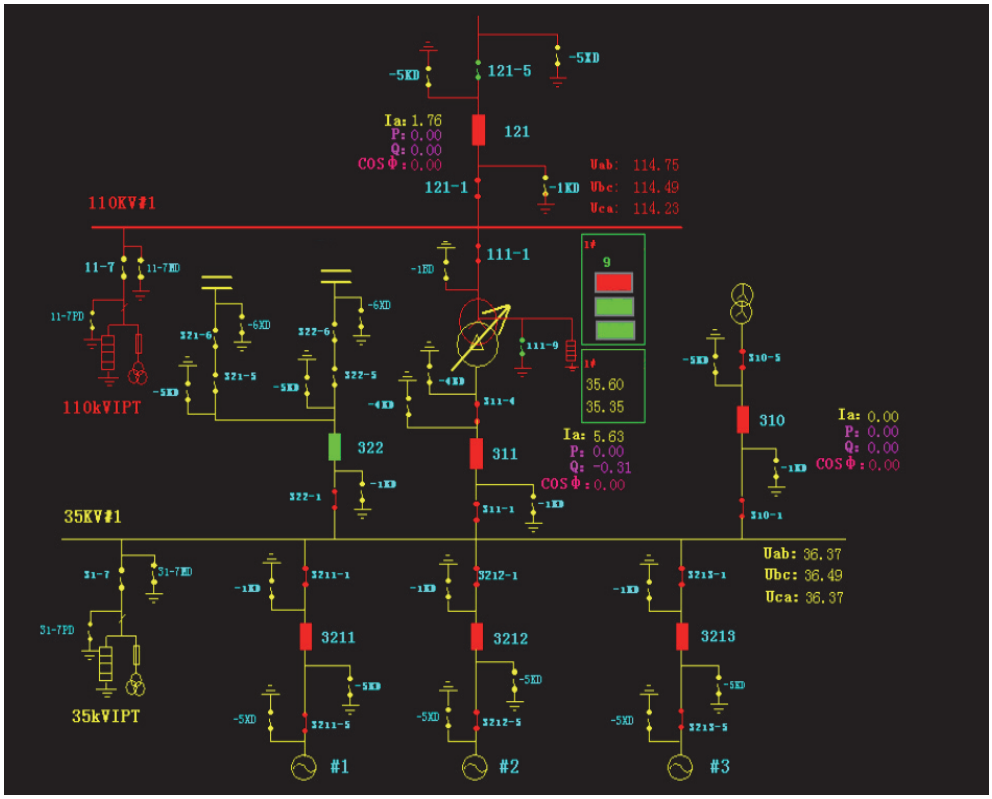

Fig. 16. Automatic generation control(AGC)

8. Conclusion

With the actual project of wind power remote monitoring and fault pre-warning as its background, this article introduces the overall system development process, network topology, the OPC data acquisition system on wind farm side, the real-time / historical database of control station. This system releases data through the B/S platform and offers information on the monitoring and operation state of wind turbines, real-time power, etc. Users can easily check the he main production information of company including the core business of production management like wind power operation, booster station operation, etc. and contents like production logs. You can acquire real-time production information from macro to micro quickly, easily and quite friendly by browsing a page.

The paper also introduces emphatically the data analysis and fault alarm function of wind farms, including:

1. Monitor and process the real-time on-line operation data state of wind turbines; make a classification of wind turbines under the states of running, fault, overhaul and reset and establish the condition monitoring library for wind turbines of the same type, which picks out the operating wind turbines with big state variation automatically and conducts fault prediction and analysis, thus accomplishing fault pre-warning;
2. Establish mathematical models of wind power equipments and a simulation system; optimize the operating system combing condition monitoring analysis and diagnosis system through the wind generator operating rules, and establish the wind power operation maintenance system which combines with the wind farm information system.
3. Both support vector machines and Grey prediction are used in prediction; conduct real-time forecasts on the wind load of the future 168 hours using the information fusion technology; help the production personnel of wind farms arrange reasonable operation modes for wind farms, reduce discarded wind, and increase the investment return of wind farms.
4. Make predictions on the wind speed in wind farms to reduce the undesirable impact of wind power on grid; get relevant information after corresponding calculation and processing according to the predicted value of wind speed given by the wind speed prediction system; then make further decisions based on that information, thereby realizing AGC - dispatching power setting and automatic power control.
5. DISA communication agreement is used in gathering information of the booster station to achieve the collecting of remote metering, remote surveillance, remote regulating, and realize wiring diagram of substation.

The aim of Wind power remote monitoring and fault pre-warning system is to accomplish the information platform of wind power enterprises and provide timely, complete and accurate information service, helping wind power enterprises improve their modern management level and realizing data share in all aspects. Wind firms production computerized management platform is built up according to the ideas of integration, platform initialization and componentization using the most advanced computer technology. Based on the most advanced enterprise production integrated management system, the system successfully carries out computerized managements according to the profession features of wind power companies on the operation of wind power companies, maintenance, statements, aided decision-making, prediction control, etc.

9. References

Ye Chaobang. The design of OPC sever with data require.North China Electric Power University. 2006.

Vu Van Tan, Dae-Seung Yoo, Myeong-Jae Yi. Design and Implementation of Web Service by Using OPC XML-DA and OPC Complex Data for Automation and Control Systems. The Sixth IEEE International Conference on Computer and Information Technology, 2006.

DCOM configuration illustrates. Huafu opctkit. User notebook.

Pan Aimin. The theory and application of COM. Beijing: Tsinghua University publishing,1999.

Lu Huiming, Zhu Yaochun. The standard communication agreement of controlling equipment-OPC Sever design.Beijing: mechanical industry publishing, 2010.

Bai Xiaolei. The research of wind power forecasting and AGC unit blend, Beijing Transportation University, 2009.

Wang Huazhhong. The design of SCADA. Beijing: Electronic industry publishing, 2010.

Bouter, S, Malti, R, Fremont, H. Development of an HMI based on the OPC standard[J]. EAEEIE Annual Conference, 2008 19th.

Part 5

Wind Turbine Generators

5

Superconducting Devices in Wind Farm

Xiaohang Li
Innova Superconductor Technology Co. Ltd. Beijing
China

1. Introduction

Wind power is very promising in the near future and drawing more and more attentions from the governments and enterprises world wide. The global wind power industry expanded rapidly in the recent several years. In 2009, the world's total generation capacity of wind power was 157.9 million kW, of which ~ 31% was newly installed within the year. From industrial reports, the installed wind power capacity will increase by more than 30% per year in the following decade, especially in China, where GDP and power consumption are boosting quickly. It is estimated that in China, the installed wind power capacity will exceed 150 million kW and supply ~ 15% of the country's needs by the year of 2020.

In a common view, wind energy is clean, renewable and abundant. The estimated global resource of wind power is up to 2.74×10^{12} kW, while the exploitable capacity is ~ 2×10^{10} kW. Further more, wind power is free of environmental impacts compared to traditional power resources, such as the hydro, thermal and nuclear power. However, energy density of wind power is low, and the wind energy resources are distributed, i.e., the majority of them is located in the rural areas, the coasts and the offshore sea shelves. At the background of global energy shortage, governments and enterprises are pushing forward the construction of new and large wind farms in these outfields. In the past several years, following the quick developments of wind power plants in the plains and highlands, the United States, Japan and Europe began to install offshore wind power turbines. For example, in April 2010, the first offshore wind plant in Germany was installed in the North Sea. This plant consisted of twelve 5 MW turbines, with annual power generation capacity of 220 million kWh.

The brilliant future of wind power emphasizes the motivation on the technical upgrades in the wind farms, including the introduction of various high temperature superconducting (HTS) devices. In the past decade, many research and test operation efforts were paid on the new and high efficiency power applications, such as “direct- driven” permanent magnet (PM) generators and HTS generators; magnet, flying-wheel and battery energy storage systems; fault current limiters; solid state transformers and electronic voltage regulators. These devices are designed to solve the problems occurring in the quick boosting up of the wind farms and the strict requirements on connecting them to the main frame of the power grids. Generally, these problems can be described as the optimization of the generator capacity, the size and weight of the wind turbine system, the stability of the output, as well as the tolerance of the system against fluctuations from the driving force, aka the wind, and the load. One of the key approaches to achieve the optimization is the superconducting

technology. Following this approach, a series of HTS devices were proposed, including HTS generators, superconducting energy storage systems (SMES), superconducting fault current limiters (SFCL), HTS transformers and HTS power transmission cables. This chapter is a basic introduction to the design and tentative application ideas of these devices. Following this part, there are 5 parts on the basic knowledge of superconductivity and HTS materials, HTS generators, SMES, SFCL and other HTS devices such as HTS cables. At the end of this chapter is a short conclusion outlining the future superconducting wind farms.

2. Basic knowledge of high temperature superconductor

In 1911, superconductivity as a physical phenomenon was discovered by Kamerlingh Onnes (H. Kamerlingh Onnes, 1911) during the low temperature conductivity measurement of Hg. In his experiment shown in Figure 1, when the temperature dropped to 4.2 K, the resistance of Hg dropped to below the limit of the measurement device, and virtually taken as zero. From then on, superconducting technology became more and more attracting in various areas, including energy, information, transport, medical, scientific instruments, defense, etc. Two key physical properties are identified in superconductor, one is zero resistance and the other is complete diamagnetic phenomenon. In electrical power application, zero resistance is often utilized as it implies high current capacity and extremely low Ohmic loss. However, diamagnetic and superconducting-normal state transition properties are also of important practical value.

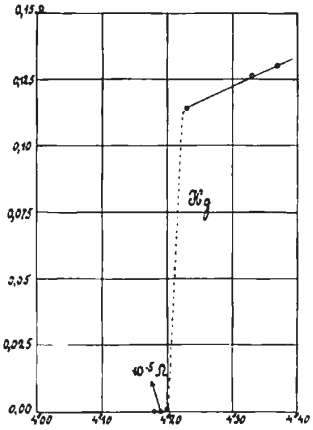

Fig. 1. The zero resistance transition of Hg measured in 1911 by Kamerlingh Onnes.

Utilizing the high current density and consequently high magnetic field density generated by the current, superconducting coils, cables, generators, motors, transformers and magnetic energy storage systems are invented and developed. Besides, based on the state transition, superconducting device can be with no resistance while carrying a current below designed value and with pronounced resistance when the current exceeds that, which makes it an excellent candidate to fault current limiter. In modern wind farm designed to supply large amount of electrical power to the main frame of the grid, superconducting devices are now widely considered. Basic knowledge of the key physical properties in superconductor will be introduced in the following several pages.

2.1 Critical parameters in superconductor

In a given superconductor, zero resistance can only occur below certain temperature and external magnetic field, while carrying a transport DC current below certain density at the same time. The three limitations are thus called the "critical" temperature, field and current density of the superconductor, denoted by Tc, Hc and jc, respectively. As shown in Figure 2, the critical limitations are correlated with each other. When two of the external parameters are zero, the limitation on the third depends only on the intrinsic properties of the material. In the other cases, superconductivity only occurs at the environmental conditions below the surface formed by Tc, Hc and jc as functions of the temperature, field and current density. In another word, the superconductor is in superconducting state only when the environmental parameters are below this surface and in the normal state otherwise. In superconductors reported so far, the highest Tc is about 160 K; the maximum theoretical Hc is up to 100 T, while the highest practical Hc is over 25 T; and the highest jc is up to 10^7A/cm^2 in epitaxial thin HTS films.

As described above, only when the ambient temperature drops below certain value, aka Tc, can a superconductor begin to show superconductivity. In a practical superconductor, the normal to superconducting state transition occurs in a temperature range around Tc. This range is then called the transition width. In HTS materials, the transition width is usually about 0.5 - 1 K, depends mainly on material homogeneity. The so called "high temperature" for superconductor implies Tc is usually higher than the liquid nitrogen temperature (77 K).

Similar to Tc, at certain external magnetic field Hc, superconductivity is suppressed too. Hc is temperature dependent and generally decreasing with temperature increasing. The field and superconductivity interaction is material dependent. Some materials allow no magnetic flux penetrates into, so they have only one Hc and are called "Type I" superconductors. The others allow partially flux penetration at fields above Hc1 while zero resistance disappear only at fields higher than Hc2 and then called "Type II" superconductors. Figure 3 shows the magnetization behavior of two types of superconductors. Practically used superconductors are usually Type II as Type I superconductors can only carry transport current in a very thin layer close to the surface, which makes it almost impossible to be used in the high current and field devices. In HTS materials, there is a special magnetic phenomenon at field called irreversible field Hirr, above which the magnetization is reversible because the flux is able to "creep" freely in the superconductor. At fields beyond Hirr, although HTS material is still with zero resistance, the free flux creeping makes it hardly to carry any transport currents as the field generated by the transport current can drive the flux out and consequently extinguish the current.

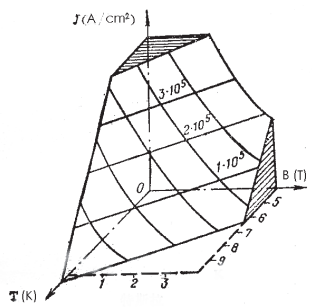

Fig. 2. Scheme of the correlations among the three critical limitations in superconductor.

In superconductor, at certain temperature and external field, resistance will generally recur when the transport current density is above certain value, jc. In applications, critical current of superconductor, denoted by Ic is commonly used instead of jc. Ic = jc.S, where S is the current-carrying cross-section. Since zero resistance is difficult to detect using conventional measurement devices, in engineering, Ic is often defined as the transport current carried by the sample when the electrical field across its length reaches 1 μV/cm.

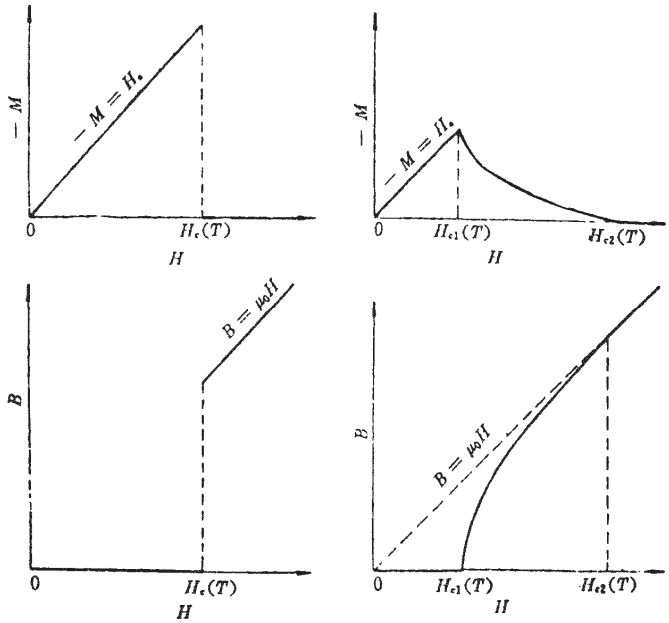

Fig. 3. Scheme of magnetization in Type I (left) and Type II (right) superconductors.

Due to zero resistance, superconducting materials can be jointed into a closed circuit, and a continuous current excited in this circuit can last for several years without significant decay. Measurement via such continuous current approach shows the upper limit of the resistivity in a typical superconductor is less than 10^{-26} Ωcm. It implies a potential application value of extremely low energy losses in various areas correlated with electricity and magnetic field. However, among more than 4000 so far discovered superconductors, only ~ 10 of them are widely utilized. The three "critical" parameters, aka Tc, Hc and jc are very important to the practical value of a superconductor. For example, discovery of HTS materials was the most exciting event in the late 1980s because it opened a new front of applied superconductivity characterized by low energy cost and high efficiency, especially in the renewable electrical power area by allowing the operation of superconducting devices in the comparativly cheap and convenient environment of liquid nitrogen temperature.

2.2 The E-I correlation

In a superconducting device design, the most important parameter to decide is the working current. It depends on both Ic and the voltage - current correlations in the material. Apply a transport DC current I to a sample and record the voltage U across it, normalize U to the

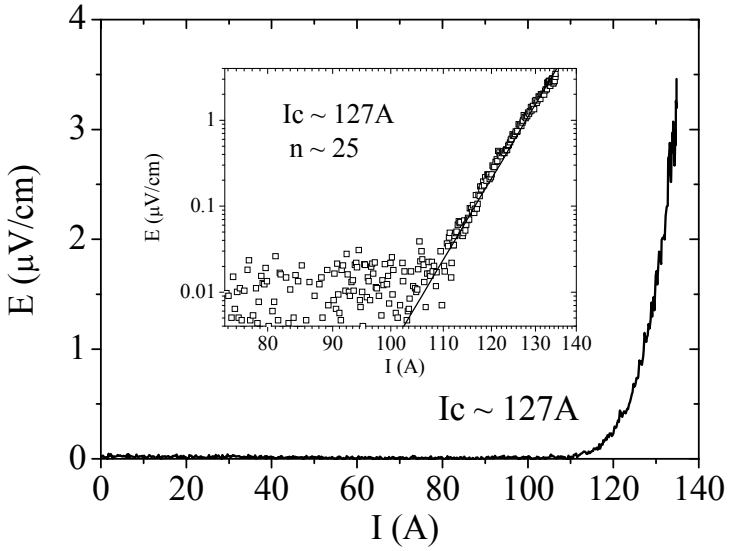

Fig. 4. The electric field - current (E-I) correlations measured in HTS wire at 77 K, self field. The inset plots the same curve in expotional coordinates to show the estimation of n value.

sample length l as the electric field E = U/l, the voltage – current correlations in the sample can be illustrated as Figure 4. With I increasing, initially the sample shows zero resistance, E is zero. When I rises to near Ic, E starts to rise rapidly with I. The E-I curve in this stage is commonly nonlinear. Finally, when I is much larger than Ic, the sample is fully transferred into the normal state, the E-I curve becomes linear and satisfying the Ohm's law, E = IRn/l. Here Rn is the normal state resistance of the sample. A so called "power law" was proposed to describe the E-I correlations at transport current I around Ic:

$$E = E_0(I/Ic)^n \tag{1}$$

In practical measurements, E_0 and n can be regarded as fitting parameters. According to the engineering criterion of Ic, E_0 = 1 μV/cm, while n is sample dependent. In a completely homogeneous sample, n represents the intrinsic properties of the superconductor. However, due to microstructure distributions and impurities, transition from superconducting to the normal state in a practical sample is usually inhomogeneous, the E - I correlation curve is then broadened in transition width and n is also smaller than the theoretical. In practical usages, especially where superconducting wires are concerning, it is generally believed that the greater the n value, the better uniformity of the material, aka the material will transfer into and out of the superconducting state more simultaneously at given environment. Thus, in magnets and superconducting power devices, which commonly use a pronounced length of superconducting wires, n value is important. The n value in commercial low temperature superconducting materials such as NbTi multi-filament wire is more than 40, much larger than that in HTS wires. For example, in Bi2223/Ag wire, n is generally less than 30, while in YBCO coated conductor, n can be comparatively larger. It is believed that the ceramic nature of HTS materials, i.e., the grainular structure, disorder region and/or the angles between the grain orientations are reasons for the comparatively bad homogenuity and small n value.

2.3 The AC losses

Zero resistance only occurs in the superconductor carrying DC current less than Ic(B,T) and at stable or zero background electromagnetic fields. In AC cases or at alternating fields, due to forced movements of the magnetic flux, there will be energy losses in the superconductor, which usually called AC losses. In bulk or single filament materials, AC losses are mainly the hysteresis loss. The definition of hysteresis loss is in analogy to that in FM materials, when a superconductor is applied to alternating magnetic fields either from AC transport current or the environment, magnetic flux lines will enter and exit, and the work done to overcome the flux pinning forces is the hysteresis loss. Thus, hysteresis loss is proportional to frequency. In multi-filament superconducting wires, in addition to hysteresis loss, there are coupling loss and eddy current loss. The coupling loss comes from the lateral flow of the current in the sheath material between the filaments, and is proportional to the square of the frequency. The eddy current loss comes from the Ohmic loss of the eddy current induced by alternating magnetic field in the normal metal sheath around the superconducting core, and is also proportional to the square of the frequency. For electrical engineering, where the frequency is 50 or 60 Hz, the hysteresis loss is dominant in common practical HTS materials. Nevertheless, AC losses in superconductor are much smaller than the Ohmic loss in normal metal conductor while transmitting the same current. Thus, using HTS materials are energy saving in AC devices if AC losses and the cooling conditions are carefully considered. Methods to estimate AC losses were proposed by researchers based on critical models of the superconductor and proofed qualitatively in applications (W. T. Norris, 1969, W. J. Carr, Jr. 1983). To reduce the AC losses, thin filament wires and special wire design such as using high resistivity material as barrier layers of lateral and eddy currents are developed. For precise researches considering flux creeping and microstructure distributions, especially in practical HTS wires with obvious inhomogeneity, finite element methods are suggested.

2.4 Properties of HTS materials

The emergence of high-temperature oxide superconductors broke the temperature barrier of applied superconductivity by switching the working temperature from liquid helium (4.2 K) to liquid nitrogen (77 K). Hence, HTS devices can be small, light and efficient, with high working current density and, as the most important advantage, cheap cooling cost. By now there are several series of HTS materials discovered: La-Ba-Cu-O, (Tc = 35 K), Y-Ba-Cu-O (Tc = 92 K), Bi-Sr-Ca-Cu-O (Tc = 110 K), the Tl series (Tc = 125 K) and the Hg series (Tc = 135K). Among them Y-Ba-Cu-O and Bi-Sr-Ca-Cu-O composites are the most promising in practical applications. The crystal structures of $Bi_2Sr_2CaCu_2O_8$ (Bi2212), $Bi_2Sr_2Ca_2Cu_3O_{10}$ (Bi2223) and $YBa_2Cu_3O_7$ (Y123 or YBCO) are shown in Figure 5.

As shown in Figure 5, HTS materials are copper oxide with layered structures of complex perovskite. They are obviously anisotropic, with very different physical properties along the perpendicular and parallel directions of the copper-oxygen layer. Bulks and wires made of HTS materials have been developed in the decades after their discovery. Among them, the most promising ones are the Bi2223 and YBCO wires. Bi2223 has a derivative of perovskite structure with pseudo-tetragonal symmetry (space group I4/mmm) as shown in Figure 5b. Its coherence length is very short, at the direction along the copper-oxygen surface is 1 ~ 2 nm, perpendicular to the surface is much less than 1 nm. Thus, in strips of Bi2223, current must flow through the grain boundaries, and only well aligned grains can transport significant current. The layered structure of Bi2223 makes it possible to obtain good textured

strips using mechanical deformation and heat treatment, a powder in the tube (PIT) method was then developed to manufacture Bi2223 wires. Now, commercial Bi2223 wires are available in the length of several hundred kilometers per year, with a price of about $ 90 /kA.m. Such wires with cross-section of ~ 1 mm² can transport ~ 150 A DC current when cooled in liquid nitrogen immersion. It opens many possibilities in practical power devices such as transmission cables. However, although the theoretical Hc2 of Bi2223 is up to 25 T, much larger than that of NbTi and Nb3Sn, at 77 K, jc in Bi2223 wire drops quickly as the magnetic field rising, makes a serious drawback to the applications in electromagnetic devices such as SMES, motors, generators and transformers. Besides, the mechanical strength and AC properties in Bi2223 wire are also to be significantly improved for practical usages. On the other hand, YBCO wires were developing very fast in the past decade and now often regarded as the succession of Bi2223. In industrial reports, YBCO wires are usually called as the "second generation" HTS wires. The structure of YBCO is also layered perovskite, as shown in Figure 5c. It has an orthorhombic symmetry (space group Pmmm).

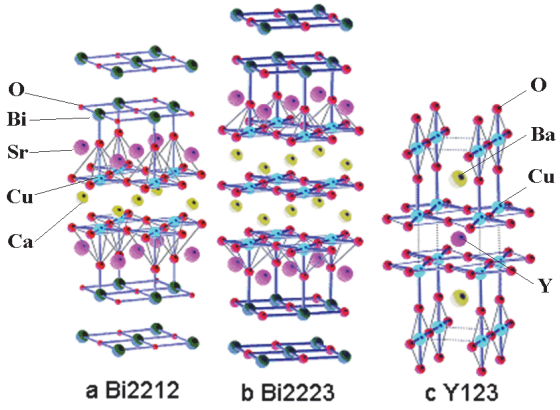

Fig. 5. Crystal structures of HTS materials: (a) $Bi_2Sr_2CaCu_2O_8$ (Bi2212), (b) $Bi_2Sr_2Ca_2Cu_3O_{10}$ (Bi2223) and (c) $YBa_2Cu_3O_7$ (Y123 or YBCO).

The c lattice constant is about 3 times of that of a and b, so it also shows significant anisotropy. Unlike Bi2223, it is difficult to prepare good textured YBCO wire using PIT method. Instead, YBCO coated conductor wires deposited on biaxial textured metal tape substrates was invented and commercialized. A schematic structure of this wire is shown in Figure 6. Hirr in YBCO at 77 K is much higher than that in Bi2223, so the jc - magnetic field correlations in YBCO wires is also much better. It is believed that YBCO wires will take the part of Bi2223 wires in most power applications, and further push forward the wide applications of HTS materials in the magnetic devices. The drawbacks of YBCO wires now are the difficulties of producing large amount of wire in comparatively cheap prices.

3. HTS generator

Decades ago, capacity of wind turbine was in the scale of kW and wind farms were mostly isolated from the power grid, and supplying power to the rural villages. At present, capacity of wind farms are becoming comparable to the hydro and thermal plants, and wind power

is going to play an important role as a major energy resource connected to the main frame of electrical services. The rapid scaling up of the wind farm demands not only large number of turbines, but also high energy density and efficiency in them. It is now widely accepted that HTS devices are promising in wind farms because the energy density in HTS devices can be 10 times larger than that in the common ones, with less than 1/3 the energy costs at the same time. Among the proposing devices, HTS generators are the most attracting. Several reports concerning 8-10 MW HTS generators developing in the States, Europe, Japan and China have been published.

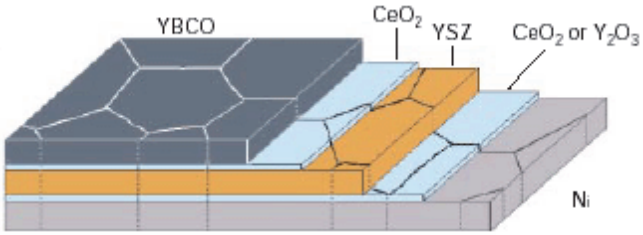

Fig. 6. A schematic structure of the YBCO coated conductor wire.

3.1 Conceptual design

As the capacity of the wind farm grows rapidly, the wind turbine also scales up quickly. At present, 2 - 3 MW wind turbines are the hot sale in the wind power industry, while turbines with the capacity of more than 5 MW are also successfully commercialized world wide. Two types of generators are currently installed in wind farms, one is high speed "doubly-fed" asynchronous and the other is low speed "direct-driven" synchronous. The former is light and compact, structured in much analogy to the generators using in the thermal plants, with 2 or 4 poles and rotates at a speed of 1500 – 3000 rpm. A complex gear system must be connected between the wheel and the generator to multiply the rotation speed as the blade velocity of the wind wheels cannot be very high. On the contrary, the latter rotates at a speed close to the wheel, which is commonly less than 150 rpm, and the gear system is simple, if cannot be omitted. The capacity of the "doubly-fed" generator is usually less than 3 MW, while the "direct-driven" PM generators are advantageous in size and weight in the capacity range of 2 – 5 MW. At 5 – 6 MW, the weight of both of the "direct-driven" PM generators and the gear box of the "doubly-fed" generators will be at the altitude of 100 tons. It makes a serious drawback to the economic benefit of the wind farm. Using HTS materials instead of permanent magnets is a proposed approach to overcome the size and weight problems in the large capacity "direct-driven" generators, because the electromagnetic field density in the HTS magnets are much larger than that in the permanent magnets.

Fig. 7 is a schematic diagram of a "direct-driven" HTS generator system illustrating the design concept. The system consists of a wind wheel, a simple/optional gear system, a HTS generator, a stand alone excitation power supply, a cooling system, a converter and a transformer connecting to the power grid. In this diagram, the wheel and the gear system are similar to those in the 3 - 5 MW "direct-driven" PM generators, but the capacity is larger and the rotary speed is also slower. For example, in 10 MW wind turbine systems, the rotary speed of the wheel is usually 8 -12 rpm, while the speeding up ratio of the gear box, if

necessary, can be 5 - 10 for the size and weight optimization in both of the generator and the gear system. The HTS generator used here is hybrid structured as widely suggested, i.e., its rotor is made of HTS materials and the stator is conventional. Fig. 8 shows a schematic diagram of the hybrid structured HTS generator. It consists of the HTS rotor, supported by torsion transmitting tubes and sealed in a cryostat (often called Dewar in scientific reports), and a conventional stator. For the convenience of connecting to the grid, the output voltage of the system V is often selected as the common values used in the substations, for example, 10.5 kV and 35 kV in China. Similarly, the output of the system is usually in 3 phases, the same as that in power grid. Thus, for designed capacity P, the output current I = 0.577P/V.

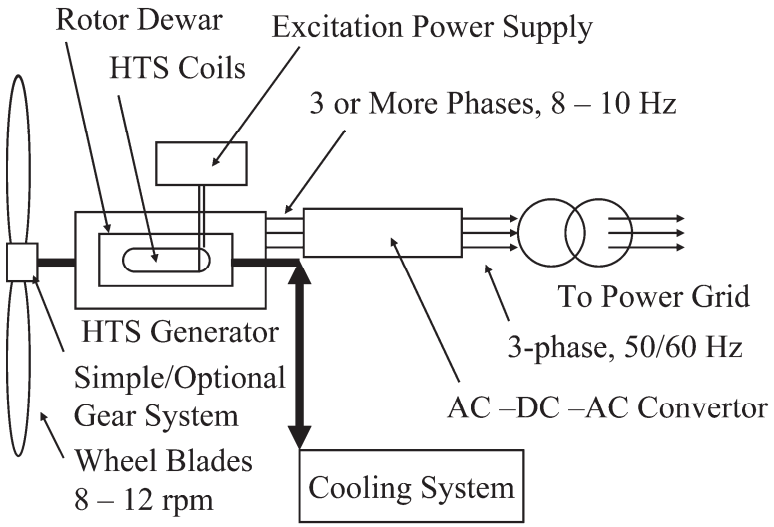

Fig. 7. The schematic diagram of a HTS generator system.

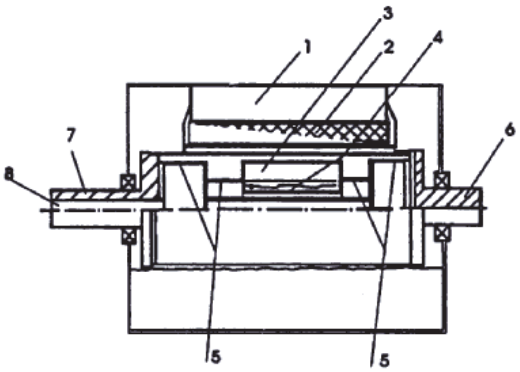

Fig. 8. The schematic diagram of the hybrid structured HTS generator. Labels in the figure: 1, Stator iron core; 2, Stator coil; 3, HTS rotor coil; 4, Rotor Dewar; 5, Torsion transmitting tube; 6, Driving shaft; 7, Supporting tube; 8, Axial tube for cooling and current transition.

However, adjusted by converter and transformer, the number of phases in the generator, as well as the generator output voltage Vg and the stator phase current Ig are not necessarily the same as those of the system, and can be optimized in generator electromagnetic design.
It is note worthy that adopting an AC – DC – AC converter between the generator and the transformer, the output frequency of the generator fg can also be adjusted. It is usually very low although the system output frequency f is commonly 50 or 60 Hz according to the grid standards. This is advantageous because the number of magnetic poles in the rotor 2p, which can be calculated by $n = 60fg/p$, decides the generator size and weight provided the materials are the same. Reducing p is particularly beneficial in the "direct-driven" HTS generators as the minimum bending diameters of commercial HTS wires are usually about 40 – 70 mm, which makes it difficult to wind magnetization coils smaller than NdFeB bulks, and a rotor with many pairs of HTS coils would be large. In common, fg in a HTS generator of several MW capacity can be 8 - 10 Hz to meet the speed requirement of the turbine, the optimized coil size and weight, and electromagnetic design convenience at the same time.
Since DC resistance in HTS material is extremely small and only DC excitation current is used for synchronous generator, the excitation power requirement of HTS generator is very low. However, the field density in HTS coil is much larger than that in conventional ones, the excitation current must be very stable, a stand alone power supply is then suggested for exciting the HTS coils. Its input power can be in the altitude of 10 kW, while the output current is 100 - 200 A, with very low fluctuations. Superconducting magnet power supply made by the Bruker Corp. can be a good candidate for this. In emergency, this device can even be activated by a set of batteries.
Besides the power supply, a cooling system is also necessary to the HTS generator. Depends on the capacity and the rotor design, around 500 – 1000 W cooling power is needed. This can be supplied by Stirling or G-M coolers, which give 200 - 500 W cooling power at ~ 77 K with 5 - 10 kW input power. At least two coolers are needed for one generator unit, an additional one as backup is suggested.
For designing HTS generators with capacity of several MWs, a number of technical issues have to be considered, including HTS material properties, especially the dependence of Ic on the field and temperature; the electromagnetic design of the rotor and the stator; HTS coil winding techniques; rotor cooling techniques and low temperature rotary sealing; energy density in the stator and stator cooling; etc. As a conceptual demonstration of HTS generator design, a 10 MW HTS generator is proposed in the following paragraphs.
At the beginning of design, the key parameters of the generator are decided first. Here, P, I, V and n are designed according to the requirements of the wind farm and the power grid. As listed in Table 1, P is 10 MW from the design goal; V is 35 kV in 3 phases to meet the standard of substations; and phase current I is 165 A calculated from $I = 0.577P/V$. After that, the most important parameters to decide are the air gap field Bg, the generator output voltage Vg, current Ig and the number of phases in the stator. Bg is decided from the working conditions and the electromagnetic properties of the materials used. To obtain the size and weight advantages of HTS, Bg in HTS generator is often suggested as 1.0 – 1.4 T, much larger than that in the conventional ones. Vg, Ig and the number of phases in the stator are depending on the materials, topology and structure of the stator, which are in much analogy to those in the "direct-driven" PM generators.
The rotor is designed with Bg, n, p and the gap width d as parameters. In HTS generator, d is usually much larger than that in conventional ones, because a cryostat must be inserted in

the gap to isolate the low temperature rotor from the room temperature parts. Considering the state of art Dewar technique, d of 10 - 20 mm can be suggested. The active length of the rotor lg is decided according to the electromotive force E and the stator topologic design. Here, E can be estimated by E = Bglgv, where v is the linear speed of the rotor pole shoes, v = 2πnRr. With p calculated from p = 60fg/n, and the properties of the HTS material used, the outer radius of the rotor Rr can be estimated using field design tools. Finally, referring to the stator material properties, the slot size and shape, as well as armature length and stator outer radius can be decided.

The key parameters of the conceptual model 10 MW "direct-driven" HTS generator are proposed and listed in Table 1. From a suggested scheme of coastal wind farm, the rotation speed n in this generator is 20 rpm and the rated generator output voltage Vg is 3000 V in 3 phases. Considering the converter capabilities and the control of the generator, the rated generator output frequency fg is selected to be 10 Hz. Thus, p = 30. Applying the reported HTS coil design parameters (Li X. et al., 2010) to this model, the schematic view of the generator and the FEM estimated field distributions in the cross-section is shown in Figure 9. In this design, the excitation current of the rotor is 80 A, the FEM estimated air gap field at the inner radius of the stator Bg is about 0.98 T, and the maximum field in the HTS coil is about 0.55 T, as shown in the figure. Considering the properties of the HTS wires used here, the working temperature of the rotor is suggested to be 65 K.

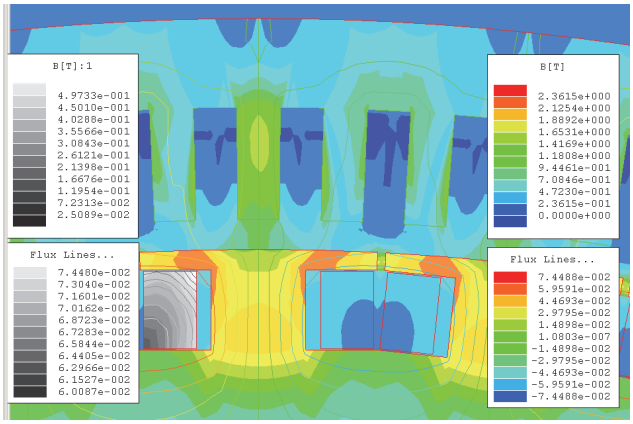

Fig. 9. The partial cross-section view with FEM results of the magnetic field distributions at 80 A working current in the 10 MW model.

The cross section dimensions of the excitation coils used here are taken from the reported 100 kW model. The coil is racetrack structured consists of 8 double pancakes. The scheme of the coil is shown in Figure 10 and the design parameters are listed in Table 1. Iron core can be used in the rotor to enhance the air gap field Bg and reduce the cost of HTS wire when the designed field of the generator is below 1.4 T. Epoxy plates are inserted between each of the pancakes and mounted at the both ends of the coils for enhanced insulation. To hold 60 such coils, the estimated circumradius of the rotor column is about 1528.6 mm. Taking the pole shoes into account, the rotor outer radius Rr is 1594 mm. With the 20 mm air gap, the inner radius of the stator is 1614 mm. Thus, the estimated electromotive force E is 1.65 V/m. At the suggested stator slot structure, where the stator outer radius is taken as 1750 mm,

thus the summed cross-section area of the stator windings is ~ 3831 cm^2, and taking the electric current density in the stator windings as 3 A/mm^2, the active length of the stator armature is ~ 7.45 m, and the estimated outline volume of this 10 MW model is 3.5 x 3.5 x 7.7 m^3, much longer than the reported European 10 MW HTS generator design (A. B. Abrahamsen et al., 2010). However, the European model is design to work at 20 K, where the current density in the excitation coil can be much larger than that at 65 K. On the other hand, because of the slim rotor and stator, the estimated weight of the 10 MW design here is only about 86 t, which maybe advantageous in practical wind farm applications.

Rated output power (kW)	10000	Maximum field in rotor coil (T)	0.55
Rated system output voltage (kV)	35	Air gap width (mm)	20
Rated system output current (A)	165	Electromotive force (V/m)	1.65
Number of output phases	3	Rotor outer diameter (mm)	3188
Rated output frequency (Hz)	50	Active armature length (mm)	7450
Generator output voltage (V)	3000	Stator inner diameter (mm)	3228
Stator phase current (A)	1924.5	Stator slot area (cm^2)	3831
Number of stator phases	3	Stator outer diameter (mm)	3500
Rated generator frequency (Hz)	10	Stator Length (mm)	7550
Rated rotation speed (rpm)	20	Excitation coil width (mm)	156
Pairs of rotor poles	30	Excitation coil height (mm)	52
Rated excitation current (A)	80	Excitation coil length (mm)	7572
Rated air gap field (T)	0.98	Winding width (mm)	36
Rotor working temperature (K)	65	Pancake coils per pole	8
Rotor current density (A/mm^2)	8.5	Turns per pancake coil	40

Table 1. Key design parameters of the 10 MW HTS generator.

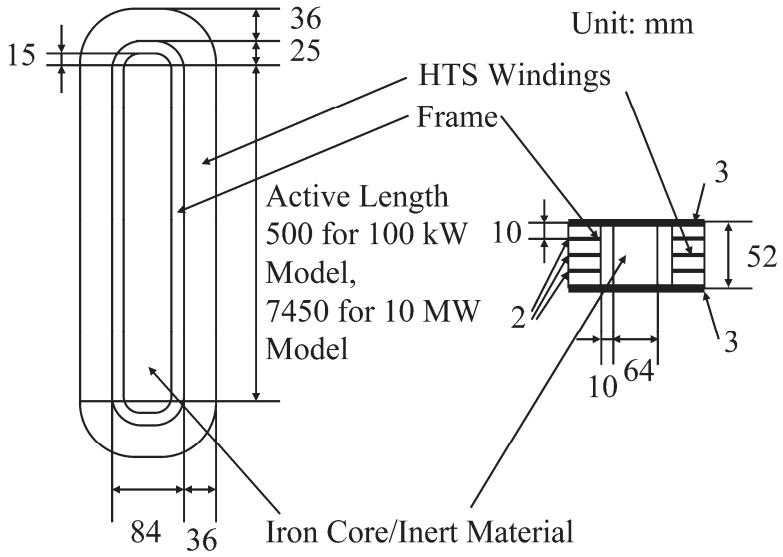

Fig. 10. Scheme of the excitation coil in the model generator.

3.2 Requirements of the HTS wire

HTS wire is the basis of the HTS generator and key to the performances. In practical using, the wire has to meet several basic requirements as listed below:

1. High critical parameters, especially jc (B, T) which characterizes the ability of transmitting high current density at high magnetic fields and reasonable temperatures. Commercial HTS wires have jc of more than 10^4 A/cm^2 at self field and 77 K, but the more important is jc at pronounced field both parallel and perpendicular to the flat surface of the HTS wire. This is still very challenging for most wire manufacturers. Besides, the tolerance of the wire against over current shock and fluctuations are also important, as in a "direct-driven" wind turbine generator, when the driving force and/or the load varies, current pulses are directly applied to the excitation coils.
2. Long defect and splice free pieces with high mechanical strength and good uniformity. Even in laboratory usages, the demanded wire length is in term of kilometers. Although a few Ohmic contacts are usually allowed in coil winding, too many joints are harmful to the performance and operating safety, especially in the conduction cooling cases. Besides, for the design and winding convenience, the wire must be in good agreement with the nominal dimensions and jc, and able to withstand the tensile and bending forces applied during coil winding, processing and operating.
3. Low AC losses. Although in synchronous generator the rotor is working at DC current and field, AC losses are still one of the important coil heating causes in magnetization and at fluctuations and current shocks. On the other hand, with low AC losses, HTS wires are able to be applied in the generator stator and other devices, such as cables and transformers.
4. Comparatively low costs. At present, commercialized Bi2223 wire costs about $ 90/kAm, while its expected lowest market price is about $ 50/kAm. Reports predicted that the YBCO wire will cost as cheap as $ 10-15/kAm in the future, but no one can insurance when this price can be achieved in the market. The price is sometimes the main drawback to the practical applications of HTS devices, because although they are better in performance and more energy efficient, they are too expensive to be accepted by the industrial operators.

In this chapter, as a basic academic introduction to the HTS generator proposed to use in the wind farm, only the first issue is discussed based on several types of market available HTS wires. Table 2 listed the basic descriptions of them. Here, the "High strength" Bi2223, "344S" and "344C" YBCO tapes are manufactured by the American Superconductor Corp. (AMSC), the "SF4050" YBCO wire is manufactured by the SuperPower Inc., while the Bi2223 wire labeled as "Innost" is manufactured by Innova.

Figures 11 – 13 show the magnetic field and temperature dependences of jc in some typical samples of HTS wires. Due to the strong anisotropy, jc in HTS wire depends not only on magnetic field strength, but also on the direction of the applied field. At the same field, jc is usually larger when the flat surface of the wire is parallel to the field than perpendiculer to. Among different types of HTS wires, Bi2223 is usually much more field sensitive than YBCO, especially at comparatively high working temperatures. However, reports show in the high pressure proccessed Bi2223 wire, jc (B, T) can be significantly enhanced. On the other hand, it is obvious that with the temperature decreasing, the critical current rises rapidly. At 60 K, for example, in most of the samples Ic at self field becomes about 2 times as large as that at 77K. Similiar enhancement of jc by lowering the temperature is also observed

at pronounced fields. Therefore, instead of 77 K, the working temperature is often selected as 20 – 65 K in the devices requiring high fields, as suggested here in the 10 MW model.

Type of HTS wire	344C	High Strength	344S	SF4050	Innost
Superconductor	YBCO	Bi2223	YBCO	YBCO	Bi2223
Stabilizer/matrix	Cu	Ag	S. S.	None	Ag
Thickness (mm)	0.18 - 0.22	0.255 - 0.285	0.275-0.31	0.055	0.19 - 0.25
Width (mm)	4.27 - 4.55	4.2 - 4.4	4.27-4.55	4.0	4.0 - 4.4
Bend diameter* (mm)	25	38	25	25	70
Tensile stress* (MPa)	200	200	300	550	80
Tension* (N)	120	210	200	-	110
Tensile strain @ 77K*	0.3%	0.4%	0.3%	0.45%	0.2%
I_{c0} @ self field, 77 K (A)	90	145	90	80	110

*Greater than 95% I_c Retention.

Table 2. Parameters and properties of the HTS wires proposed to use in the rotor.

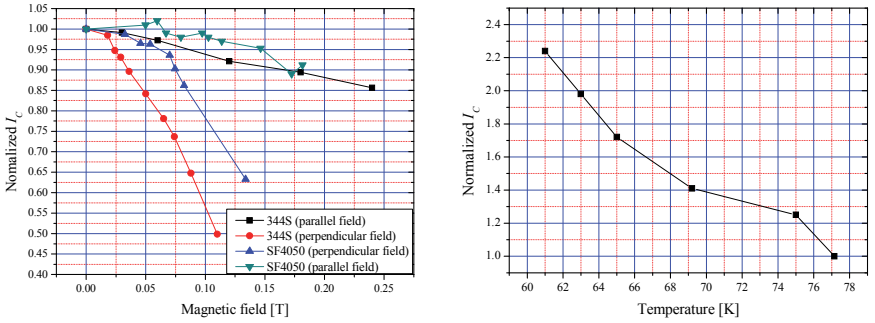

Fig. 11. Normalized Ic vs. field (a) and temperature (b) in wires from SuperPower and AMSC.

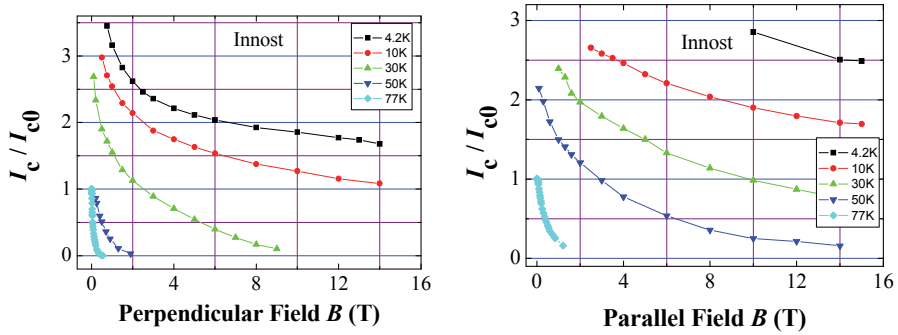

Fig. 12. Normalized Ic vs. field and temperature in wires from Innova.

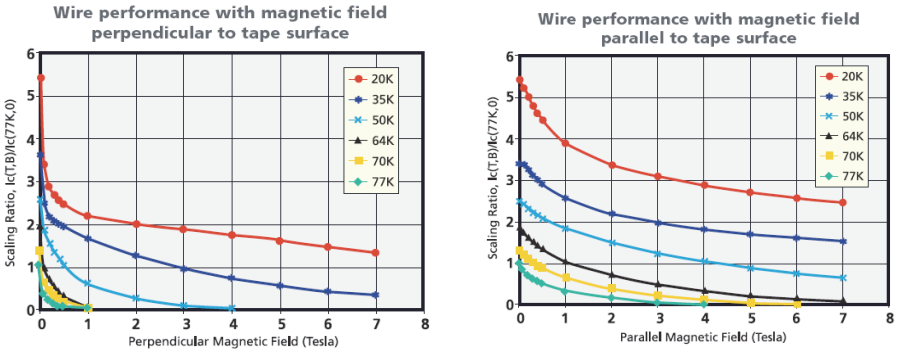

Fig. 13. Normalized Ic vs. field and temperature in Bi2223 wires from AMSC (AMSC 2009).

Besides the critical current vs. field and temperature relationships, the thermal stability and properties against pulsed current shocks in the HTS wires are also important in the design of HTS devices. It is difficult to predict the responses of HTS wire at variable over-current pulses just from theoretical models. Hence, U-I curves in wire samples are measured using 4-electrode method at liquid nitrogen immersion and quasi-adiabatic conditions simulating the heat transfer environments in the coil. The thermal insulation of the latter is made by wrapping several layers of fiberglass cloth around the about 20 cm long sample, and then solidified it in epoxy. Typical pulsed current shock waveforms are shown in Figure 14.

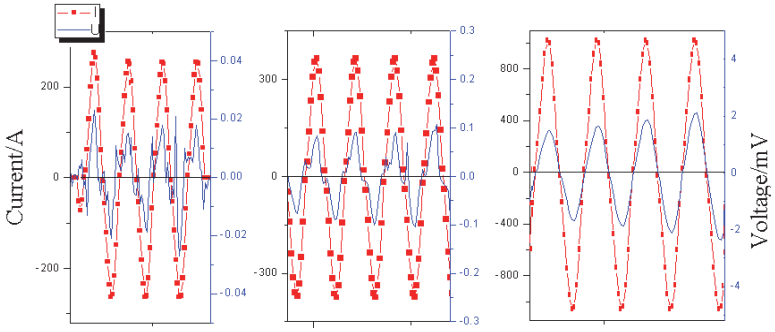

a: Imax = 2Ic b: Imax = 3Ic c: Imax = 8Ic

Fig. 14. Waveforms of the U-I responses in Bi2223 tape at pulsed currents of I_{max} = 2I_c, 3I_c and 8I_c, with duration t = 200 ms, in quasi-adiabatic environment.

From Figure 14, U-I results with the peak value of the pulsed 50 Hz AC current I_{max} up to 8I_c and the duration t = 200 ms show that during the over-current pulse, the voltage across the sample, essentially the sample resistance increases with time, indicative of a typical heat up response. Afterwards, in the setup of the experiment here, continuous working current I_w is applied to the sample to monitor the recovery processes. Figure 15 shows typical recovery results in Bi2223 and YBCO wires with different cooling conditions. Careful tests show that the possibility and time of recovery depend directly on the energy injected by the pulse and the continuous working current Iw. Three types of recovery can be identified. The first is

immediate recovery, with only slight temperature and resistance rising. As shown in Figure 14a, the U-I responses in this case show obvious reentry into the superconducting state within the period of the applied AC pulses. This indicates the heat is not accumulating in the sample. The second is delayed recovery, the reentry within the period is not obvious as shown in Figure 14b, and the recovery time can be ranged from several ms to 10 s, with the maximum sample temperature up to 200 K. Nevertheless, in this case the sample is able to reenter the superconducting state without turning off the working current. Figure 15 shows typical recovery results in this case. Here the resistance in the coil increases obviously and quickly at the occurring of the over-current, which makes it a "fault current limiter" against the pulsed current and protect itself from continuous heating up. This can be an additional advantage for the application of HTS generators in wind farms because the wind and load are frequently fluctuating. The third, however, is irrecoverable. As shown in Figure 14c, at large over-current shock and/or long pulse duration, the sample is quick and continuously heat up, indicated by quick and continuously rising of the voltage across the sample. In this case, if the working current in the coil cannot be cut off within several seconds, the coil would be directly burnt by the accumulated heat. Hence, sensors and circuit breakers are necessary in the HTS generator to demagnetization the rotor at large current shocks.

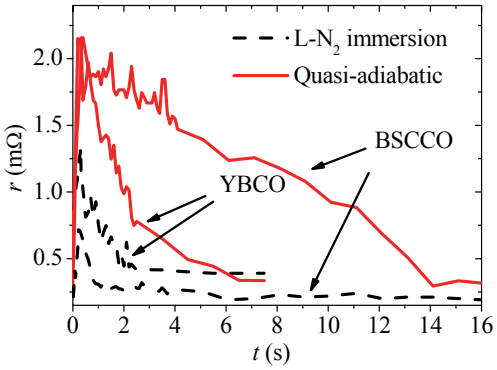

Fig. 15. Pulsed current shock recovery characterized by resistance – time correlation curves obtained at different cooling conditions in Bi2223 and YBCO wires.

3.3 Rotor coil winding and testing

To check the feasibility of the proposed 10 MW model, especially the rotor coil design and winding techniques, a 100 kW model generator with 6 poles and active length of 500 mm is developed first. The dimension parameters of the coil in the 100 kW generator are listed in Table 3. Unlike in conventional racetrack coils, the corner radius here is limited by the rated minimum bending radius of the HTS wire to keep the Ic properties. Besides, as the market available HTS wires are all in flat tape shape and can withstand little twisting stresses, the excitation coil on the pole is in stacked double pancake structure instead of the solenoid one. The otherwise design techniques are in much analogy to those in conventional synchronous generators. With designed working current of 50 A, FEM field simulation shows a gap field of ~ 0.91 T at the inner radius of the stator, and the maximum field at the coil, with DT-4 iron core to control the field distributions, is ~ 0.3 T. Thus, wires with Ic (B) > 50 A at 0.3 T field is required. FEM results of the field distributions in the coil show that the high fields

occur at the upper part and the lower-inner corner in the cross section of the coil, with a significant part of the field perpendicular to the flat wire surface. Hence, it is challenging to run this model at 77 K, because few wires have Ic > 50 A at 0.3 T perpendicular field. It is possible to enhance the current carrying capacity of the wire by lowering the temperature, and consequently enhance the energy density.

Frame corner radius	Frame width	Frame length	Coil height	Wire used (m)
25	84	550	52	2569
Outer corner radius	Coil width	Coil length	Winding height	Turns per coil
61	156	622	10	320

Unit: mm (if not labeled)

Table 3. Parameters of the HTS coil proposed to use in the rotor of 100 kW model.

A test racetrack coil is fabricated according to the parameters listed in Table 3. For electrical insulation, the wire is wrapped by 3 layers of Kapton film before winding. The thickness of each layer is about 0.01 mm. Thus, the thickness and width of the wire with insulation are about 0.42 – 0.46 mm and 4.26 – 4.51 mm, respectively. In coil winding, the middle point of the wire is firstly mounted to the inner frame and the wire is then wound towards both ends. To improve the thermal conductivity and mechanical strength, the coils are impregnated in a mixture of low temperature epoxy DW-3 and AlN powders with the weight ratio of epoxy : AlN = 3 : 1. After winding, the coil is heated to 60 °C while continuously rotating for about 1 hour to solidify the epoxy. Due to insulation, epoxy addition and other effects in winding, the mean thickness of the turns expands to about 0.9 mm, while the mean thickness of the double pancake coil, which consists of twice of the wire width, is about 10 mm including a 0.5 mm thick epoxy resin insulation plate.
After winding and solidifying, the E-I characteristics and the field distributions of the test coil are measured in liquid nitrogen immersion, and the E-I curves are shown in Figure 16.

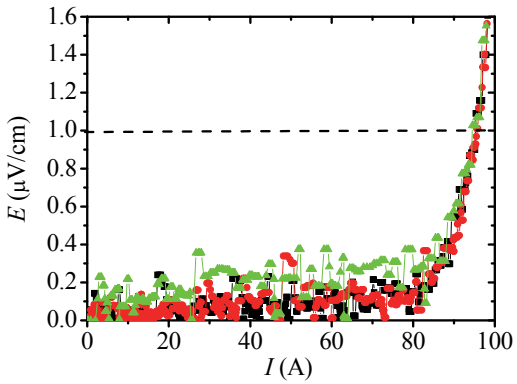

Fig. 16. E-I results in the test coil at three times repeated magnetization up to 100 A.

According to the 1μV/cm criteria, Ic of the coil is ~ 96 A, much smaller than that of the original wire, which is ~ 145 A. This degradation can be attributed to the perpendicular field

generated by the coil. Field distributions obtained by precise Hall sensor show that at 80 A working current, the field at the coil center is ~ 0.12 T and the maximum perpendicular field at the outer side is ~ 0.17 T. Three times of repeated magnetization up to 100 A with current saturating at 100 A for about 10 minutes cause no further Ic degradation and demonstrate the overload stability of the test coil.
From the above, the design concept of HTS wind turbine generator is proposed and some of the most important issues are discussed with a primary test result in a 1:1 sized test coil using commercial Bi2223 wire. The results shine a few lights on the future applications of the HTS generator in the wind farms. However, there are still a lot of works to do.

4. SMES in wind farms

SMES is an energy storage device can achieve high power density with quick response and little energy losses. Utilizing superconducting materials, the current density in SMES is 1 - 2 orders of magnitudes higher than that in the conventional energy storage coils. Due to the extremely low DC resistance, the energy stored in SMES can be kept for a period of longer than several days without significant losses. Besides, because SMES is free of energy form transition during the process of energy exchanging, it is advantageous in energy conversion efficiency, too. The energy losses in SMES are mainly rectifier/inverter losses and the power consumed by refrigeration. For HTS wire based SMES, the energy storage efficiency can be up to 94%.
With the advantages described above, SMES is able to adjust the active and reactive power in the grid, as well as compensate the voltage and current surges, especially in renewable power plants. For example, in wind power plant, the fluctuation caused by the wind can be smoothed by SMES installed between the wind turbine and the grid, and the output voltage and frequency are then regulated to meet the requirements of the power grid. Besides, SMES can also provide backup power for the coolers, the control system and the excitation power supply in the wind farm.

4.1 Structure and functions of SMES

Figure 17 shows a typical diagram of SMES connected to the power grid. It usually consists of a HTS coil to store the electromagnetic energy, which is installed in a cryostat and cooled by a cryocooler system; a reversible AC/DC converter acts as the rectifier/inverter to charge and discharge the coil; a pair of current leads connect the coil and the converter; a controller gathers the diversity signal from the power grid and the monitor signal from the magnet to generate the activation pulses and drive the converter. Commonly, the activation pulses are PWM type, which can modulate the converter output to desired waveforms. At fluctuations, a compensate signal is generated from comparing the ideal waveform to the practical ones in the grid. With this signal and the energy stored in HTS coil, SMES can work as a dynamic voltage regulator (DVR) as well as an emergency backup power supply. These functions are useful in renewable power plants which often encounter fluctuations from the resources and loads, and can help them to meet the voltage and frequency stability requirements from the main frame of the grid.
A suggested operation model in wind power plant with SMES is shown Figure 18. Currently, wind turbine will be directly cut off while encountering over-speed of wind for the safety of the instruments. However, this is harmful to the power grid stability because as shown in Figure 18 in solid line, with such working mode, the power generated from the

wind plant will drop suddenly to zero at point b shortly after it reaches the maximum. In a friendlier operation mode, the grid demands a little "inert" in the output power, aka a turn-off period within several seconds similar to that in thermal and hydro plants. With SMES, this demand is easy to fulfill. Utilizing the energy stored in the coil and the ability of waveform tailoring by the converter, SMES can give enough additional active power to simulate the "inertial" turn-off output, as illustrated in section c of Figure 18 by dashed lines. With this ability, the compatibility between the wind farm and the grid can be significantly improved. It is very helpful to overcome the technical barriers limiting the capacity of wind power connected to the grid.

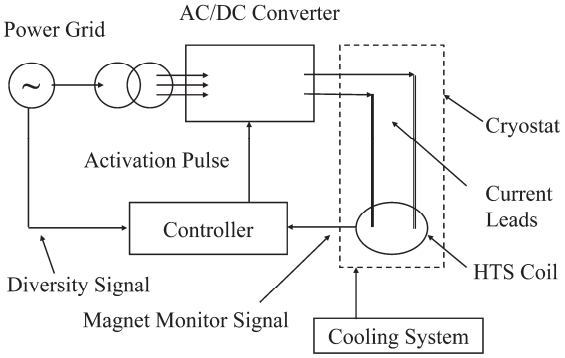

Fig. 17. Schematic diagram of SMES.

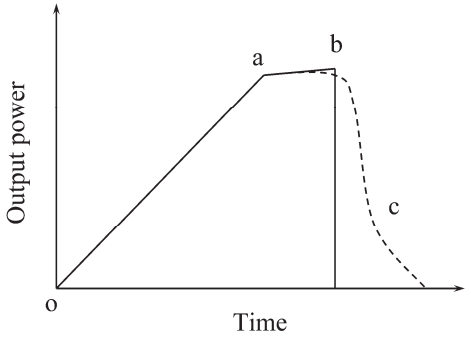

Fig. 18. Suggested operation model of SMES in the wind farm at over-speed of wind. Point a, rated output at rated speed; b, turbine is cut off at over-speed, output would jump to 0 (solid line); c, with SMES, several seconds of "inertial" output available (dashed line).

4.2 Design concept of SMES using HTS wire

The first concern in SMES design is the scale and application purposes. There are roughly three levels of scales for SMES. The small has capacity of ~ 0.1MWh that can supply several minutes of output at the end user voltage and ~ 1000 A. It is suitable for small power plants as photovoltaic stations, stand alone wind turbines, and emergency generators; functioning

as a stabilizer against the fluctuations; as well as supplying active and reactive powers for power factor correcting, phase balancing and temporary supporting to the very important loads. The medium has capacity of ~ 10MWh and can supply several minutes of output at distribution substation level. It can be installed in distributed power generating stations (DG) and middle-sized power plants to smooth fluctuations, regulate frequency and voltage, and improve the output stability and quality. Large SMES with capacity of ~ 1GWh or more can supply the output energy for several hours or even longer at the level of main-frame power transmission grids. Such SMES can work as hot backup and DVR for power system, as well as peak load adjusters and switch-connecters in the grid. In wind farms, small and medium scaled SMES are usually enough for improving the conditions of connecting to the grids.

Table 4 lists a proposed HTS magnet design for a 10 MJ - 10 MW SMES designed as output regulator for the substation level, for example, at the output end of 10 MW wind turbine. As shown in the table, the maximum field in the solenoid coil is 8.94 T. According to the jc (B, T) results shown in Figure 12, the working temperature of this SMES is selected as 10 K. Although this temperature is relatively low and the consumption of cooling power is much higher than that at 77 K, the SMES is still advantageous in energy efficiency comparing to that with low temperature superconducting wires, which must work at 4.2 K.

Type of coils	Inductance	Maximum field	Coil height	Peak power
4-solenoid	4 x 8.9 H	8.94 T	700 mm	10 MW
Rated voltage	Energy stored	Coil inner radius	Coil outer radius	Turns per coil
10 kV	10 MJ	157 mm	270 mm	~ 77000

Table 4. Design parameters of 10 MJ – 10 MW model SMES using HTS wires.

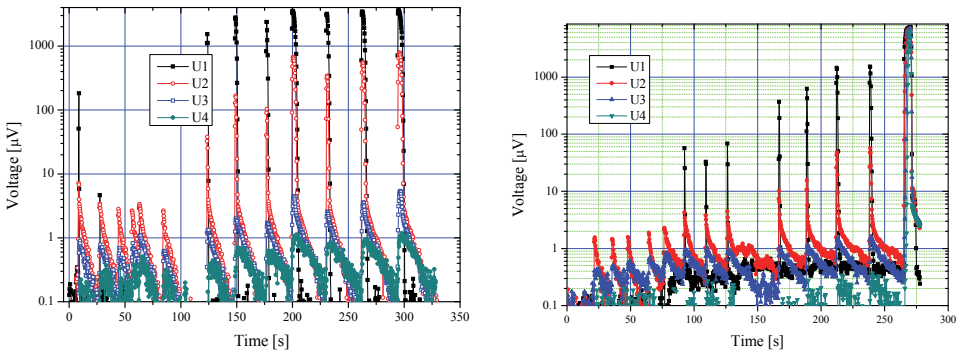

Fig. 19. Thermal heating induced quench in HTS wires working at 0.5 (a) and 0.9 (b) Ic.

Besides the jc (B, T) concerning, the properties at quick charging and discharging are also very important. In the model described above, when the peak power is 10 MW, the output current in the coil is ~ 416 A, which is about 2 – 3 times as large as the Ic at 10 K and ~ 9 T field in the proposed HTS wire. Parallel connection is used here to allow more wires share

the peak current. However, in full discharge process, the wire is at temporary over-current, while quench initiation and propagation may occur because of temporary heating. Figure 19 shows experimental results in HTS wires at thermal heating induced quench propagation at working currents of 0.5 Ic and 0.9 Ic, respectively.

In the experiment, four traces are recorded to monitor the voltages across a series of voltage comtacts in the HTS wire. At working current of 0.5 Ic, the heating current is 0.5 - 0.62A with 0.01A increments, and the duration of the heating pulse is 300ms, while at 0.9 Ic, the heating current is 0.28 - 0.42A with the same increments and the duration. Each set of peaks in the figure stands for a pulsed thermal shock. According to the results, at 0.5 Ic, irrecoverable quench occurs at the heating current of 0.62A, while at 0.9 Ic, the same phnomenon shows when the heating current is 0.42A. On the other hand, quench propagation starts at 0.34A heating current for 0.5 Ic working current, corresponding to the quench initiation energy of 0.52 J, while in 0.9 Ic cases, quench propagation starts at 0.25 A heating current, corresponds to the quench initiation energy of 0.28 J. Besides, dividing the distance between contacts by the delay time of quench in corresponding sections, the quench propagation speed NZPV in sample can be calculated. The minimum quench energy (MQE) can also be estimated from extracting the quench initiation energy injected into the wire. In Figures 20a and 20b the NZPV and MQE in typical HTS samples are shown. As demonstrated in the figures, NZPV depends sensitively on the working currents, which indicates succeeding heating in seconds after the over-current shock may accumulate in the wire and start quench. Therefore the effects of different working currents must be considered in MQE estimation, and in SEMS design, working current should be carefuly selected to avoid succeeding heat accumulation.

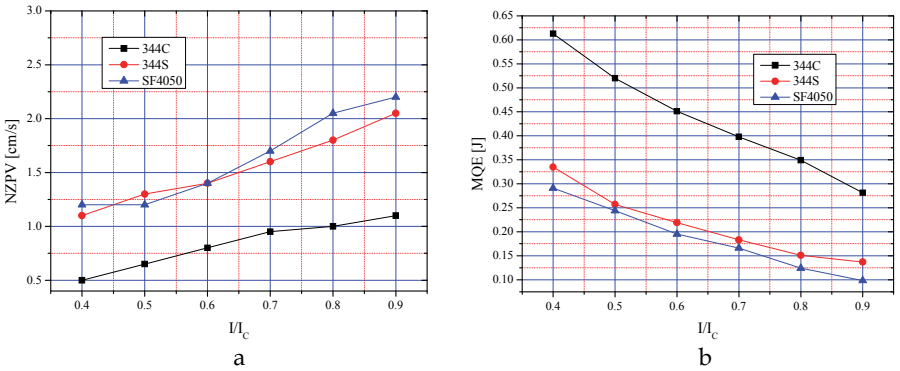

a b

Fig. 20. NZPV and MQE in typical HTS wire samples estimated from voltage-time records of thermal heating induced quench propagation.

In total, development of SMES using HTS is still in the very primary stage. Attempt to build and operate an 1 MJ/0.5 MW HTS SMES was done in China in 2006 – 2008, the system is in substation level with rated voltage of 10.5 kV aiming to be DVR and active filter against the fluctuations in the sub-grid caused by the inductance loads such as motors and fluorescent lamps. The test operation of the HTS coil was successful with full charge/discharge current of ~ 600 A, but the waveform regulator was not as stable as expected. This result shows not only the HTS techniques need further exploration for MW level SMES applications, but also the power electronics require in depth research and many more test operations.

5. SFCL in wind farms

Fault current limiter is a novel device developed quickly in the recent decade. In principle, it is a device with variable resistances which can show small resistance at the rated current and show large effective resistance at over-currents. From the state transition curve shown in Figure 1, superconductor is excellent candidate to fault current limiter. Superconducting fault current limiter (SFCL) was proposed shortly after the commercial HTS wire is available. However, in practical operation, it is not so simple to achieve even substation level SFCL as that expected. The key problem in SFCL is finding suitable method to transform microscopic effects to macroscopic ones with high energy efficiency, quick response and recovery, and safety as well. In wind farms, SFCL can be utilized as over-current protection for generators and bus buffer against surges from the grid and/or adjacent wind plants. In such usage the over-current is ~ 1000 A, with voltage around 35 kV. This makes a market for MW level SFCL.

Various topologies and structures are proposed for SFCL in the past years. Currently, SFCL of the bridge type, the resistance type and the magnetic saturation type are tested in grids and promising in industry applications. Figure 21 shows schematic structures of these types.

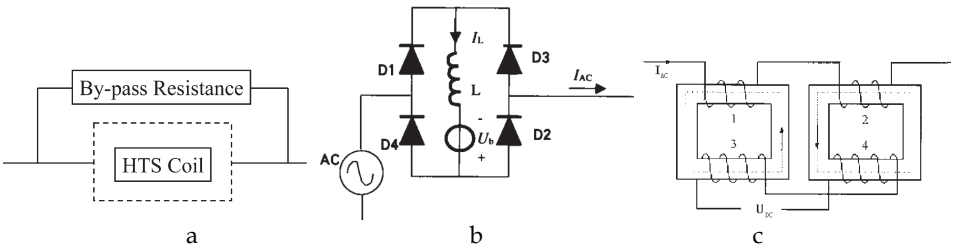

Fig. 21. Schematic structures of SFCL in the resistance type (a), bridge type (b) and magnetic saturation type (c).

Many prototype SFCL use the superconducting state transition to generate an appropriate resistance and achieve its current limiting functions. According to the definition of jc, when the fault disappears, SFCL can automatically reset and the circuit protected by the SFCL will then return to its low resistance state. As shown in Figure 21a, the resistance type SFCL uses directly the normal state resistance to limit the fault current. It is simple and combines the fault detection and reaction together, thus quick in response at most cases. The drawbacks of the resistance type SFCL are the comparatively long recovery time depends on the cooling conditions and pronounced heat generation at the current limiting stage. The bridge type in Figure 21b combines the effects of DC resistance and the inductance of the HTS coil. At the rated current, the AC part of the current applied to the coil is overridden by DC bias, and no obvious voltage dropping occurs across the coil. However, at faults, when the peak value of the current rises to larger than the bias, the AC parts will take effects in the coil and generate both resistance and impedance, which in turn limits the current. The bridge type SFCL is also quick in response with short recovery time, but the structure is complex and its capacity depends on the diodes forming the bridge. The magnetic saturation type shown in Figure 21c utilizes both high current density in HTS wires and nonlinear magnetic responses in the iron core. In this type of SFCL, when the current is small, the field generated by the DC bias in the HTS coil is captured in the iron core and saturates it deeply, thus the AC winding

presents low impedance, while at faults, the high field caused by the large current drives the iron core into and out of saturation, and the impedance of the AC windings will increase rapidly to limit the fault current.

In principle the requirement of HTS wire in SFCL is similar to that in SMES, especially the over-current tolerance and quench properties are emphasized. In the resistance type SFCL, however, the resistance after superconducting to normal-state transition needs to be as large as possible. Special HTS wire structure is developed for resistance type SFCL, characterized by ultra thin stabilizing layers or stabilizing layers/matrix with high resistivity. Besides, as AC currents and/or currents with AC parts are often applied to SFCL, the AC losses in HTS wire need to be carefully considered. Figure 22 shows the AC losses measurement results in typical HTS wires. From the results, it is demonstrated that in Bi2223 wires, the AC losses can be predicted by the Norris model, while in the YBCO wire with magnetic substrate of Ni : W alloy, extra AC losses caused by the substrate magnetization must be added to the total losses. Similar effect is also observed in MgB2/Fe wires (X. Du, 2010). This is somehow disadvantageous in SFCL usages.

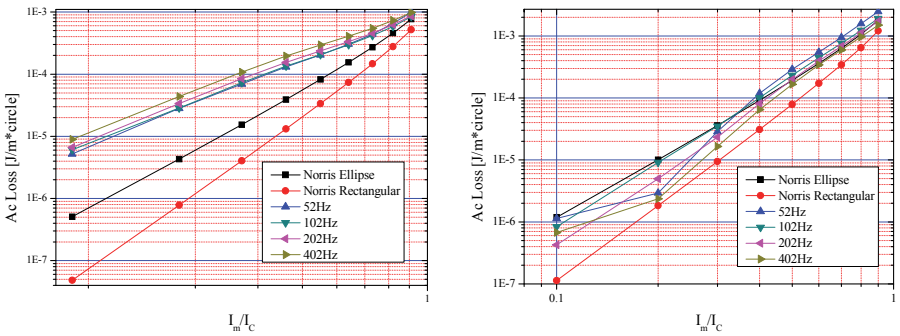

Fig. 22. AC losses in 344C YBCO (a) and Bi2223 (b) superconducting wires compared with the predictions of the Norris model.

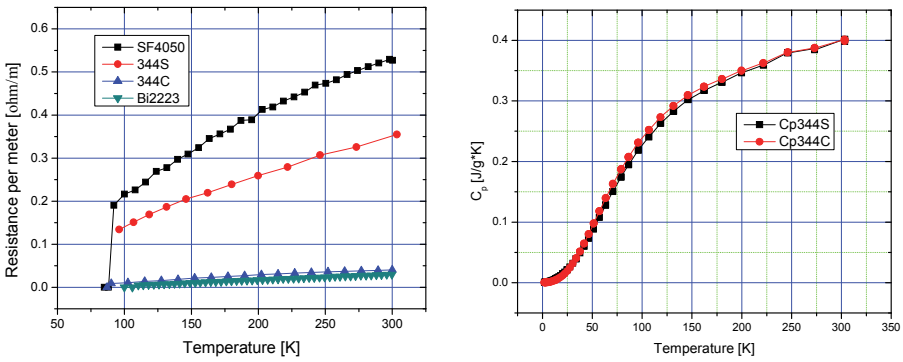

Fig. 23. Resistance (a) and heat capacity (b) as functions of temperature measured in HTS wires.

Besides, as HTS wires in SFCL are often working in the normal state, and the temperature in the SFCL can be as high as ~ 200 K after fault current shocking, the normal state resistance and heat capacity in the wires as functions of temperature are to be investigated, especially for the resistance type SFCL. Figures 23a and 23b show the experimental results of normal state resistance and heat capacity in typical HTS wires. By cooperation with manufacturers, it is possible to tailor the properties of the wire, and design SFCL with the best current and thermal responses.

A prototype resistance type SFCL is designed and tested aiming to over-current protection in HTS wind generator. In this case, the fault current is commonly below 1000 A, with pulse duration of several seconds. A matrix structure with 4 coils is designed, each two of them are serial connected, and the two branches are parallel connected. The photo of the SFCL is shown in Figure 24. In test operations of this prototype, with 0.1 Ω line resistance and 1.4 Ω by-pass resistance, the peak fault current is suppressed from 4524 A to 1017 A at 320 V short circuit voltage, while the steady state current is ~ 600 A after the 4th cycle (80 ms). At 360 V, the peak suppression is from 5090 A to 1050 A, and the saturated current is 620 A. This pilot experiment demonstrates the ability of protecting the magnetization and power generation coils in HTS generator and similar devices using simple structured SFCL.

Fig. 24. Prototype SFCL and test circuitries.

6. Other HTS devices

Besides the devices above, there are many more possibilities utilizing the superconducting techniques, such as HTS cables and transformers. Superconducting power transmission cable is a high current density device with very low resistance that works both at AC and DC currents. In wind farm, HTS cables can be the connector between the generator and the converter, and/or between the converter and the bus. In principle, superconducting cables are suitable in high current density and short distance transmission. As the energy loss in HTS cable, even counting on the AC losses, is much lower than that in conventional metal cables, HTS cable is significantly power saving. Moreover, HTS cable can also act as SFCL at over-currents, if the resistance and current capacity are carefully selected. HTS transformer

is also advantageous in the energy density with lower losses at the high current part. The combination of HTS transformer, HTS cable, SMES and HTS generator will show additional advantages by sharing the cooling system and simplifying the current leads since the low temperature parts can be connected together, with only one room temperature outlet at the end that connecting to the grid, as shown in Figure 25. The technical barriers of widely applying HTS devices in wind farm are the comparatively high prices, complex installation and operation with the low temperature systems, and lack of opportunities to operate with large electrical devices and the power grid.

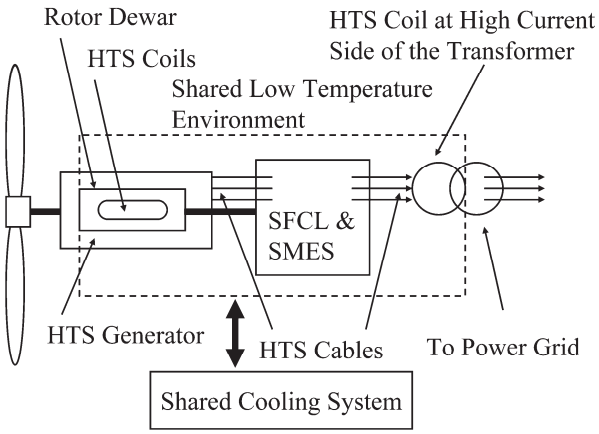

Fig. 25. Combination of HTS devices in the wind farm.

7. Conclusion

After the developing of superconducting techniques during the past century, more and more devices are invented and developed, and several of them are suitable to be applied in electrical power applications, especially in the renewable power plants such as wind farms. It is expectable that in the near future, HTS generators in 10 MW capacity, as well as SMES, SFCL, HTS cable and transformer are able to be utilized in the novel wind farm, and further enhance the economic profits as well as the serving abilities to the power grid. From now on, efforts concerning test operations at practical conditions of HTS power devices in both wind farms and substations are to be emphasized.

8. Acknowledgment

The author thanks heartily to Dr. Yigang Zhou and Dr. Xiaoji Du from Institute of Electrical Engineering, Chinese Academy of Sciences for supplying designing ideas and testing data. Thanks to Editor Ms. Romina for kindly contacts. This chapter is partially supported by the high-tech program from MOST of China, Grant No. 2008AA03Z203, and the NSFC project, Grant No. 50507019.
Special thanks to my beloved May.

9. References

H. Kamerlingh Onnes. (1911). Commun. Phys. Lab. Univ. Leiden. Suppl. 29

W. T. Norris. (1969). Calculation of hysteresis losses in hard superconductors carrying ac: isolated conductors and edges of thin sheets, J. Phys. D: Appl. Phys. 1930, Vol. 3, pp. 489-507

W. J. Carr, Jr. (1983). AC loss and macroscopic theory of superconductors, Gordon and Breach, Science Publishers, Inc., ISBN 0-677-05700-8, New York, USA

Li, X., Zhou, Y., Han, L., Zhang, G., et. al. (2010). Design of a High Temperature Superconducting Generator for Wind Power Applications, IEEE Trans. on Appl. Supercond. To be published in ASC 2010 suppl. issue, ISSN: 1051-8223

A. B. Abrahamsen, N. Mijatovic, E. Seiler, T. Zirngibl, C. Træholt, P. B. Nørgard, N. F. Pedersen, N. H. Andersen and J Østergard. (2010). Superconducting wind turbine generators, Supercond. Sci. Technol. Vol. 23, 034019

American Superconductor Corp. Data Sheet and Press Release, Feb. 10th, 2009

Xiaoji Du, Doctoral thesis, 2010

6

Modeling and Designing a Deadbeat Power Control for Doubly-Fed Induction Generator

Alfeu J. Sguarezi Filho and Ernesto Ruppert
School of Electrical and Computer Engineering, University of Campinas
Brazil

1. Introduction

Renewable energy systems, especially wind energy have attracted interest as a result of the increasing concern about CO_2 emissions. Wind energy systems using a doubly fed induction generator (DFIG) have some advantages due to variable speed operation and four quadrants active and reactive power capabilities compared with fixed speed squirrel cage induction generators (Simões & Farret, 2004).
The stator of DFIG is directly connected to the grid and the rotor is connected to the grid by a bi-directional converter as shown in Figure 1. The converter connected to the rotor controls the active and the reactive power between the stator of the DFIG and ac supply or a stand-alone grid (Jain & Ranganathan, 2008).
The control of the wind turbine systems is traditionally based on either stator-flux-oriented (Chowdhury & Chellapilla, 2006) or stator-voltage-oriented (Hopfensperger et al, 2000) vector control. The scheme decouples the rotor current into active and reactive power components. The control of the active and reactive power is achieved with a rotor current controller. Some investigations using PI controllers and stator-flux-oriented have been reported by Peña et al (2008). The problem with the use of a PI controller is the tuning of gains and the cross-coupling on DFIG terms in the whole operating range.
Some investigations using predictive functional controller (Morren et al, 2005) and internal mode controller (Guo et al, 2008) have presented a satisfactory power response when compared with the power response of PI, but it is hard to implement one of them due to the predictive functional controller and internal mode controller formulation. Another way to achieve the DFIG power control is using fuzzy logic (Yao et al, 2007). The controllers calculate at each sample interval the voltage rotor to be supplied to the DFIG to guarantee that the active and the reactive power reach their desired reference values. These strategies have satisfactory power response, although the errors in parameters estimation and the fuzzy rules can degrade the system response.
The aim of this chapter is to provide the designing and the modeling of a deadbeat power control scheme for DFIG in accordance with the present state of the art. In this way, the deadbeat power control aims the stator active and reactive power control using the discretized DFIG equations in synchronous coordinate system and stator flux orientation. The deadbeat controller calculates the rotor voltages required to guarantee that the stator active and reactive power reach their desired references values at each sample period using a rotor current space vector loop. Experimental results using a TMS320F2812 plataform are presented to validate the proposed controller.

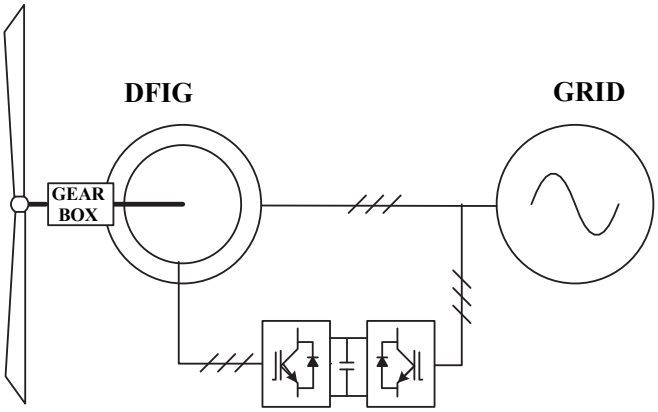

Fig. 1. Configuration of the DFIG directly connected to the grid.

2. Doubly-fed induction machine model

The doubly-fed induction machine model in synchronous reference frame is given by (Leonhard, 1985).

$$\vec{v}_{1dq} = R_1\vec{i}_{1dq} + \frac{d\vec{\lambda}_{1dq}}{dt} + j\omega_1\vec{\lambda}_{1dq} \tag{1}$$

$$\vec{v}_{2dq} = R_2\vec{i}_{2dq} + \frac{d\vec{\lambda}_{2dq}}{dt} + j(\omega_1 - NP\omega_{mec})\vec{\lambda}_{2dq} \tag{2}$$

The relationship between fluxes and currents is done by

$$\vec{\lambda}_{1dq} = L_1\vec{i}_{1dq} + L_m\vec{i}_{2dq} \tag{3}$$

and

$$\vec{\lambda}_{2dq} = L_m\vec{i}_{1dq} + L_2\vec{i}_{2dq} \tag{4}$$

Where $\vec{v}$, $\vec{i}$, $\vec{\lambda}$ are voltage, currents and flux space vectors respectively, R is resistance of the winding, L is inductance of the winding, the subscripts 1, 2, m denotes stator, rotor and mutual, NP is the pole pairs and ω_{mec} is the mechanical rotor speed.
The electromagnetic torque is given by

$$T_e = \frac{3}{2}NP.\,\mathrm{Im}\left\{\vec{i}_1\vec{\lambda}_1^{*}\right\} \tag{5}$$

The superscript $*$ represents the complex conjugate and Im represents the imaginary component of the result.
The mechanical dynamics of the machine is given by:

$$J\frac{d}{dt}\omega_{mec} = T_e - T_L \tag{6}$$

Where J is the load and rotor inertia moment and T_L is the load torque.
The induction machine active power P is

$$P = \left(v_{1d}i_{1d} + v_{1q}i_{1q}\right) \tag{7}$$

and the reactive power Q is

$$Q = \left(v_{1q}i_{1d} - v_{1d}i_{1q}\right) \tag{8}$$

2.1 Power control principles using stator field orientation

The DFIG power control aims independent stator active P and reactive Q power control by means a rotor current regulation. For this propose, the stator field orientation (Novotny & Lipo, 1996) technique is used. Thus, the P and Q are represented as functions of each individual rotor current using the stator flux space vector position. In the synchronous system reference frame dq, the synchronous speed ω_1 is the speed of the stator flux vector and it is given by

$$\frac{d\delta_s}{dt} = \omega_1 \tag{9}$$

The stator flux space vector transformation from stationary reference frame $a\beta$ to the synchronous system reference frame dq is given by:

$$\begin{aligned}&\vec{\lambda}_{1dq} = \lambda_{1d} + j\lambda_{1q} = \\ &= \vec{\lambda}_{1\alpha\beta}e^{-j\delta_s} = \left(\lambda_{1\alpha} + j\lambda_{1\beta}\right)\left[\cos(\delta_s) - j\sin(\delta_s)\right]\end{aligned} \tag{10}$$

Therefore, the components of the direct and quadrature axis become:

$$\lambda_{1d} = \left[\lambda_{1\alpha}\cos(\delta_s) + \lambda_{1\beta}\sin(\delta_s)\right] \tag{11}$$

and

$$\lambda_{1q} = \left[\lambda_{1\beta}\cos(\delta_s) - \lambda_{1\alpha}\sin(\delta_s)\right] \tag{12}$$

Thus, by using the stator flux orientation, the flux space vector components become:

$$\lambda_1 = \lambda_{1d} = \left|\vec{\lambda}_{1dq}\right| = \sqrt{\lambda_{1d}^2 + \lambda_{1q}^2} \tag{13}$$

and

$$\lambda_{1q} = 0 \tag{14}$$

The relationship between the fluxes and currents of Equation (3) becomes, respectively:

$$\lambda_1 = L_1 i_{1d} + L_m i_{2d} \tag{15}$$

and

$$0 = L_1 i_{1q} + L_m i_{2q} \tag{16}$$

In the same way of the stator flux vector components, the stator voltage vector components become:

$$v_{1d} = 0 \tag{17}$$

and

$$v_1 = v_{1q} = \left|\vec{v}_{1dq}\right| = \sqrt{v_{1d}^2 + v_{1q}^2} \tag{18}$$

Now, the active power can be calculated substituting the expression of i_{1q} using Equation (16), the value of v_{1d} of Equation (17) and the value of v_{1q} using Equation (18) in the Equation (7). The new active power expression, using the rotor quadrature axis current i_{2q}, is given by

$$P = -\frac{3L_m}{2L_1} v_1 i_{2q} \tag{19}$$

In the same way of the active power, the reactive power can be calculated by substituting the expression of i_{1d} using Equation (15), the value of v_{1d} of Equation (17) and the value of v_{1q} using Equation (18) in the Equation (8). The new reactive power expression, using the rotor direct axis current i_{2d}, is given by:

$$Q = \frac{3}{2} v_1 \left(\frac{\lambda_1}{L_1} - \frac{L_m}{L_1} i_{2d} \right) \tag{20}$$

From Equations (19) and (20), the stator power can be calculated using the rotor current space vector components. As the stator of the doubly-fed induction generator is directly connected to the grid, the magnitude of the stator flux space vector and the stator voltage space vector is constant. Thus, the independent stator active and reactive power control is achieved through rotor current space vector control.

3. Deadbeat control theory

The deadbeat control is a digital control technique that allows to calculate the required input $\overline{u}(k)$ to guarantee that the output $\overline{x}(k)$ will reach their desired reference values in N samplings intervals using a discrete equation of the continuous linear system (Franklin et al , 1994).

A linear continuous system (Ogata, 2002) can be represented by

$$\begin{aligned} \dot{\overline{x}} &= A\overline{x} + B\overline{u} + G\overline{\omega} \\ \overline{y} &= C\overline{x} \end{aligned} \tag{21}$$

Where ω denotes the perturbation vector and A, C, B and G are nxn matrices. In this paper $C = I$, where I is the identity matrix.

The Equation (21) can be discretized considering T as the sampling period and k as the sampling time. Thus, using zero-order-hold (ZOH) with no delay Equation (21) becomes

$$\bar{x}(k+1) = A_d\bar{x}(k) + B_d\bar{u}(k) + G_d\bar{\omega}_d(k) \tag{22}$$

Where

$$\begin{aligned} A_d &= e^{AT} = I + AT \\ B_d &= \int_0^{\tau} e^{AT} B d\tau = BT \\ G_d &= \int_0^{\tau} e^{AT} G d\tau = GT \end{aligned} \tag{23}$$

The input calculation to guarantee a null steady state error (Franklin et al , 1994) is given by

$$\bar{u}(k) = F(\bar{x}_{ref} - \bar{x}) \tag{24}$$

Where $\bar{x}_{ref} = \bar{x}(k+1)$ and it is the reference vector and *F* is the gain matrix.
Substituting (24) in (22) and making $\bar{x}_{ref} = \bar{x}(k+1)$ the input that guarantees a null steady state error is given by

$$\bar{u}(k) = B_d^{-1}A_d[A_d^{-1}\bar{x}_{ref} - \bar{x}(k)] - A_d^{-1}G_d\bar{\omega}_d \tag{25}$$

The block diagram of the deadbeat control is presented in Figure 2.

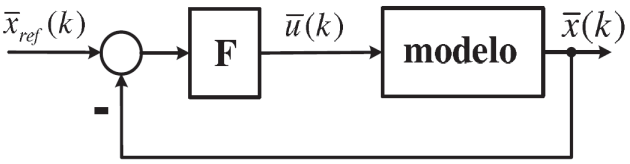

Fig. 2. Deadbeat control block diagram.

4. Deadbeat power control for doubly-fed induction generator

4.1 Rotor side equations

The stator power control of DFIG is made by the rotor current control using the stator field orientation. Thus, the rotor state space equation was necessary in the application of the deadbeat control theory in which the rotor current space vector in synchronous reference frame *dq* is the state variable. In this way, the rotor voltage space vector substituting Equation *(4)* in Equation *(2)* is given by

$$\vec{v}_{2dq} = R_2\vec{i}_{2dq} + \frac{d(L_m\vec{i}_{1dq} + L_2\vec{i}_{2dq})}{dt} + j(\omega_1 - NP\omega_{mec})(L_m\vec{i}_{1dq} + L_2\vec{i}_{2dq}) \tag{26}$$

Which means

$$v_{2d} = R_2 i_{2d} + \frac{d(L_m i_{1d} + L_2 i_{2d})}{dt} - (\omega_1 - NP\omega_{mec})(L_m i_{1q} + L_2 i_{2q}) \tag{27}$$

and

$$v_{2q} = R_2 i_{2q} + \frac{d(L_m i_{1q} + L_2 i_{2q})}{dt} + (\omega_1 - NP\omega_{mec})(L_m i_{1d} + L_2 i_{2d}) \tag{28}$$

Thus, substituting the stator direct axis current i_{1d} of Equation *(*15*)* in the derivative of Equation *(27)* and substituting the stator quadrature axis current i_{1q} of Equation *(*16*)* in the derivative of Equation *(*28*)*, the rotor voltage equations are done by

$$v_{2d} = R_2 i_{2d} + \frac{d}{dt}\left[L_m \left(\frac{\lambda_1}{L_1} - \frac{L_m}{L_1} i_{2d} \right) + L_2 i_{2d} \right] - (\omega_1 - NP\omega_{mec})(L_m i_{1q} + L_2 i_{2q}) \tag{29}$$

and

$$v_{2q} = R_2 i_{2q} + \frac{d}{dt}\left[L_m \left(-\frac{L_m}{L_1} i_{2q} \right) + L_2 i_{2q} \right] + (\omega_1 - NP\omega_{mec})(L_m i_{1d} + L_2 i_{2d}) \tag{30}$$

In this work, the stator of the DFIG is directly connected to the grid and the stator voltage has constant frequency and magnitude. Thus, the magnitude of the stator flux is also constant and in this case $\frac{d\lambda_1}{dt} = 0$. Therefore, the rotor voltage equations become

$$v_{2d} = R_2 i_{2d} - L_2 \omega_{sl} i_{2q} + \left(\frac{L_1 L_2 - L_m^2}{L_1} \right) \frac{di_{2d}}{dt} - L_m \omega_{sl} i_{1q} \tag{31}$$

and

$$v_{2q} = R_2 i_{2q} + L_2 \omega_{sl} i_{2d} + \left(\frac{L_1 L_2 - L_m^2}{L_1} \right) \frac{di_{2q}}{dt} + L_m \omega_{sl} i_{1d} \tag{32}$$

which means

$$\vec{v}_{2dq} = \left(R_2 + jL_2 \omega_{sl} \right) \vec{i}_{2dq} + \left(\frac{L_1 L_2 - L_m^2}{L_1} \right) \frac{d\vec{i}_{2dq}}{dt} + jL_m \omega_{sl} \vec{i}_{1dq} \tag{33}$$

Where $\omega_{sl} = \omega_1 - NP\omega_{mec}$.
In the state-space form, Equation (33) becomes:

$$\dot{\bar{i}}_2 = H\bar{i}_2 + K\bar{v}_2 + L\bar{i}_1 \tag{34}$$

which means

$$\begin{bmatrix} \frac{di_{2d}}{dt} \\ \frac{di_{2q}}{dt} \end{bmatrix} = \begin{bmatrix} \frac{-R_2}{\sigma L_2} & \frac{\omega_{sl}}{\sigma} \\ \frac{-\omega_{sl}}{\sigma} & \frac{-R_2}{\sigma L_2} \end{bmatrix} \begin{bmatrix} i_{2d} \\ i_{2q} \end{bmatrix} + \\ + \begin{bmatrix} \frac{1}{\sigma L_2} & 0 \\ 0 & \frac{1}{\sigma L_2} \end{bmatrix} \begin{bmatrix} v_{2d} \\ v_{2q} \end{bmatrix} + \begin{bmatrix} 0 & \frac{\omega_{sl} L_m}{\sigma L_2} \\ \frac{-\omega_{sl} L_m}{\sigma L_2} & 0 \end{bmatrix} \begin{bmatrix} i_{1d} \\ i_{1q} \end{bmatrix} \tag{35}$$

Where $\sigma = 1 - \frac{L_m^2}{L_1 L_2}$.

From now on, it will be assumed that the mechanical time constant is much greater than the electrical time constants. Thus, ω_{mec} =*constant* is a valid approximation for a sample time. Since the synchronous speed ω_1 is fixed by the grid and $\omega_{sl} = \omega_1 - NP\ \omega_{mec}$, ω_{sl} =*constant* is also a valid approximation for a sample time (Sguarezi Filho et al., 2011).

4.2 Deadbeat power control

The DFIG power control scheme uses a deadbeat controller to obtain rotor voltages which should be applied on induction generator in order to guarantee the active and reactive power reach their desired reference values in a few sample intervals. The sample time *T* interval is the same time of PWM modulator. The power control is made using the rotor current space vector control in the synchronous reference frame *dq*.

Equation (35) can be discretized, since the rotor applied voltage remains constant during a control period of the PWM voltage source inverter. Thus, Equation (35) can be discretized using Equations (22) and *(23)*, considering the mentioned hypothesis above and making:

- $\overline{x} = \overline{i}_2$;
- *A=H;*
- *B=K;*
- $\overline{u} = \overline{v}_2$;
- *G=L;*
- $\overline{\omega} = \overline{i}_1$.

The discrete equation of the rotor voltage is shown in Equation *(36)*.

$$\overline{i}_2(k+1) = A_d \overline{i}_2(k) + B_d \overline{v}_2(k) + G\ \overline{i}_1(k) \tag{36}$$

which means

$$\begin{bmatrix} i_{2d}(k+1) \\ i_{2q}(k+1) \end{bmatrix} = \begin{bmatrix} 1 - \frac{R_2 T}{\sigma L_2} & \frac{\omega_{sl} T}{\sigma} \\ \frac{-\omega_{sl} T}{\sigma} & 1 - \frac{R_2 T}{\sigma L_2} \end{bmatrix} \begin{bmatrix} i_{2d}(k) \\ i_{2q}(k) \end{bmatrix} + \\ + \begin{bmatrix} \frac{T}{\sigma L_2} & 0 \\ 0 & \frac{T}{\sigma L_2} \end{bmatrix} \begin{bmatrix} v_{2d}(k) \\ v_{2q}(k) \end{bmatrix} + \begin{bmatrix} 0 & \frac{\omega_{sl} L_m T}{\sigma L_2} \\ \frac{-\omega_{sl} L_m T}{\sigma L_2} & 0 \end{bmatrix} \begin{bmatrix} i_{1d}(k) \\ i_{1q}(k) \end{bmatrix} \tag{37}$$

Where

$$A_d = e^{AT} = I + AT = \begin{bmatrix} 1 - \frac{R_2 T}{\sigma L_2} & \frac{\omega_{sl} T}{\sigma} \\ \frac{-\omega_{sl} T}{\sigma} & 1 - \frac{R_2 T}{\sigma L_2} \end{bmatrix} \tag{38a}$$

$$B_d = \int_0^\tau e^{AT} B d\tau = BT = \begin{bmatrix} \frac{T}{\sigma L_2} & 0 \\ 0 & \frac{T}{\sigma L_2} \end{bmatrix}$$
$$G_d = \int_0^\tau e^{AT} G d\tau = GT = \begin{bmatrix} 0 & \frac{\omega_{sl} L_m T}{\sigma L_2} \\ \frac{-\omega_{sl} L_m T}{\sigma L_2} & 0 \end{bmatrix} \quad (38b)$$

The rotor voltage which is calculated to guarantee null steady state error using Equations (24) and (37) is given by

$$v_{2d}(k) = \sigma L_2 \frac{i_{2d_{ref}} - i_{2d}(k)}{T} + R_2 i_{2d}(k) - L_2 \omega_{sl} i_{2q}(k) - L_m \omega_{sl} i_{1q}(k) \quad (39)$$

and

$$v_{2q}(k) = \sigma L_2 \frac{i_{2q_{ref}} - i_{2q}(k)}{T} + R_2 i_{2q}(k) + L_2 \omega_{sl} i_{2d}(k) + L_m \omega_{sl} i_{1d}(k) \quad (40)$$

The rotor current space vector references are $i_{2d_{ref}} = i_{2d}(k+1)$ and $i_{2q_{ref}} = i_{2q}(k+1)$.
For the active power control, the rotor current quadrature axis reference using Equation *(19)* is given by

$$i_{2q_{ref}} = -\frac{2 P_{ref} L_1}{3 v_1 L_m} \quad (41)$$

Using Equation *(20)* for the reactive power control, the rotor current direct axis reference is

$$i_{2d_{ref}} = -\frac{2 Q_{ref} L_1}{3 v_1 L_m} + \frac{\lambda_1}{L_m} \quad (42)$$

Thus, if the *d* and *q* axis of the rotor voltage space vector components are calculated according to Equations *(39)-(42)* mentioned above and they are applied to the generator, then the active and reactive power convergence to their respective commanded values will occur in a few sampling intervals. The space vector modulation using the desired rotor voltage in the rotor stationary reference frame *αβr* generates switching signals for the rotor side inverter. The transformation from *dq* reference frame to the *αβr* reference frame is done by:

$$\vec{v}_{2\alpha\beta r}(k) = \vec{v}_{2dq} e^{j(\delta_s - \delta_r)} = \left[v_{2d} \cos(\delta_s - \delta_r) - v_{2q} \sin(\delta_s - \delta_r) \right] + \\ + j \left[v_{2d} \sin(\delta_s - \delta_r) + v_{2q} \cos(\delta_s - \delta_r) \right] \quad (43)$$

In this work the back to back converter is used in the power control strategy. The rotor voltage calculated using the deadbeat control theory will allow to drive the inverter connected to the rotor of DFIG. The converter that is connected to the grid controls the DC-

link voltage and this one can be controlled by a current control presented by Rodríguez et al. (2005). The Deadbeat power control block diagram is shown in Figure 3 and a detailed block diagram of the deadbeat power control implementation is shown in Figure 4.

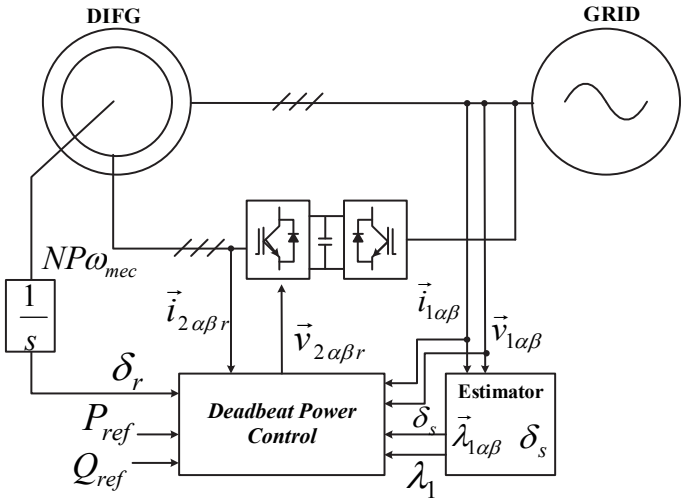

Fig. 3. Deadbeat power control diagram for DFIG.

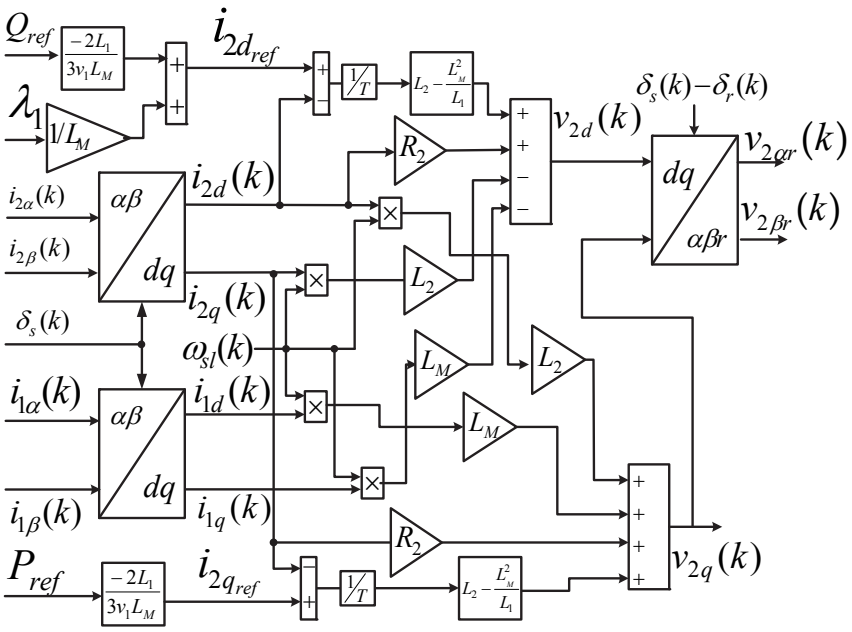

Fig. 4. Detailed deadbeat power control algorithm.

Stator currents and voltages, rotor speed and currents are measured to stator flux position and magnitude, synchronous frequency and slip frequency estimation.

4.3 Estimation

The stator flux estimation in stationary reference frame $a\beta$ is given by

$$\vec{\lambda}_{1\alpha\beta} = \int fem_{1\alpha\beta}\, dt = \int \left(\vec{v}_{1\alpha\beta} - R_1 \vec{i}_{1\alpha\beta}\right) dt \tag{44}$$

The position of stator flux is estimated by using the trigonometric function and it is given by

$$\delta_s = tg^{-1}\left(\frac{\lambda_{1\beta}}{\lambda_{1\alpha}}\right) \tag{45}$$

The synchronous speed ω_1 estimation is given by

$$\omega_1 = \frac{d\delta_s}{dt} = \frac{\left(v_{1\beta} - R_1 i_{1\beta}\right)\lambda_{1\alpha} - \left(v_{1\alpha} - R_1 i_{1\alpha}\right)\lambda_{1\beta}}{\left(\lambda_{1\alpha}\right)^2 + \left(\lambda_{1\beta}\right)^2} \tag{46}$$

and the slip speed estimation using the rotor speed and the synchronous speed is

$$\omega_{sl} = \omega_1 - NP\omega_{mec} \tag{47}$$

The angle in rotor reference frame is

$$\delta_s - \delta_r = \int \omega_{sl} dt \tag{48}$$

5. Experimental results

The deadbeat power control strategy was implemented with a Texas Instruments DSP TMS320F2812 platform which also has a T = 400μs. The system consists of a three-phase voltage source inverter with insulated-gate bipolar transistors (IGBTs) and the three-phase doubly-fed induction generator and its parameters are shown in the appendix. The rotor voltage commands are modulated by using symmetrical space vector PWM, with switching frequency equal to 2.5 kHz. The DC bus voltage of the inverter is 36 V. The stator voltages and currents are sampled in the frequency of 2.5 kHz. The encoder resolution is 3800 pulses per revolution.

The algorithm of the deadbeat control was programmed on the Event Manager 1 of the Texas Instruments DSP TMS320F2812 platform and its flowchart is presented in Figure 5. The schematic of the implementation of the experimental setup is presented in Figure 6 and the experimental setup is shown in Figure 7.

Six tests were made, five in the subsynchronous operation and one in several speed operations from supersynchronous to subsynchronous operation. The first one was the response of i_{2d} step from 0.5A to 5 A which is shown in Figure 8 (a) and the satisfactory performance of the controller can be seen due to the fact that the reference was followed. In this test the i_{2q} is 0.5A.

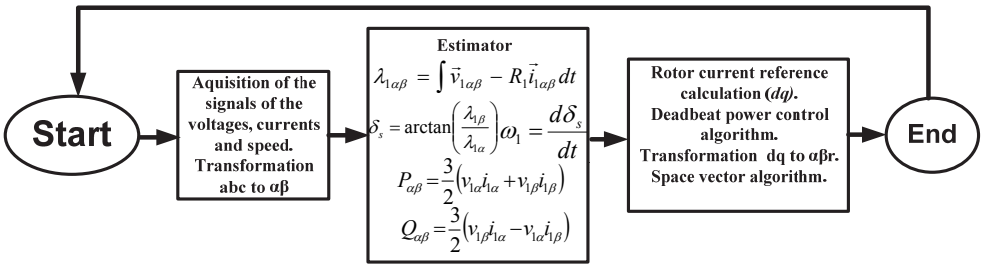

Fig. 5. The flowchart of the DSP program.

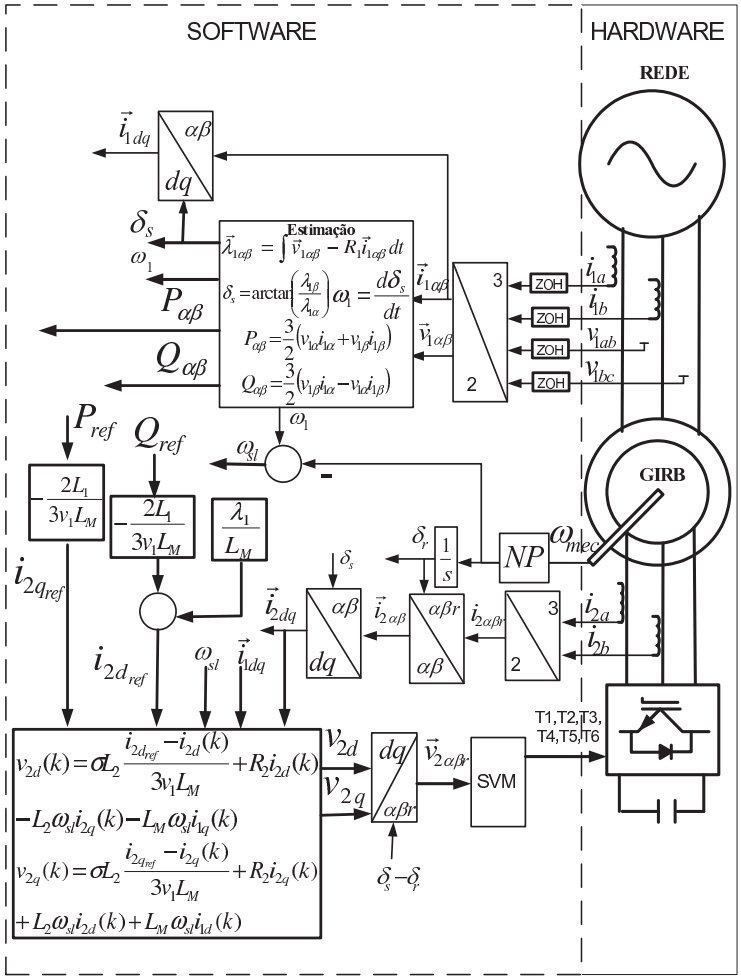

Fig. 6. The schematic of the implementation of the deadbeat power control setup.

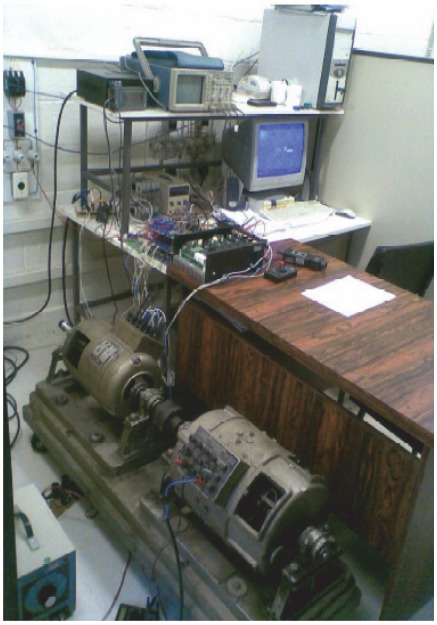

Fig. 7. Experimental Setup.

The second one was the response of i_{2q} step from 0.5A to 5 A. The satisfactory performance of the controller in this test can be seen in Figure 8 (b), due to the fact that the reference was followed. In this test i_{2d} is 4A.

The same test of the i_{2q} step from 0A to 5A, as mentioned above, with rotor currents in rotor reference frame is presented in Figure *9*. In this test the i_{2d} is 5A. The satisfactory response of the controller can be seen due to the fact that the reference was followed and the amplitude of the rotor *ac* currents increased.

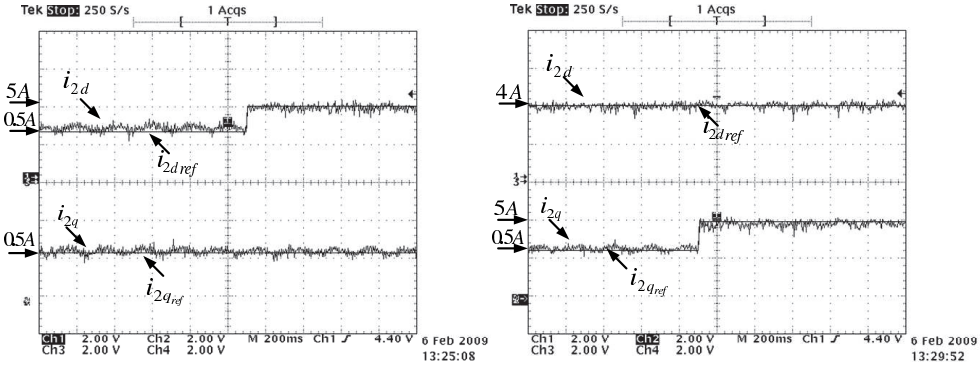

(a) Response of step test of the i_{2d}. (b) Response of step test of the i_{2q}.

Fig. 8. Response of step test of the rotor current (1.33A/div.).

The fourth test was the response of the reactive power Q_{ref} of -300VA, 300VA and 0VA which means leg, lead and unitary power factor. The active power reference is -300W. The rotor current references were calculated using Equations *(41)* and *(42)*. The satisfactory performance of the controller can be seen in Figure 10(a), due to the fact that the reference was followed. The rotor current is shown in Figure 10(b).

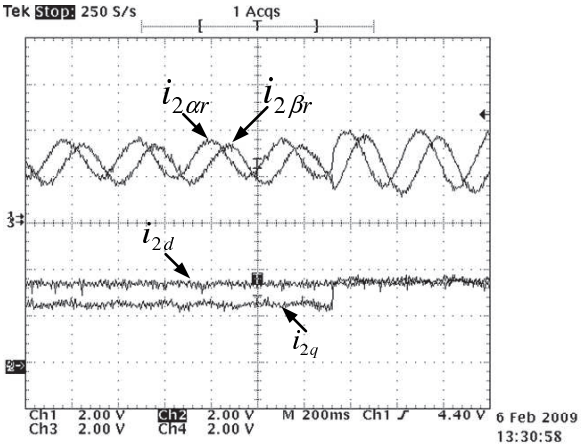

Fig. 9. Response of step test for i_{2q} (1.66 A/div.).

The fifth test was the steady state of unitary power factor and the active power was -300W. Again, the rotor current references were calculated using Equations *(41)* and *(42)*. The response of stator power and rotor current are presented in Figures 11(a) and 11(b), respectively. The stator voltage (127Vrms) and the stator current (0.8Arms) are shown in Figure 12. The satisfactory performance of the controller can be seen because the angle between the stator voltage and the stator current is 180°.

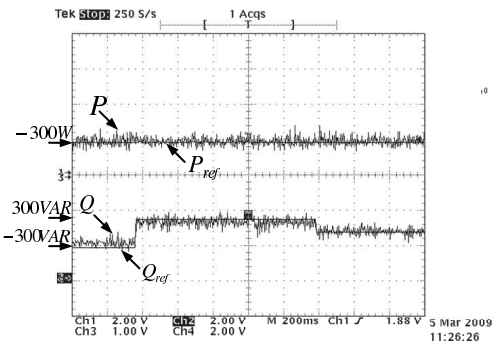

(a) Response of step test of the reactive power (800VA/div.).

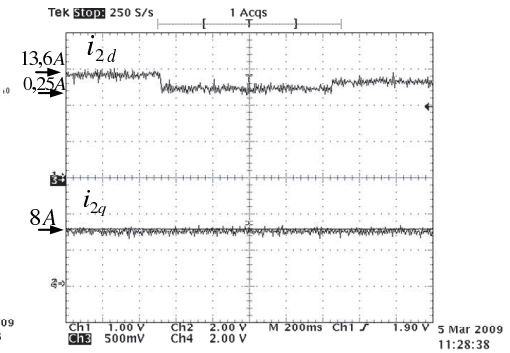

(b) Response of step test of the i_{2d} (28A/div.).

Fig. 10. Response of step of reactive power and rotor direct axis current.

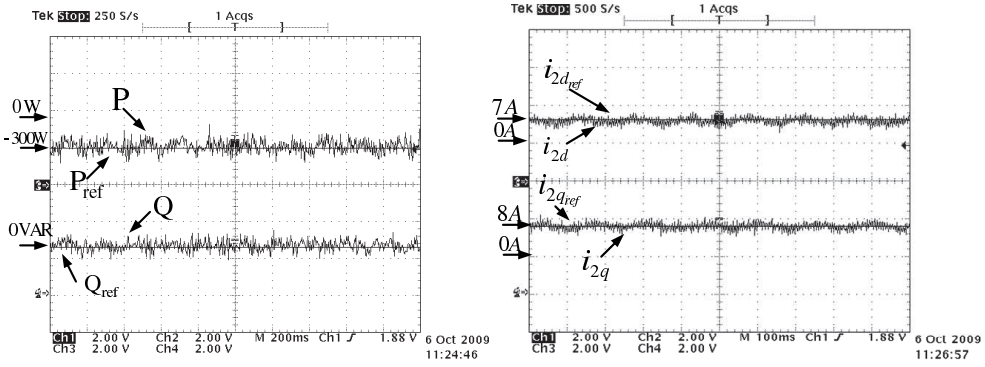

(a) Response of test of the active and the reactive power (300VA/div.).

(b) Response of test of the rotor current (8A/div.).

Fig. 11. Response of steady state test of unitary power factor and the rotor current.

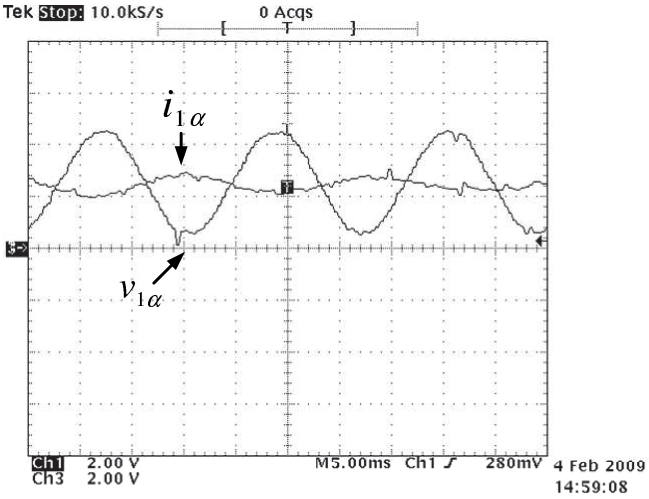

Fig. 12. The stator voltage(18V/div.) and current (0.38A/div.).

In the last test, the generator operates with several speed from 1850 rpm to 1750 rpm and a constant active and reactive power reference of 0W and 0VA, respectively. The rotor current references were also calculated using Equations (41) and (42). So, i_{2dref}= 7A and i_{2qref}= 0A. In this case, this test just maintains the magnetization of the generator. The response of the active and reactive power is shown in Figure 13(a) and the rotor current is presented in Figure 13(b). The rotor speed in several operations and the rotor current of phase α are shown in Figure 14. The satisfactory performance of the controller can be seen during several speed operations, since the reference was followed.

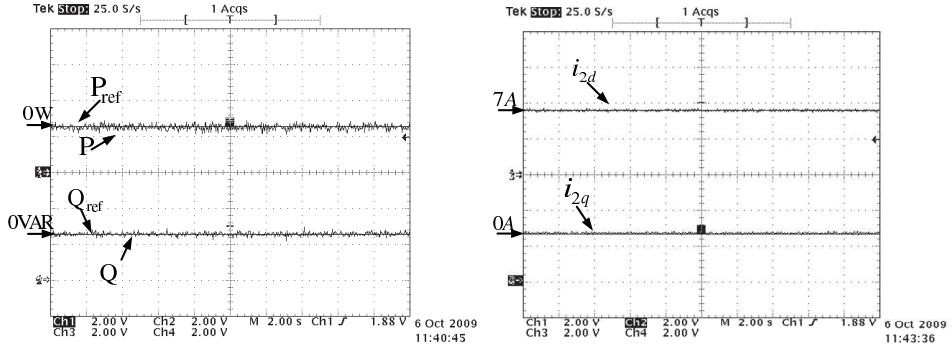

(a) Response of constant active and reactive power.

(b) Response of constant rotor current.

Fig. 13. Response of the active and reactive power and rotor current.

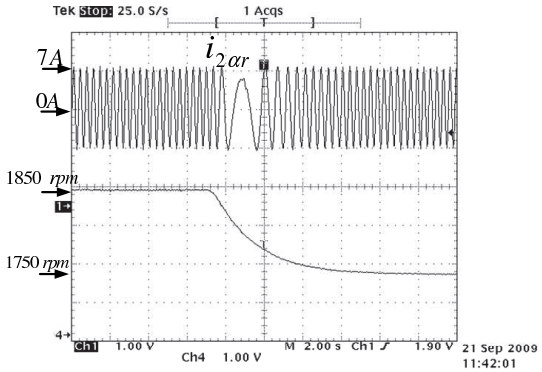

Fig. 14. Rotor speed and current of phase α (7A/div.).

6. Conclusion

This book chapter has presented a model and design of a deadbeat power control scheme for a doubly-fed induction generator using a deadbeat control theory and rotor current space vector loop. The stator field orientation technique allows the independent control of the rotor current components in synchronous reference frame *dq*, in this case, the direct and quadrature axis of the rotor current space vector. Thus, the control of the rotor current components allows controlling the active and reactive power of the generator. The deadbeat controller uses the DFIG discretized equations to calculate at each sample period the required rotor voltages, so that the active and reactive power values reach the desired reference values. Thus, the deadbeat controller does not need to tune gains as the PI controllers. This strategy constant switching frequency overcomes the drawbacks of conventional direct power control (Xu & Cartwright, 2006).

The experimental results confirm the effectiveness of the power controller during several operating conditions of generator speed. Thus, the deadbeat power control strategy is an interesting tool for doubly-fed power control in wind turbines.

7. Acknowledgment

The authors would like to thank FAPESP (Fundação de Amparo à Pesquisa do Estado de São Paulo) for the financial support.

8. Appendix

Doubly-fed induction generator parameters:
R_1 = 2.2 Ω; R_2 = 1.764 Ω; L_m = 0.0829 H; L_{l1} = 0.0074 H; L_{l2} =0.0074H ; J = 0.05 Kg.m^2; NP = 2; PN = 2.25 kW; VN = 220 V.

9. References

Simões, M. G & Farret, F. (2004). *Renewable Energy Systems with Induction Generators*. CRC PRESS.

Jain, A. K. & Ranganathan, R. T. (2008). Wound Rotor Induction Generator With Sensorless Control and Integrated Active Filter for Feeding Nonlinear Loads in a Stand-Alone Grid. *IEEE Transactions on Industrial Electronics*, 55 (1), pp. 218-228.

Chowdhury, B. H. & Chellapilla, S. (2006). Double-fed induction generation control for variable speed wind power generation. *Electric Power System. Research*, no. 76, pp. 786–800.

Hopfensperger, B.; Atkinson, D. J.; & Lakin, R. (2000). Stator-flux-oriented control of a doubly-fed induction machine with and without position encode. *Proc. Inst. Elect. Eng., Electr. Power Applications*, vol. 147, no. 4, pp. 241 – 250, April.

Peña, R.; Cárdenas, R.; Proboste, J.; Asher, G.; & Clare, J. (2008). Sensorless control of doubly-fed induction generators using a rotor-current based MRAS observer. *IEEE Trans. Ind. Electron.*, vol. 55, no. 1, pp.330 – 339, January.

Morren, J.; Sjoerd, M. & de Haan, W. H. (2005). Ridethrough of wind turbines with doubly-fed induction generator during a voltage dip. *IEEE Transactions on Energy Conversion*, vol. 20, no. 2, pp. 435–441, June.

Guo, J.; Cai, X. & Gong, Y. (2008). Decoupled control of active and reactive power for a grid-connected doubly-fed induction generator. *Third International Conference on Electric Utility Deregulation and Restructuring and Power Technologies. DRPT 2008*, pp. 2620 – 2625, China, April.

Yao, X.; Jing, Y. & Xing, Z. (2007). Direct torque control of a doubly-fed wind generator based on grey-fuzzy logic. *International Conference on Mechatronics and Automation. ICMA 2007*, pp. 3587 – 3592, China, August 2007.

Leonhard, W. (1985). *Control of Electrical Drives*. Berlin, Germany: Springer-Verlag.

Novotny, D. W. & Lipo, T. A. (1996). *Vector Control and Dynamics of AC Drives*, Clarendon Press OXFORD.

Franklin, G. F.; Powel, J. D. & Workman, M. L. (1994). *Digital Control of Dynamic Systems*. Addison-Wesley Publishing Company.

Ogata, K. (2002). *Modern Control Engineering*. Prentice Hall

Sguarezi Filho, A. J.; de Oliveira Filho, M. E. & Ruppert Filho, E. (2011). A Predictive Power Control for Wind Energy. *IEEE Transactions on Sustainable Energy*, vol. 2, no. 1, pages: 97-105.

Rodríguez, J. R. & Dixon, J. W.; Espinoza, J. R; Pontt, J.; & Lezana, P. (2005). Pwm regenerative rectifiers: State of the art. *IEEE Transactions Industrial Electronics*, vol. 52, no. 1, February.

Xu, L. & Cartwright, P. (2006). Direct active and reactive power control of DFIG for wind energy generation. *IEEE Trans. Energy Convers.*, vol. 21, no. 3, pp. 750 – 758, September.